Synthesis of Nano Hydroxyapatite/Stilbite Composite for Defluoridation of Drinking Water

Taju Sani

A Thesis Submitted to

The Department of Chemistry

Presented in Partial Fulfilment of the Requirements for the Degree of

Doctor of Philosophy (Inorganic Chemistry)

Addis Ababa University

Addis Ababa, Ethiopia

April 2016

Addis Ababa University

School of Graduate Studies

This is to certify that the thesis prepared by Taju Sani Ahmed entitled: ***Synthesis of Nano Hydroxyapatite/Stilbite Composite for Defluoridation of Drinking Water*** and submitted in partial fulfillment of the requirements for the Degree of Doctor of Philosophy (Inorganic Chemistry) complies with the regulations of the university and meets the accepted standards with respect to originality and quality.

Signed by the Examining Committee:

Name	Signature	Date
________________________	____________________	April 20, 2016
External Examiner		
______________________	____________________	April 20, 2016
Internal Examiner		
______________________	____________________	April 20, 2016
Internal Examiner		
______________________	____________________	April 20, 2016
Advisor		
______________________	____________________	April 20, 2016
Advisor		

____

Chair of Department or Graduate Program Coordinator

Synthesis of Nano Hydroxyapatite/Stilbite Composite for Defluoridation of Drinking Water

Abstract

Taju Sani

Addis Ababa University, 2016

The presence of high fluoride in groundwater used for drinking has become a matter of great concern in the Rift Valley of Ethiopia due to its serious health hazard, flourosis. Hence, developing easily accessible and socially acceptable low cost removal methods capable of reducing the fluoride concentration below the limit established by WHO (1.5 mg/L) is nowadays a crucial target. In this study, the defluoridation capacity of locally available cheap natural stilbite zeolite and its modified version of high-performing and low energy demanding nanohydroxyapatite/stilbite, nHAST composite adsorbent for fluoride removal have been investigated. While modifying, stilbite zeolite plays a dual role: as a support material and a reagent for calcium source, because this particular stilbite from Ethiopia is rich in calcium. Based on this fact, the modification procedure was carried out simply by the addition of phosphate source, in this case $(NH_4)_2HPO_4$ to stilbite. In the reaction, Ca^{2+} from STI are first ion-exchanged by NH_4^+ ions, thus released to the solution. At a favourable pH, the Ca^{2+}ions react with PO_4^{3-} forming hydroxyapatite that precipitates on the zeolite surface in the form of nanocrystals, nHAST composite (**n**ano**H**ydroxy**A**patite**ST**ilbite).

In order to manage the growth of significantly smaller crystals of hydroxyapatite with higher fluoride removal capacities, the effect of synthesis time, crystallization pH and crystallization time are carefully optimized based on powder XRD, ICP-OES, TGA, IR-ATR, ^{31}P MAS-NMR, TEM (C_s-STEM/EELS) and defluoridation capacity. The nHAST composite, which is found to have highest efficiency and capacity was successfully synthesized using crystallization time of 144 hours at autogenous crystallization pH of 8, and 2 hours synthesis time at room temperature conditions.

Batch adsorption studies were performed as a function of solution pH effect, co-ion effect, contact time, adsorbent dose and initial fluoride concentration. Interestingly, unlike most adsorbents, nHAST composite shows high defluoridation capacity in a wider pH range with maximum of 86 % and minimum of 79 % fluoride removal at pH 3 and 10, respectively. Similarly, nHAST composite shows no effect due to chloride and sulfate concentrations ranging from 0 to 500 mg/L. In real situation as well, nHAST was found to be efficient. From real water with fluoride concentration of 8.2 mg/L, at a dose of 10 g/L nHAST resulted in a final fluoride concentration of 1.40 mg/L, below the limit established by WHO.

Finally, the fluoride removal performance of nHAST composite was compared with that of Bone Char, an applied technology as adsorbent in the field in Ethiopia. It is worth noting that preparation of bone char involves prolonged high-temperature charring treatments, which should be performed under carefully controlled conditions, and of course involves consumption of energy. On the other hand the synthesis of nHAST composite is very easily performed, and does not require energy or skilled manpower. The reaction mechanism involving the fluoride adsorption is analyzed based on kinetics and isotherm studies. In both nHAST and BC, the kinetic data fitted well to a pseudo-second order kinetic model of similar characteristics. In contrast, the adsorption isotherm on the nHAST composite fitted best with the Freundlich model, whereas on BC, it correlated well with the Langmuir model, suggesting a different mechanism: adsorption of fluoride on BC was homogeneous, whereas on composite, it was heterogeneous, possibly related to the higher load of fluoride on the nHAp component in the composite. At low concentrations, both adsorbents behave similarly, the maximum adsorption capacity, measured at high concentrations, is higher in the nHAST composite than in BC. The intrinsic HAp capacity of nHAST, normalized to the amount of HAp on the adsorbent, is significantly higher (9.15 mg F^-/g HAp) than that of BC (1.08 mg F^-/g HAp) (measured at low F^- initial concentrations where the OH^-/F^-–exchange mechanism predominates), showing a much higher fluoride removal efficiency of nHAp on the composite. These results foresee a high potential of nHAST composite towards its application for defluoridation of potable water.

Acknowledgments

First of all, I would like to express my sincere gratitude and respect to my supervisors Prof. Isabel Diaz and Dr. Yonas Chebude for their thoughtful guidance, continuous supervision, and encouragement through all the stages of this thesis. Really, I remain thankful for their utmost dedication in providing all research facilities necessary for my research work including the provision of financial support during my five months stay in Madrid to do part of my research work in her well equipped laboratory at Instituto de Catálisis y Petroleoquímica, CSIC, Madrid, Spain.

My heartfelt gratitude is extended to Prof. Joaquín Pérez-Pariente and Dr. Luis Gómez-Hortigüela for their valuable cooperation, invaluable discussion, and continuous support during my stay in Madrid, and enormous contributions in my research work.

My sincere thanks go to Dr. Carlos Marquez, Javier Agundez, Isabel Pacheco, Conchi, Dr. Manuel Sanchez Sanchez and Dr. Alvaro Mayoral for their genuine assistance during characterization of my samples. I would also like to acknowledge Prof. Pedro Bosch, Dr. Eduardo Pérez and Dr. Pilar Gálvez are for helpful discussions. I also acknowledge Prof Vicente Cortes and his family, Dr. Enrique Sastre, Dr. Victoria Gascon, Cecilia Manrique, and all PhD students in the Molecular Sieves Group of the ICP-CSIC for their valuable support and cooperation.

I am also thankful to my friends, Tefera Haile, Minale Demelash, Belayhun Mandefro, and all my group members, Dr. Wondimagegne Mamo, Guta Gonfa, Kiros Guesh, Lijalem Ayele, Solomon Legesse, Meseret Desalegne, Masresha Amare and

Tesfaye Haile for their encouragement, support and constructive suggestions throughout my research work. I thank Mohammedali Adem, a Masters student at AAU for his contribution.

I would also like to express my utmost gratitude to Addis Ababa University, Department of Chemistry and its staff members for their unreserved cooperation. I also want to thank Dilla University for giving me the study leave to pursue my PhD at AAU and financial support. I would like to thank the Spanish Research Council for supporting this thesis through scientific research project and Oromo Self Help Organization (OSHO) for the kind donation of Bone Char and synthetic HAp raw samples. My sincere thanks would go to Dr. Asfawossen Asrat and Prof. Solomon Tadesse, Earth Science Department, AAU for their kind donation of natural Ethiopian Zeolite samples.

I would like to express my indebtedness and offer my special thanks to my father Sani Ahmed, my mother Radiya Osmail, my brothers Salhadin Sani and his family, Jemal Sani and Duru Kadi and his family, my sister Jelila Sani. Their support and encouragement were unique in all my life. Most importantly, special thanks to my family, my wife Halimet Endris and my sons Sora Taju and Amir Taju, and my daughter Tasnim Taju for their love, understanding and endless patience.

Table of Contents

Abstract iii

Acknowledgments vi

List of Figures xiii

List of Schemes xvii

List of Tables xviii

List of Abbreviations xx

Chapter One 1

1. Introduction 1

  1.1. Fluoride occurrence 1

  1.2. Fluoride adsorption mechanisms 3

  1.3. Health effects of fluoride: World and the Ethiopian scenario 4

  1.4. Guidelines of drinking water 7

  1.5. Overview of defluoridation techniques 8

    1.5.1. Adsorbent materials for defluoridation 11

  1.6. Rationale of the study 23

  1.7. Objectives 27

    1.7.1. General objectives 27

    1.7.2. Specific objectives 27

Chapter Two 28

2. Experimental 28

  2.1. Materials and Methods 28

2.1.2. Adsorbent preparation: Synthesis of nHAST composite 28

2.1.3. Synthesis procedure optimization for nHAST composite 30

2.1.4. Synthesis procedure and reproducibility test 31

2.2. Characterization Methods 31

2.2.1. Powder X-ray diffraction 32

2.2.2. Inductively Coupled Plasma, ICP analysis 32

2.2.3. Thermogravimetric analysis... 32

2.2.4. Infrared Spectroscopy 33

2.2.5. Electron Microscopy 33

2.2.6. Nuclear Magnetic Resonance Measurements 34

2.2.7. Point of zero charge determination 34

2.3. Defluoridation studies 35

2.3.1. Adsorption kinetics and isotherms 37

2.3.2. Effect of process parameters on fluoride adsorption by nHAST 39

2.3.3. Regeneration experiments 41

2.3.4. Scaling-up nHAST synthesis and using recovered filtrate solutions 41

Chapter Three 43

3. Results and Discussion on Natural Zeolites 43

3.1. Characterization and Defluoridation test 43

3.1.1. Powder X-ray diffraction analysis 43

3.1.2. Thermogravimetric analysis 44

3.1.3. ICP elemental composition studies....................44

3.2. Defluoridation test....................46

3.3. Comparison of Defluoridation capacity of zeolites from Ethiopia and Mexico....................48

3.3.1. Characterization of zeolites....................48

3.3.2. Defluoridation test results....................51

Chapter Four....................57

4. Results and Discussion on nHAST composite....................57

4.1. X-ray diffraction analysis results....................57

4.2. IR-ATR analysis result....................58

4.3. ICP elemental analysis results....................59

4.4. Defluoridation test results....................60

4.5. Optimization of synthesis procedure for nHAST composite....................61

4.5.1. Synthesis time optimization....................61

4.5.2. Crystallization pH optimization....................67

4.5.3. Crystallisation time optimization....................79

4.6. Factors affecting fluoride adsorption onto nHAST....................96

4.6.1. Effect of adsorbent dose....................96

4.6.2. Effect of contact time....................97

4.6.3. Effect of initial fluoride concentration....................99

4.6.4. Effect of solution pH....................100

4.6.5. Effect of co-existing anions....................102

4.6.6. Regeneration of nHAST composite 103

4.6.6. Fluoride removal on real groundwater from Ethiopian Rift Valley 107

4.6.7. Optimized synthesis procedure and reproducibility test 108

4.7. Scale-up of nHAST composite synthesis 114

4.7.1. ICP elemental analysis result 116

4.7.2. Thermogravimetric analysis 117

4.7.3. Point of zero charge determination 119

4.7.4. Defluoridation test results 121

4.8. Comparison of nHAST composite with Bone Char 123

4.8.1. X-ray diffraction analysis result 123

4.8.2. Thermogravimetric analysis result 125

4.8.3. IR-ATR analysis results 127

4.8.4. ^{31}P MAS-NMR analysis result 128

4.8.5. Fluoride removal results and adsorption mechanisms 131

4.8.6. Experimental results on kinetic studies 132

4.8.7. Experimental result on adsorption isotherm 137

4.9. Comparison of nHAST composite with synthetic HAp 142

Chapter Five 146

5. Conclusions 146

List of Publications 148

References 149

Appendices......166

Appendix 1: Experimental curves corresponding to the potentiometric mass titrations technique for the determination of the PZC of a) nHAST-1, b) nHAST-2, c) nHAST-3......166

Appendix 2: T. Sani, M. Adem, P. Bosch, I. Diaz, Defluoridation Performance Comparison of Nanohydrotalcite/Hydroxyapatite Composite with Calcined Hydrotalcite and Hydroxyapatite, Water Air Soil Pollution, 90 (2016) 227-233, DOI 10.1007/s11270-016-2786-2......167

List of Figures

Figure 1: Geographical area of the world with high risk of fluorosis. Countries in blue have high fluoride concentration >1.5 mg/L in drinking water 5

Figure 2: Fluoride concentration profile in drinking water sources of Ethiopia............6

Figure 3: Representations of basic building tetrahedra TO_4 (T, Si/Al) and an open structure cages built from tetrahedra units, and channels of zeolites 13

Figure 4: The framework of stilbite zeolite 15

Figure 5: Crystal structure of hydroxyapatite 18

Figure 6: Structural representation of hydrotalcites..22

Figure 7: Picture of natural stilbite rock sample from Ethiopian.................................24

Figure 8: XRD pattern of STI zeolite 43

Figure 9: TGA (solid line) and DTG (dotted line) of the STI sample 44

Figure 10: SEM-EDX mapping of STI sample...46

Figure 11: F^- removal performance of the STI from Ethiopia from a) 20 and b) 5 mg/L initial fluoride concentrations as a function of dose 48

Figure 12: Thermogravimetric analyses of Mexican natural zeolites..........................51

Figure 13: Suggested mechanisms for fluoride retention in natural zeolites...............55

Figure 14: XRD profiles of the support STI and nHAST composite samples.............57

Figure 15: IR-ATR spectra of a) nHAST composite and b) STI zeolite 59

Figure 16: XRD profiles of the support STI zeolite and the nHAST composites synthesized as a function of synthesis time 62

Figure 17: IR-ATR spectrum of the support STI zeolite and nHAST composites at various synthesis times 64

Figure 18: F^- removal capacity (dashed lines) and removal efficiency (solid lines) of nHAST composite samples as a function of synthesis time 66

Figure 19: XRD profiles of the support STI zeolite and nHAST composite samples as a function of crystallization pH.......68

Figure 20: IR-ATR spectra of a support raw precursor, STI and nHAST composite samples as a function of crystallization pH.......69

Figure 21: TGA (solid lines) and DTG (dotted lines) of the nHAST composites synthesized at various crystallization pH, and the support STI zeolite.......71

Figure 22: SEM micrographs of nHAST composite samples synthesized at various pH of crystallization.......75

Figure 23: F^- removal performance of the nHAST composites synthesized at different crystallization pH at a) 5 mg/L and b) 10 mg/L initial fluoride concentrations.......77

Figure 24: XRD profiles of the support STI zeolite and nHAST composite samples as a function of crystallization time.......80

Figure 25: IR-ATR spectra of a support STI zeolite and nHAST composite samples as a function of crystallization time.......81

Figure 26: TGA (doted lines) and DTG (solid lines) of STI and nHAST composite samples.......83

Figure 27: F^- equilibrium concentration (solid lines) and removal efficiency (dotted lines) as a function of crystallization time of nHAST composite samples.......86

Figure 28: Percent HAp crystallized in nHAST composites and the corresponding defluoridation capacity as a function of crystallization time at 10 g/L dose.......88

Figure 29: ^{31}P MAS-NMR spectra of nHAST 144h at pH 8 and nHAST 19h at pH 8 (solid lines), and nHAST 19h at pH 9 (dashed line), and HAp (dotted line).......90

Figure 30: STEM/HAADF/EELS results on nHAST 19h and nHAST 144h.......92

Figure 31: Comparison of STEM images at different magnification for HAp grown on stilbite surface for nHAST 19h and nHAST 144h samples.......93

Figure 32: Experimental curves corresponding to the potentiometric mass titration technique for the determination of the PZC of natural STI zeolite............................94

Figure 33: Experimental curves corresponding to the potentiometric mass titration technique for the determination of the PZC of nHAST 144h....................................95

Figure 34: The effect of adsorbent dose on fluoride removal efficiency (dotted lines) and fluoride equilibrium concentrations (solid lines) by nHAST composite 97

Figure 35: Fluoride removal efficiency as a function of contact time at 10 g/L dose of nHAST composite (C_o = 10 mg/L) 98

Figure 36: Effect of initial fluoride concentration onto nHAST composite fluoride removal capacity, studied at 10 g/L dose...99

Figure 37: SEM micrograph of nHAST composite 100

Figure 38: Effect of solution pH on fluoride removal of nHAST composite 101

Figure 39: Effect of coexisting ions on fluoride removal of nHAST composite, studied at 10 g/L dose...103

Figure 40: Defluoridation capacity of nHAST composite in consecutive cycles before regeneration...104

Figure 41: XRD patterns of the regenerated nHAST adsorbent samples 105

Figure 42: Effect of regeneration on defluoridation capacity of nHAST 106

Figure 43: Fluoride desorption test of regenerated adsorbent samples.....................107

Figure 44: XRD patterns of zeolite samples 109

Figure 45: XRD patterns of nHA/zeolite composite samples synthesized at best optimized synthesis procedure for nHAST composite 111

Figure 46: Fluoride removal efficiency of natural zeolites (Z4-Z9, STI) (black bar) and the corresponding nHA/Zeolite composites (white bar) 113

Figure 47: TGA and DTG curves of STI and nHAST composite samples 118

Figure 48: Experimental curves corresponding to the potentiometric mass titrations technique for the determination of the PZC of nHAST-0..120

Figure 49: Experimental curves corresponding to the potentiometric mass titrations technique for the determination of the PZC of nHAST-Mix composite 121

Figure 50: Fluoride removal efficiency (%) of nHAST composite samples (dose = 10 g/L)..122

Figure 51: XRD profiles of the support STI, nHAST composite and BC samples...124

Figure 52: TGA (solid lines) and DTG (dashed lines) of the STI, nHAST and BC samples..126

Figure 53: IR-ATR spectra of a) nHAST composite b) STI zeolite, and c) BC........127

Figure 54: ^{31}P MAS NMR spectra of the nHAST composite and BC samples.........129

Figure 55: SEM micrographs of a) STI, b) nHAST composite, and c) BC..............130

Figure 56: Fluoride equilibrium concentration (dashed lines) and removal efficiency (solid lines) of nHAST composite and BC as a function of dose.............................131

Figure 57: Fluoride adsorption kinetics on nHAST and BC composite samples at initial fluoride concentration of 10 mg/L and dose of 10 g/L..................................133

Figure 58: a) Pseudo-first order and b) Pseudo-second order plot of fluoride adsorption kinetics at a dose of 10 g/L and 10 mg/L initial fluoride concentration..136

Figure 59: nHAST and BC fluoride adsorption isotherms performed at a dose of 10 g/L, with varying initial concentrations...138

Figure 60: Linearized Langmuir adsorption isotherm for fluoride adsorption..........140

Figure 61: Linearized Freundlich adsorption isotherm for fluoride adsorption 141

Figure 62: Fluoride removal efficiency (%) of BC, synthetic HAp, and nHAST composite samples at 10 g/Ldose 143

List of Schemes

Scheme 1: A simple illustration for the preparation of nHAST composite----------- 29

Scheme 2: Scaling up synthesis process illustration of nHAST-0, nHAST-1, nHAST-2 and nHAST-3 composites using the recovered filtrates (APs) ------------------------ 115

List of Tables

Table 1: ICP chemical composition analysis of STI sample 45

Table 2: Structural identification by XRD analysis of the natural zeolite from Ethiopia and Mexico..49

Table 3: Categorization and structural properties of clinoptilolite, heulandite, stilbite, and analcime taken from the Atlas of natural zeolite framework 50

Table 4: Fluoride removal efficiency as a function of adsorbent dose from initial fluoride concentrations of a) 20 mg/L and b) 5 mg/L, respectively 52

Table 5: ICP elemental analysis of STI and nHAST composite samples....................60

Table 6: Fluoride removal efficiency of the support STI and nHAST composite.......61

Table 7: ICP elemental analysis results on STI zeolite and nHAST composites 65

Table 8: ICP elemental analysis result of the support STI and nHAST composites synthesized as a function of crystallization pH...72

Table 9: ICP elemental analysis result of the support STI and nHAST composites synthesized at different crystallization time 85

Table 10: Physicochemical parameters of groundwater samples, before and after treated with nHAST adsorbent...108

Table 11: ICP elemental analysis of Zeolite samples 110

Table 12: ICP elemental analysis of nHAZ4-nHAZ9 composite samples synthesized at the optimized synthesis procedure 112

Table 13: ICP elemental analysis of nHAST-0, nHAST-1, nHAST-2, and nHAST-3samples synthesized in scale-up at slightly different crystallization pH 116

Table 14: ICP elemental analysis of a support STI, nHAST composite and BC.......125

Table 15: Data for fluoride adsorption kinetics of nHAST and BC, at 10g/L dose and 10 mg/L initial fluoride concentration 134

Table 16: Summary of the Pseudo-first order and Pseudo-second order rate constants and correlation coefficients of nHAST and BC adsorbents......................................135

Table 17: Langmuir and Freundlich isotherm model parameters describing the nHAST and BC fluoride adsorption 139

Table 18: Maximum (monolayer) defluoridation capacities of some adsorbents reportedin literature...145

List of Abbreviations

AP	Ammonium Phosphate
ATR-IR	Attenuated Total Reflectance infrared
BC	Bone Char
a.u	arbitrary unit
EDX	Energy Dispersive X-ray
EELS	Electron Energy Loss Spectroscopy
HAADF	High Angular Annular Dark Field
HAp	Hydroxyapatite
ICP–OES	Inductively Coupled Plasma Optical Emission Spectrometry
IZA	International Zeolite Association
nHAST	Nano Hydroxyapatite/Stilbite
OSHO	Oromo Self Help Organization
PZC	Point of Zero Charge
^{31}P MAS NMR	^{31}P Magic Angle Spinning Nuclear Magnetic Resonance
SEM	Scanning Electron Microscope
Si/Al	Silicon to Aluminum ratio
STEM	Scanning Transmission Electron Microscope
STI	Stilbite
TDS	Total Dissolved Solids
TGA	Thermogravimetric Analysis
TISAB	Total Ionic Strength Adjusting Buffer
UNICEF	United Nations International Children’s Emergency Fund
WHO	World Health Organization
XRD	Powder X-Ray Diffraction

Chapter One

1. Introduction

1.1. Fluoride occurrence

Fluorineis the 13th most abundant naturally occurring element in the Earth's crust [1-4]. Due to its very high reactivity, it is found chemically as fluoride (F^-) in various rocks, commonly in Fluorite (CaF_2), Cryolite (Na_3AlF_6) and Fluorapatite ($Ca_5(PO4)_3F$) [4-7]. Although these fluoride bearing minerals are hardly soluble in water, when conditions favor they do dissolve in polluted water, or are found through human activities such as discharge by agricultural and industrial activities including fertilizer, steel, aluminum and glass manufacturing, and electroplating [8-13].

Generally, most groundwater sources have higher fluoride concentrations than surface water. As groundwater percolates through the weathered rock in the aquifers, it dissolves fluoride bearing minerals, hence releasing fluoride into solution [4]. Due to the large number of variables that include the geological, chemical and physical characteristics of the aquifer, the porosity and acidity of the soil and rocks, the temperature, the depth of the aquifer and the action of other chemical elements [14, 15], the fluoride concentrations in groundwater can range from well under 1 mg/L to more than 35 mg/L [16]. High fluoride levels are often seen in regions where there is geothermal or volcanic activity. The floor of the East African Rift Valley is characterized by high hydrothermal activity, which accelerates the solubility of fluoride bearing minerals such as fluorite and fluorapatite with high concentrations of fluoride in the groundwater [17]. In another similar study by T. Rango et al., the presence of high fluoride levels was demonstrated in alkaline (pH of 7 to 8.9) groundwater containing high concentrations of sodium (Na^+), and bicarbonate (HCO_3^-), and low concentrations of calcium (Ca^{2+}) [18]. When fluoride rich minerals come in contact with water of high alkalinity, they release fluoride into groundwater through hydrolysis replacing hydroxyl (OH^-) ion. The degree of weathering and leachable fluoride in a terrain is more important in deciding the fluoride bearing minerals in the bulk rocks or soil. Due to weathering of rocks, the Ca-Mg carbonate concentration in arid and semi-arid areas appears to be a good sink for the fluoride ion [4]. Thus, a low level of Ca in water supplies means higher levels of fluoride solubility [19, 20].

Human exposure to fluoride may occur through food chain, drinking water and even inhalation. However, drinking water is a major source [21-23] and is responsible for 75 to 90 % of daily fluoride intake [24, 25]. The level of fluoride in drinking water is a very important physicochemical factor, which must be considered when assessing water quality for human consumption. Based on current literature, fluoride has both beneficial and detrimental health effects depending on its concentration in drinking water [26]. As a trace element, fluoride is essential to the growth as well as strengthening of teeth and bones [18, 27, 28], and in that it is especially beneficial to young children below eight years of age. Low intake of fluoride could reduce the incidence of dental caries [13, 27, 28]. Though dental caries is not life threatening, it might decrease one’s quality of life through inflicting pain, impeding nutrition, and incurring treatment costs.

In contrast, excess ingestion of fluoride can cause dental/skeleton fluorosis and increased blood pressure [29-33]. It has been reported that chronic ingestion of fluoride and its accumulation over a long period of time can bring about further complications (cancer, osteosclerosis and neurological impairment) [34]. In recognition of high levels of fluoride in drinking water to be a risk factor for fluorosis, the World Health Organization (WHO) has set the maximum permissible limit of fluoride in drinking water at 1.5 mg/L [6, 35]. However, the recommended level to achieve maximum protection against dental caries and risk of fluorosis is in the range between 0.5 and 1 mg/L [13, 18].

1.2. Fluoride adsorption mechanisms

Consumption of high amount of fluoride exposes to fluorosis, most probably due to its reaction with HAp, $Ca_{10}(PO_4)_6(OH)_2$, the main inorganic constituent of bones and teeth. Several studies were conducted on the mechanism of fluoride adsorption onto HAp particles [14, 36-42]. In general, both physical adsorption originating from electrostatic interaction (eq. 1) and chemical adsorption from ion exchange (eq. 2 and 3) were proposed as the main driving force for fluoride uptake onto HAp surfaces [37-39, 41, 42].

$$Ca_{10}(PO_4)_6(OH)_2 + n\,F^- \longrightarrow Ca_{10}(PO_4)_6(OH)_2 \ldots F_n^- \qquad [1]$$

$$Ca_{10}(PO_4)6(OH)_2 + F^- \longrightarrow Ca_{10}(PO_4)_6(F,OH) + OH^- \qquad [2]$$

$$Ca_{10}(PO_4)_6(OH)_2 + 2F^- \longrightarrow Ca_{10}(PO_4)_6F_2 + 2OH^- \qquad [3]$$

Furthermore, it has been reported that the fluoridation at significantly high fluoride concentration could also take place on HAp dissolved surface phase to form calcium fluoride (CaF_2) [40, 43, 44] as shown in eq. 4.

$$Ca_{10}(PO_4)_6(OH)_2+20F^- \longrightarrow 10CaF_2+ 6PO_4^{3-}+ 2OH^- \qquad [4]$$

Therefore, these studies indicated that fluorapatite or hydroxyfluorapatite is the resulting product of electrostatic interaction or ion exchange reaction. Fluorapatite, which has very low solubility, is the compound of fluoride found in the mineral part of bones and teeth, and that play a significant role in strengthening them if present in small quantities. However, at high fluoride concentration the conversion of a large amount of the hydroxyapatite into less soluble fluorapatite (K_{sp}, FAp = 3.16×10^{-60}, K_{sp}, HAp= 2.34×10^{-59}) favors the condition of making the teeth denser, harder and more brittle, also known as dental fluorosis and in extreme case skeletal fluorosis.

1.3. Health effects of fluoride: World and the Ethiopian scenario

Intake of higher fluoride than the WHO permissible levels increases risk of fluorosis, which has already become a serious threat worldwide. So far many cases of fluorosis have been reported in several parts of the world including Ethiopia, where water sources used for drinking purpose are contaminated with fluoride [45-50]. For instance, groundwater having as high as 4.5 mg/L fluoride has been found in many States of Mexico, and even higher concentration, up to 8 mg/L, was also reported in fluorisis endemic Guanajuato and Sonora States [51, 52], where the prevalence of fluorosis has reached about 60 % [49]. In Southern California Lakeland, the fluoride concentration in groundwater is about 5 mg/L [53], and nearly 23 % of children in the US are suffering from dental fluorosis [54]. In India alone, more than 60 million people including children are suffering with different forms of fluorosis [24]. In Ethiopia sources from various studies have shown that the fluoride level in the groundwater of the Rift Valley area used by most rural communities for drinking purpose may reach about 36 mg/L [17, 55, 56]. In the early 1980s, the World Health organization predicted that more than 260 million people worldwide were dependent on drinking water with a fluoride concentration of higher than 1 mg/L [4, 57]. According to the latest estimates, globally more than 200 million people consume drinking water with a fluoride concentration higher than the permissible 1.5 mg/L level [46, 58], the majority of which live in tropical regions, fourteen countries in Africa, eight in Asia, and six in the Americas [55, 59] (Figure 1) with the worst situation occurring in India [60], China, Sri Lanka and the countries of the Rift Valley, in particular Kenya, Tanzania, and Ethiopia [4, 14, 61].

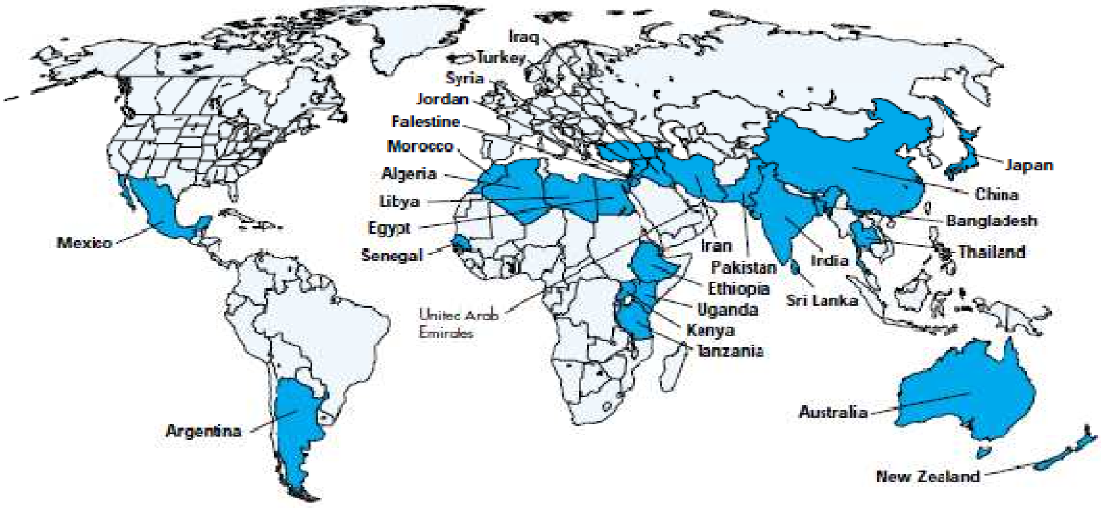

Figure 1: Geographical area of the world with high risk of fluorosis. Countries in blue have high fluoride concentration >1.5 mg/L in drinking water

It is already known that Ethiopia is one of the countries in the world where a significant percentage of the population suffers from the consumption of fluoride rich drinking water. As shown in Figure 2, the scope of fluoride distribution is very wide and spread throughout all regions, though the potential concentrations in the Rift Valley region is very high [62]. As a result of this, a significant number of studies have been conducted in this region since the existence of fluorosis was first identified in the country in 1962 [63]. The findings of these studies indicated that water is the major contributor to the total daily fluoride intake in human body [22, 47, 56, 64, 65]. By now it is well known that a significant amount of population living in the Rift Valley region are consuming groundwater with fluoride concentrations exceeding the WHO permissible levels [17, 45, 47, 56, 66-68], that reached in some places up to 26 mg/L [56], indicating the presence of very high risk of fluorosis in the region.

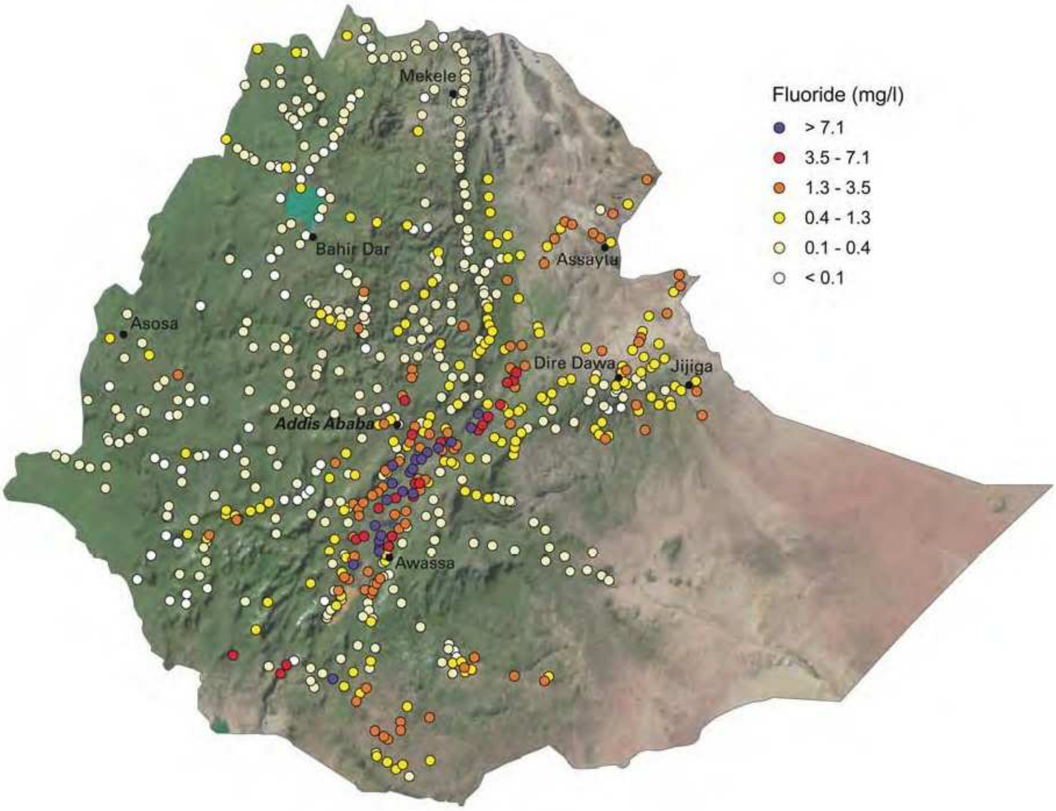

Figure 2: Fluoride concentration profile in drinking water sources of Ethiopia

There are several reports regarding the incidences of fluorosis in this region. R. Tekle-Haimanot et al. [17] reported the prevalence of dental fluorosis that accounts to more than 80 % of the sampled children living in the Rift Valley of Ethiopia (1,221 out of 1,456). In another similar study in children living in the Rift Valley areas conducted by F. Wondwossen et al. [67] reported even alarmingly very high, 91.8 % in moderate-fluoride area (0.3–2.2 mg/L), and 100 % in high fluoride area (10–14 mg/L), prevalence of dental fluorosis. The latest study result by R. Tekle–Haimanot et al. also showed the increasing tendency of dental fluorosis in children, reported over 80 %, and significant cases of skeletal fluorosis, mainly among older people. This study also indicated that more than 41 % of drinking water sources in the Ethiopian Rift Valley are fluoride contaminated. The report also recorded the highest fluoride concentration in Ethiopia in Lake Shala Rift Valley (264.0 mg/L) [47]. The highest fluoride concentration ever found in natural water was reported in lake Nakuru [23, 69], 2800 mg/L in the Kenyan Rift Valley .

Despite the presence of high fluoride in groundwater that is used for human consumption, lack of suitable infrastructure for treatment makes this region one of the most affected by fluorosis [16, 18]. The actual number of people affected by fluorosis is not known, but according to the Ethiopian Ministry of Water Resources estimates, more than 11 million people in the Rift Valley region are highly vulnerable to fluoride related problems as they rely on drinking water sources having high fluoride concentrations [63, 65, 70]. Though there are attempts to reduce the total fluoride concentration in potable waters, the mitigation activities in Ethiopia are still at the initial stages.

1.4. Guidelines of drinking water

In areas where alternative options are not feasible, the most prioritized effective fluorosis mitigation means should be defluoridation, i.e. removal of excessive fluorides from drinking water to permissible levels [19, 71]. Taking health effects into consideration, the World Health Organization guidelines followed in most of the nations set the acceptable fluoride concentration in drinking water in the range between 0.5 to 1.5 mg/L [72], above which the occurrence of chronic fluorosis is inevitable. However, national standards can be set based on factors such as climatic conditions, volume of water intake, and diet. For instance, the Australian Drinking Water Guidelines [20] set the recommended maximum acceptable level of fluoride in drinking water at 1.1 mg/L due to hot climatic conditions and similarly, the Indian standards for drinking water [24] set the recommended maximum desirable limit of fluoride in drinking water at 1.0 mg/L, whereas for countries in tropical regions, the recommended fluoride concentration is even lower, about 0.8 mg/L because of the relatively higher water consumption [45]. However, the Ethiopian drinking water quality guideline so far adopts the WHO maximum limit, despite the presence of hot climatic conditions in flourosis endemic Rift Valley region.

1.5. Overview of defluoridation techniques

If the community water sources used for human consumption found to have higher fluoride concentration than the permissible level, the first remedial measures to combat fluorosis should be to search for water sources with a lower fluoride level, if any or else blending multiple water sources that can lower to WHO guideline values is another alternative [6], harvesting rainwater, and provision of bottled water, at least for young children or pregnant women, again if possible. In cases where these alternatives are not available, or limited, like in the case of Ethiopian Rift Valley region, and where the groundwater to which communities at large depend on is often greater than 10 mg/L [12, 18], defluoridation of drinking water is the sole option remaining to prevent fluorosis [19, 71].

Over the years, various defluoridation methods have been proposed to remove excessive fluoride from drinking water and prevent the associated health problems [48, 73]. In general, based on fluoride removal mechanisms the defluoridation methods may be classified as chemical precipitation, ion-exchange, adsorption, and membrane-based mechanisms [48]. However, most of them present certain disadvantages.

Chemical precipitation method: chemical precipitation involves addition of soluble chemicals, such as calcium and aluminum salts to fluoride-contaminated water, and the formation of fluoride precipitates or co-precipitates. The Nalgonda process, which was developed in India by the National Environmental Engineering Research Institute (NEERI) is most widely studied and established precipitation technique. Due to low cost, it has been applied in developing countries including India, Kenya, Tanzania [74] and Ethiopia [63] for defluoridation of water. However, low treatment efficiency, requirement of a large chemical dosage and close monitoring, adverse health effects of dissolved aluminum species in the treated water, and continuous production of a sludge that requires appropriate disposal limit its application at large [16, 63, 75, 76].

Ion exchange method: ion exchange process involves the replacement of ions in solution by counter ions in exchanger surface to maintain electrical neutrality. In the case of defluoridation, fluoride can be removed from water with a strongly basic anion exchange resin containing quaternary ammonium functional groups [48], according to eq. 5.

$$\text{Matrix–NR}_3^+\text{Cl}^- + \text{F}^- \longrightarrow \text{Matrix–NR}_3^+\text{F}^- + \text{Cl}^- \qquad [5]$$

The fluoride ions in solution replace the chloride ions of the resin as it has stronger electro-negativity. The exhausted resin is regenerated with concentrated solution of sodium chloride. In the case of ion exchange, the presence of other anions such as sulfate, phosphate, bicarbonate results in ionic competition, it is relatively costly, and treated water sometimes has a low pH and high levels of chloride.

Membrane based method: the most advanced membrane based processes, used by industrialized countries such as reverse osmosis, electrodialysis and nanofiltration are highly effective for fluoride removal as well as for the production of high-quality water [76] that meets WHO standards. However, their application in developing world, and even in rural and remote communities in the developed world not shining due to very high operational and maintenance cost, system complexity, requirements for skilled manpower, the need for constant supply of electric energy, and membrane fouling in case waters contain high salinity and TDS (total dissolved solids).

Adsorption based method: adsorption based processes, which involve the passage of water through a bed containing adsorbent materials to retain fluoride either by physical, chemical or ion exchange mechanisms, are very attractive due to their effectiveness, convenience, easy availability, simplicity of operation, and economical as well as environmental low impacts [28, 48, 77]. Since the past few years, adsorption is being the most interesting area in defluoridation research that is widely recognized as an ideal and appropriate compared to other defuoridation techniques, particularly for poor communities in developing nations, although not without disadvantages because it is affected by solution pH, the presence of co-anions such as sulfate, phosphate, and bicarbonate, besides, the requirements of regeneration or an appropriate disposal of fluoride-loaded adsorbent materials [48].

1.5.1. Adsorbent materials for defluoridation

The starting point in the development of adsorption-based process is the choice of suitable adsorbent. Several locally available and naturally occurring adsorbent materials have been tried in the past to identify an efficient and economical defluoridating agents [48, 77, 78] such as the most commonly used activated alumina and activated carbon [48], activated clay [60], ceramic materials [79], diatomaceous earth [34], bleaching earth [29], carbonaceous materials produced from coffee grounds [80]. Cheap natural materials such as red soil, charcoal, brick, fly-ash and serpentine [81]or natural zeolites [26, 82,83], hydroxyapatite [37, 39], even banana peel [77] and bone char materials [48] were also tried as effective and low cost adsorbents for fluoride removal, to mention a few.

Defluoridation study in Ethiopia has been started since the first recognition of the fluorosis problem in 1962 [63, 84]. Similar to other developing countries, relatively simple, relatively low cost adsorbent materials such as locally produced aluminium sulphate and lime combination (Nalgonda technique), and imported activated alumina [63, 84] have been used to remove fluoride in the Wonji-Shoa and Methara Sugar Estates since 1962. Locally available cheap clay soils [84], untreated hydrated alumina (UHA) and thermally treated hydrated alumina (THA) obtained from hydrolysis of locally manufactured aluminium sulphate [85], and even waste residue from alum manufacturing process [12] were also tried in the past for fluoride removal. A local non-governmental organization (NGO) called Oromo Self Help Organization

(OSHO) field-tested bone char technology in rural villages of Ethiopian Rift Valley [63] since 2007. In recent years, thermally treated latertic soils [86], locally available cheap natural zeolite [26, 82], aluminium oxide–manganese oxide composite material [50], nanoscale aluminium oxide hydroxide (AlOOH) [65], and Aluminium hydro (oxide)–based (AO) adsorbent [63] for defluoridation of drinking water. These studies reported the low fluoride removal efficiency for natural zeolites and high fluoride removal in the case of AO based adsorbents.

However, the applicability of these methods is limited either due to their low efficiency, high production cost or lack of public acceptance in the case of BC. Therefore, it is of paramount importance to identify adsorbent materials with a compromise between their fluoride removal capacity, social acceptance, as well as cost, in addition to technical including disposal issues for applications in rural communities in developing countries. Adsorbent materials that have been studied in this research work are discussed in the following sections.

1.5.1.1. Natural zeolites

Zeolites are crystalline microporous aluminosilicates with defined three-dimensional structures. Zeolites framework structures can be built by linking in a periodic pattern, a primary or basic building unit, the tetrahedral TO_4 (where T stands for Si or Al atoms), which share oxygen vertices to form different open structures as shown in Figure 3. The tetrahedra are linked together to form cages connected by pore openings of defined sizes, typically less than 1 nm [87], which in turn are connected to form channels of molecular dimensions, properties of interest for a number of applications [88, 89]. The aperture dimensions of a channel are qualitatively determined from the number of tetrahedral atoms (or oxygen atoms) of the n rings that defines the channel. Structures with 8-ring, 10-ring, and 12-ring channel apertures are the most common and are known as small-pore, medium-pore, and large-pore zeolites [90, 91]. This topology can promote reaction rates and selectivity based on spatial constraints, attractive or repulsive interactions between adsorbent materials and pore walls.

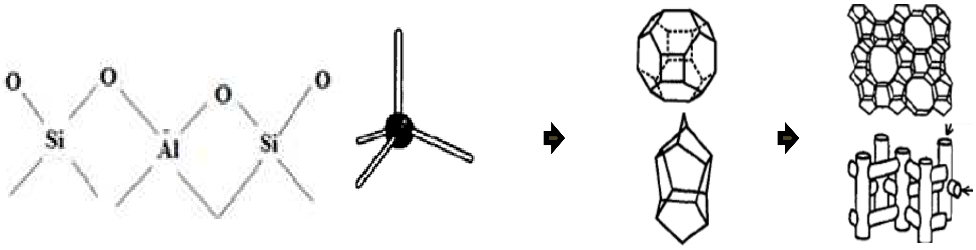

Figure 3: Representations of basic building tetrahedra TO_4 (T, Si/Al) and an open structure cages built from tetrahedra units, and channels of zeolites

Zeolites are found naturally in sedimentary and volcanic areas all over the world. The inorganic network is exclusively composed of Si and Al, with different relative ratios depending on the particular framework topology. The structures of the low silica zeolites are predominantly formed with four, six and eight rings of tetrahedra. One of the chemical properties of zeolites that determine the reactivity is the Si/Al ratio. The composition of the zeolite framework (Si/Al ratio) has a significant effect on the adsorptive properties of the adsorbent such as its acidity, ion exchange capacity and hydrophilicity. The aluminosilicate zeolites based on increasing framework Si/Al composition are classified into four arbitrary categories: (1) “Low” Si/Al zeolites (Si/Al of 1 to 1.5), represented by zeolites A and X are Al saturated, and have the highest cation concentration. (2) “Intermediate" Si/Al zeolites (Si/Al of 2 to 10) consist of synthetic zeolite Y, natural zeolites erionite, stilbite, chabazite and clinoptilolite to mention a few. (3) “High” Si/Al zeolites (Si/Al of 10 to 100), can be generated by framework modification or by direct synthesis; This including zeolite beta and ZSM-5. These materials represent a range of pore sizes from 0.4 to 0.8 nm. (4) “Silica” molecular sieves (Si/Al > 100), consists typical of silicalite [92]. For example, the acidity tends to decrease in strength while the cation concentration and ion exchange capacity, proportional to the aluminum content, increases with decreasing Si/Al ratio [93]. In general, zeolites have a low Si/Al ratio and therefore a high degree of ion-exchange capacity. The Si/Al ratios together with none-framework cations play an important role in determining zeolites chemical properties, as this can be fine-tuned in terms of compositions, cations and framework structure [93, 94].

The incorporation of Al^{3+} in the inorganic framework generates a negative charge on the network, which needs to be balanced by the presence of cationic species. These cations usually contain alkali and alkaline earth metals and are hosted within zeolite minerals. The general formula for a zeolite can be written as: $M_{2/n}$: Al_2O_3:$xSiO_2$:yH_2O, where M is the charge balance cation, n is the charge of the cation, x is generally ≥ 2, and y is the water in the voids of the zeolites [95]. Other cations can also exchange the extra framework cations in zeolite microporous structure easily, and this is one of the main applications of these minerals as an ionic exchanger. Indeed, they are used world-wide as cationic exchangers, even as adsorbents in water and wastewater treatments [96]. Some of the main applications of zeolites in this area include the selective treatment of sewage water, the extraction of ammonia, odor control, heavy metal extraction from nuclear, mining and industrial waste, soil conditioning for agricultural use and even as an additive to animal feed stock [97]. Among these applications of natural zeolites, we are especially interested in the potential use of this mineral as a cheap and locally available fluoride adsorbent

[26], because the occurrence of groundwater containing high concentrations of fluoride is extensive in Ethiopia and is an endemic problem that needs to be tackled urgently.

From our previous study on “Natural zeolites from Ethiopia for elimination of fluoride from drinking water” stilbite zeolite was identified among others for its high calcium contents [26]. The ion-exchange of this sample was studied to find the possibility of exploitation of this calcium zeolite and to understand its significance in the intended application as fluoride removal either directly [26, 82] or in its modified version, as the support precursor for the controlled growth of hydroxyapatite, other active fluoride removal face, on its surface [98].

The stilbite family with the STI framework type [99] consists of three minerals with the same framework topology, but different extra framework cation compositions and symmetries: barrerite, stellerite and stilbite. The framework of stilbite has two kinds of interconnecting channels, 10-ring channels and smaller 8-ring channels (Figure 4). A cavity, which also contains 5-rings and 4-rings, is formed at the intersection of these channels [99].

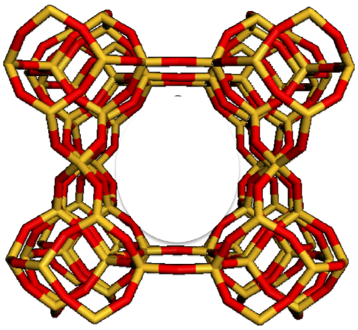

Figure 4: The framework of stilbite zeolite

The dehydration of stilbite has been studied in detail, because it is thought to involve a partial collapse of the framework as a result of the approach of the strongly polarizing extra-framework cations to the zeolite walls [100]. Early attempts to stabilize the stilbite structure involved the investigation of the stabilizing effect of cations on the crystal structure [101].

Although many research works have dealt with low cost defluoridation methods, attempts made to evaluate zeolites for defluoridation are very limited in spite of the fact that they have the properties necessary for a good adsorbent [48]. The result of a recent study by L. Gómez-Hortigüela et al. also revealed the low adsorption capacity of zeolites for fluoride anion [26, 82], in similar pattern with other low cost natural minerals. This is because zeolites in general have negative surface charges at all pH values, predominantly cation exchanger and we need anion exchangers. So they have to be modified [26, 48]. Here, many researchers are involved in zeolite surface modification research, and they indicated the possibilities to enhance the capacity for anions through surface charge reversal by the impregnation of their surface with multivalent cations [28, 102, 103]. Of these, a pioneer attempt made by M.S. Onyango et al. to exchange an extraframework Na^+ ions usually present in zeolite by multivalent ions of Al^{3+} or La^{3+} was successfully accomplished by yielding of modified zeolites with greatly improved fluoride removal capacity. Here, in the La/Al-zeolite modifications, Na^+ ions in Na-bound zeolite are exchanging with Al^{3+} or La^{3+} ions to create active sites for fluoride sorption attributed to more surface positive charges generated due to the incorporation of the multivalent cations [102]. This is confirmed by the point of zero charge (PZC) determination, which in the case of Al^{3+} and La^{3+} exchange zeolites appeared at 8.15 and 4-5.25, respectively, indicating that at pHs below these values, the zeolites are positively charged, thus resulting in an increased attraction of the negatively-charged fluoride anions, and a consequent higher defluoridation capacity. Furthermore, higher defluoridation capacity for Al-treated zeolite was reported as compared to La-treated zeolite, indicating their differences in F^- removal mechanisms, suggesting the chemical adsorption in the case of Al-treated zeolite. Similarly, S. Xingbin et al. carried out modification studies on natural stilbite using trivalent Al^{3+} cations [104], this also reported enhanced fluoride adsorption capacity for the Al-modified zeolite. Other studies have also shown an increased defluoridation capacity after zeolites pretreated with various multivalent cations, Zr^{4+}, Fe^{3+} or Ca^{2+} exchanged zeolites [83, 105-108]. Thus, it is possible to use zeolites in fluoride removal application, especially if subjected to suitable pre-treatments. In this study the defluoridation potential of locally available natural calcium rich stilbite zeolite obtained from Ethiopia as raw, and its modified version, nanhydroxyapatite/stilbite composite (nHAST) has prepared using stilbite as calcium reagent as well as a support to grow nano hydroxyapatite on its surface has been explored.

1.5.1.2. Hydroxyapatite

Following human metabolism, where fluoride is removed from water and taken up by our teeth and bones through the hydroxyapatite component, one of the most widely tested adsorbents has traditionally been hydroxyapatite (HAp), $Ca_{10}(PO_4)_6(OH)_2$ [37, 39]. It is a double salt of tri-calcium phosphate and calcium hydroxide and the principal inorganic constituent of human bones and teeth (Figure 5). Over the past three decades, researchers have studied several aspects of the uptake of fluoride ions by tooth enamel and synthetic HAp [37, 109, 110]. The surface of HAp has a remarkable capacity for retaining fluoride ions from an aqueous solution because of the presence of exchangeable hydroxide anions. In fact, due to the higher stability of fluorapatite (where hydroxide is replaced by fluoride, $Ca_5(PO_4)_3F$, $K_{sp}= 3.16x10^{-60}$) compared to hydroxyapatite ($Ca_5(PO_4)_3OH$, $K_{sp}= 2.34x10^{-59}$), such hydroxide anions of HAp can be exchanged by fluoride anions, resulting in a fluoride removal material.This process is governed by factors such as fluoride, calcium and phosphate ion concentration of the solution, its pH, exposure time, temperature and the nature of the apatite surface [111].

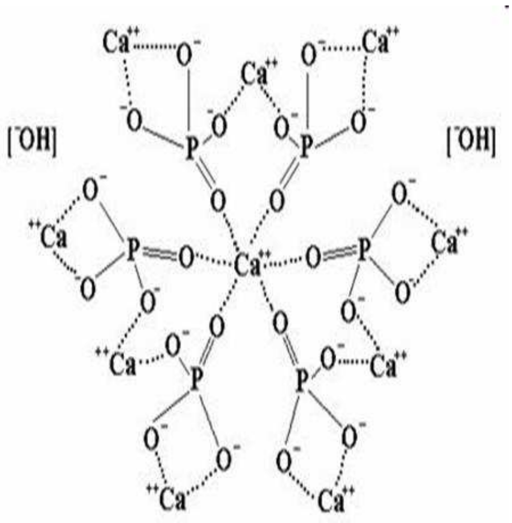

Figure 5: Crystal structure of hydroxyapatite

Bone char (BC), is a natural HAp material produced by an incomplete combustion (charring) at a relatively high temperature (500 to 600 °C) of animal bones to remove all the organics. It contains a porous matrix rich in surface ions, mainly about 57 to 80 % of calcium phosphate ($Ca_3(PO_4)_2$), 6 to 10 % of calcium carbonate ($CaCO_3$), and about 7 to 10 % activated carbon that allow adsorption or ion exchange to occur [6].

Bone char is a commonly used adsorbent in developing countries for defluoridation of drinking water, mainly due to economic reasons, and has been studied by several researchers [112-115]. Despite the encouraging results obtained from high-quality bone char materials, this adsorbent has important disadvantages. The hygienic problem and the low adsorption capacity of the poor-quality bone char, which are a direct consequence of the crucial preparation method, as well as cultural and religious objections, are the major barriers that limit its usage on a large scale throughout the world. For these reasons, considerable number of studies have dealt with various types of other adsorbent materials, of which synthetic hydroxyapatite remains as the main candidate due to its identical chemical composition, non-toxicity, availability and high defluoridation ability [39, 41, 44, 116, 117].

Although HAp has shown an excellent potential towards the retention of fluoride from water, current research is applied in an attempt to further enhance its fluoride-removal capacity through the production of nano structured HAp materials. When the crystals are in the nano-range, the surface properties, electronic structure, coordination, etc., get modified enhancing their performance [37, 118]. In this context, a significant number of nanohydroxyapatite (nHAp) adsorbents have been synthesized and studied for fluoride removal from aqueous solution, the results of which could definitely give a new dimension in the field of the defluoridation as it showed significantly higher defluoridation capacities [37, 42, 117-120].

Nevertheless, the potential application of these materials in the field is not easily achievable, due to the cost associated with their production and significant pressure drops during filtration owing to the small particle size. To overcome such permeability problems and at the same time utilize the advantages of nHAp, it is essential to prepare adsorbents based on nHAp in a usable form by combining them with other high-surface materials [38, 120-122]. By having the HAp nanoparticles not free but supported on the external surface of a material with a large particle size, we provide mechanical stability, and thus avoid pressure drops associated with the nanosize of HAp, as well as prevent the potential toxicity typical of nanoparticles and possible sintering (and loss of efficiency) of the HAp nanoparticles during defluoridation.

There are several methods of synthesizing hydroxyapatite materials such as, precipitation [37, 38, 44, 117, 122, 123], sol gel [124, 125], microwave technique [42], ultrasonic and microwave combined technique [120]and hydrothermal methods [126]. Among these, the precipitation route, which involves the crystallization of HAp from solution reaction mixture of calcium saltsthat provide Ca^{2+} and phosphates in the presence of basic solutions such as ammonia, appears to be the most widely used technique for the preparation of HAp materials, because it is very simple, cost effective and eco-friendly that makes the process easily acceptable by the users. In addition to this, it is indicated that relatively large amount of HAp can be produced using this technique at a reasonable cost [123]. In order to obtain homogeneity and stoichiometry of the resulting hydroxyapatite, this method usually needs diluted solutions and long time (days) for complete reaction [124]. However, in most cases they employ systems that involve high temperature and basic high pH conditions, pH 9 or higher that require extra cost, or environmentally unfriendly solvents [37, 38, 42, 44, 98, 117, 124].

Based on the fact that hydroxyapatite was crystallized out from the reaction mixture of calcium salts, which provide Ca^{2+} and phosphate salts in basic media, L. Gómez-Hortigüela et al. recently reported the synthesis of HAp on stilbite surface (stilbite/hydroxyapatite composite), in the reaction carried out between phosphate source and Ca-rich natural Ehiopian stilbite in the presence of ammonia solution to keep pH of crystallization at 9 [98]. This study described the crystallization of HAp on the external surface of stilbite as an ion exchange of Ca^{2+} ions from stilbite by NH_4^+ in the synthesis medium. According to this study, such exchange leads to a controlled release of Ca^{2+} ions to the surface of the zeolite, which in the presence of phosphate and at the suitable pH precipitates as nanohydroxyapatite on the external surface of the zeolite. This technology was protected by a patent, and thus the current research work conducted in my thesis is mainly devoted to the optimization of the synthesis conditions using stilbite from Ethiopia.

1.5.1.3. Hydrotalcite

Hydrotalcites, HTs also known as layered double hydroxides (LDH), are anionic clays with positively charged octahedral hydroxide layers, which are neutralized by interlayer anions and water molecules, (Figure 6).The general formula of HT is $[M^{2+}_{1-x}M^{3+}_{x}(OH)_2]\ (X^{m-})_{x/m}\cdot nH_2O$, where M^{2+} and M^{3+} are di-and trivalent cations, respectively, X^{m-} is an anion whose charge is m-. The replacement of divalent cations by Al^{3+} in HT framework generates a positive charge on the network, which is balanced through the intercalation and adsorption of compensating anions, such as CO_3^{2-}, SO_4^{2-} and NO_3^-, situated in the interlayer space. Because there is no overall charge, hydrotalcites are quite stable.

The nature of the compensating anions, type of divalent cations as well as the M^{3+}/M^{2+} ratio determine key properties such as anionic exchange capacity, stability under different pH conditions, surface area and acid-base properties of hydrotalcites [127]. They have a so-called “memory effect”, where a material can be thermally treated to remove water, hydroxyl, and carbonate units from its matrix, then rehydrated in an aqueous solution to recover their original layered structure in the presence of appropriate anions [128, 129].

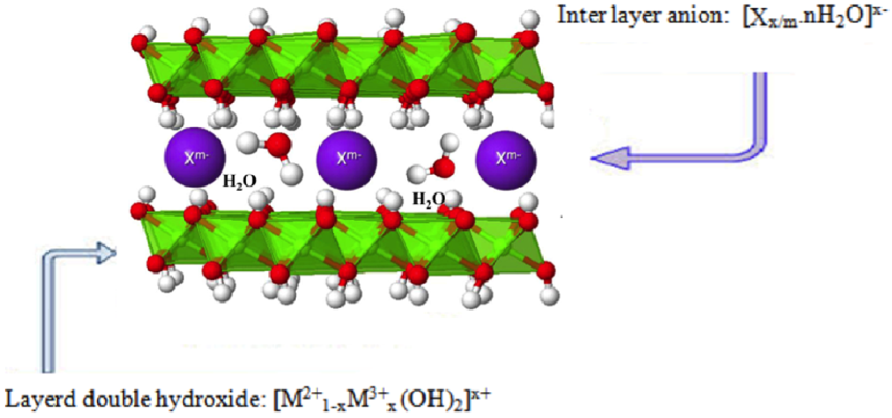

Figure 6: Structural representation of hydrotalcites

Researchers have already started using the advantage of this anomalous, but interesting property of calcined hydrotalcite, cHT in fluoride removal from water. L. Liang et al. among others have shown that cHT can be used effectively for fluoride removal from aqueous solutions through memory effect mechanism [129, 130]. The exceptional property of cHT is that when they are exposed to water and a source of anions, the HT structure is recovered, incorporating anions and water.

1.6. Rationale of the study

Fluorosis is known to be endemic in the Ethiopian Rift Valley that already imposes a great health impact insignificant number of people. Studies have shown that more than 11 million living in this region are affected by flourosis [63, 70]. Despite the widespread awareness of the problem among local water agencies, specifically rural communities at large still rely primarily on fluoride rich groundwater sources for both drinking and domestic uses. The scarcity of suitable infrastructure such as affordable water supply systems or the absence of other alternative safe water sources on the top of very low economic development aggravated the situation and makes the region one of the most affected areas by fluorosis [18, 47]. This dictates not only the seriousness of the problem, but the need for an immediate solution, possibly using defluoridation technologies to remove excessive amount of fluoride from drinking water.

Commercially available, most advanced defluoridation methods, which claimed to be highly efficient and recently used by industrialized countries such as adsorption by reverse osmosis, electro dialysis, and ion-exchange process require more technical support for operation and maintenance besides the high initial cost for installation [50]. However, the adsorption processes is found to be preferred and most promising for poor communities in developing countries in terms of running costs, availability of various adsorbent materials, effectiveness, simplicity and ease of operation as well as environmental low impacts [28, 48, 63, 77].

In line with this, in Ethiopia, mitigation measures based on activated alumina, Nalgonda technique since the early identification of flourosis, and in recent years, bone char technology has been implemented at community level in this hotspot Rift

Valley region. However, at present almost all of them are non-functional, mainly due to poor operation and maintenance, lack of chemicals and capacity to manage the plants by the community, besides the known religious and cultural reasons in the case of bone char.

This, and the widespread of fluorosis in the Rift Valley region of Ethiopia motivated us to do this research work with the focus on the development of socio-economically equitable and efficient alternative defluoridation technology based on the use of locally available, cheap natural minerals from the country, stilbite zeolite in this case [26].

Ethiopia has vast natural deposits of zeolites, which are mostly unexploited because there is a lack of scientific knowledge, available manpower with a geology background and the means to initiate the systematic exploitation of this resource. Previous studies showed abundant resources of mordenite and clinoptilolite zeolites near Adama [131], and phillipsite and also clinoptilolite zeolites in the Hawassa area [132]. One latest survey has also revealed the presence of large deposits of pure stilbite zeolite, which possesses the STI structure type [99], in the northern Tigrai region of Ethiopia as shown in Figure 7 [26, 133].

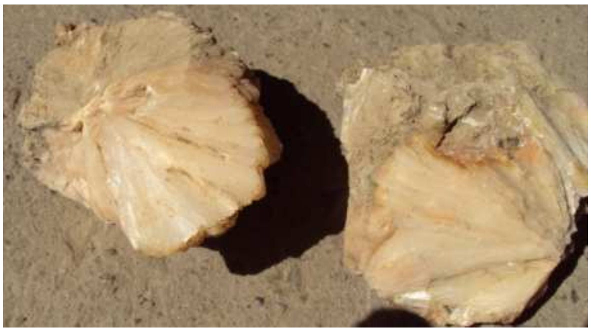

Figure 7: Picture of natural stilbite rock sample from Ethiopian

Recently, researchers at the Chemistry Department, AAU, Ethiopia and the Instituto de Catálisis y Petroleoquímica, CSIC, Madrid, Spain, have shown the limitation (poor defluoridation performance) in Ethiopian natural zeolites [26, 82]. However, in another study they proposed an interesting option based on one of these zeolites, natural stilbite for the development of high performing nanohydroxyapatite for fluoride removal. Here the stilbite zeolite simultaneously plays a dual role: a support material that hold nHAp, and a Ca reagent (a source of Ca) in its reaction with phosphate salts for the growth of nHAp, to produce a stilbite/hydroxyapatite composite material [98]. They proposed that Ca^{2+} ions are first ion-exchanged by NH_4^+, thus being released to the solution, which, in the presence of PO_4^{3-} and at the pH 9, leads to a precipitation of HAp on the zeolite surface. However, as we understand from this work, optimization of synthesis conditions of the stilbite/hydroxyapatite composite is no completed. Therefore, further optimization work was planned in order to finalize the remaining work to identify the best combination of synthesis conditions for composite preparation. In the present study the best performing stilbite/hydroxyapatite composite, nHAST in this case, is reported at an autogenous pH of 8 (pH of only solution mixture of stilbite and phosphate reagents, without the addition of base), unlike the common precipitation methods of HAp preparation, which in many cases carried out at high temperatures and basic pH conditions, often higher than 9 [37, 38, 42, 44, 98, 117].

In addition to this, further study on the effect of process parameters for the composite sample synthesized at the optimized best conditions is highly required for any new adsorbent materials before it can be used for practical applications [104-106]. Therefore, the most important process parameters that affect fluoride removal from water such as adsorbent dose, initial fluoride concentration, co-ions effect, solution pH effect, and stability have carefully analyzed. Furthermore, in this study, the regenerability of the exhausted nHAST adsorbent has thoroughly investigated. The adsorption kinetics and isotherms has also been studied in order to understand the possible fluoride adsorption mechanisms of this sample, the result of which has been compared with the BC adsorbent that needs replacement.

Therefore, in this work natural stilbite from Ethiopia in fluoride removal application is carefully assessed based on the following research questions:

- Could natural zeolites be applied to the defluoridation system?
- Can we modify zeolites to improve the fluoride removal capacity?
- Could natural zeolites play any other role in the development of fluoride removal technology?
- Would the combination of stilbite zeolite and HAp help in the final development of defluoridation technologies
- Could the synthesis parameters affect the performance of zeolite and HAp composite?
- Is the fluoride adsorption performance of the composite being comparable with the widely tested BC adsorbent in developing nations? From natural resource exploitation point of view, if the application of natural stilbite zeolite based defluoridation method is possible, it must be a focus of attention. Having these questions in mind the following are the objectives of the study.

1.7. Objectives

1.7.1. General objectives

The main objective of this thesis is to develop socio-economically equitable and efficient defluoridation technology based on natural stilbite zeolite from Ethiopia.

1.7.2. Specific objectives

- To test the defluoridation potential of locally available natural stilbite zeolite obtained from Ethiopia;
- To synthesize an efficient, high capacity and a low energy demanding stilbite/hydroxyapatite, nHAST composite adsorbent for fluoride removal using stilbite as a support material as well as a reagent for calcium source;
- To fully characterize the adsorbent materials in order to understand its property;
- To test the performance of nHAST composite in fluoride removal thoroughly;
- To compare the fluoride removal performance of nHAST composite against BC and HAp, this is currently applied as adsorbent in the field in Ethiopia;
- To test the fluoride removal capacity of another HAp based adsorbent, nHT/HA composite, in which the anionic exchanger nanohydrotalcite, nHT is supported on HAp.

Chapter Two

2. Experimental

2.1. Materials and Methods

In this study different adsorbent samples are used. All natural zeolites, synthetic HAp, bone char and hydrotalcite samples were collected from various places. A raw Italian natural clinoptilolite, commercially labeled Zeocat ECO, a clinoptilolite rock from San Luis Potosí (Mexico), a heulandite (greenish) and hydrotalcite samples were from Puebla in Mexico. Natural zeolites, stilbite (Figure 7) and analcime collected from Tigray region in Ethiopia were obtained from the School of Earth Sciences, Addis Ababa University. Synthetic HAp, and bone char samples were kindly donated by the Oromo Self-Help Organization (OSHO) defluoridation plant located at Modjo, Ethiopia. NaOH (99 %, Sigma Aldrich, Germany), HCl (37 % Sigma Aldrich, Germany), NaF (98 %, Merck, Germany), $(NH_4)_2HPO_4$, NH_3(25 %, Sigma Aldrich, Germany), HNO_3 (70 %, Sigma Aldrich, Germany), $NaNO_3$ (99.5 % Sigma Aldrich, Germany), Na_2SO_4 (99.5 %, Sigma Aldrich, Germany), $NaHCO_3$ (99.5 %, Sigma Aldrich, Germany), NaCl (99.5 %, Sigma Aldrich, Germany), TISABIII (CRYSON), EDTA (99.5 %, Sigma Aldrich, Germany), CH_3COOH (99.9 %, Sigma Aldrich, Germany), tri-sodium citrate, deionized water were used in this work. All the chemicals used were at least reagent grade and used with no further purification.

2.1.2. Adsorbent preparation: Synthesis of nHAST composite

All raw samples except the zeolite from Puebla (Mexico) and synthetic HAp, which were obtained as the desired powder form were manually ground with a mortar and sieved to the desired average particle size fraction between 75 µm to 105 µm for experimental studies.

The nHAST composite is synthesized in laboratory as described in [95] as follows: 2.00 g of sieved STI zeolite is added to 30 ml of 1 M $(NH_4)_2HPO_4$ solution in polyethylene plastic bottles and stirred for 10 minutes. The pH of the resulting solution mixture was adjusted to 9 using 25 % of NH_3 solution. Growth of HAp was then carried out keeping the mixture in water bath under static conditions for 19 hours at room temperature. The chemical reactions that could occur during this crystallization time comprise a controlled cationic exchange of Ca from the stilbite zeolite, and a subsequent precipitation of HAp in the presence of a source of phosphorus on the surface of the zeolite, according to eq. 5 to 7.

$$(NH_4)_2HPO_4\ (dis) \longrightarrow 2NH_4^+\ (aq) + HPO_4^{2-}\ (aq) \qquad [5]$$

$$STI\text{-}Ca^{2+} + 2NH_4^+\ (aq) \longrightarrow STI\text{-}(NH_4^+)_2 + Ca^{2+}\ (aq) \qquad [6]$$

$$STI\text{-}(NH_4^+)_2 + 5Ca^{2+}\ (aq) + 3HPO_4^{2-}\ (aq) + 4NH_3\ (aq) + H_2O$$

$$\longrightarrow STI\text{-}(NH_4^+)_2\cdots Ca_5(PO_4)_3OH\ (S) + 4NH_4^+\ (aq) \qquad [7]$$

The adsorbent solid material labeled nHAST composite was separated by filtration, washed thoroughly with plenty of distilled water and dried in an open air at room temperature overnight. Scheme 1 shows the illustration of the preparation procedure. Finally, optimization of synthesis procedural parameters was thoroughly assessed to further increase the capacity of the composite adsorbent as follows:

Scheme 1: A simple illustration for the preparation of nHAST composite

2.1.3. Synthesis procedure optimization for nHAST composite

The crystal size, morphology and the nature of synthetic hydroxyapatite materials are largely affected by the conditions of synthesis procedure such as reaction temperature, synthesis time, crystallization pH and crystallization time. These in turn have an impact on the performance of hydroxyapatite. Therefore, studies on optimization of synthesis conditions for the preparation of nHAST composite was carried out to tune the materials property and upgrade the performance in fluoride removal, of course with respect to the reported precedent literature work [98].

2.1.3.1. Synthesis time optimization

The effect of synthesis time, that is spacing time between the addition of NH_3 solution to the reaction mixture of STI and $(NH_4)_2HPO_4$, in fluoride adsorption performance by nHAST composite was studied by varying synthesis times, 0, ½, 1, 2, 4, 24 and 48 hours and keeping other conditions constant as described in [101] while synthesizing composite samples;two samples were synthesized per each synthesis time, and tested in fluoride removal in batch mode to identify the best performing nHAST sample.

2.1.3.2. Crystallisation pH optimization

To examine the effect of crystallisation pH on the crystal size of HAp grown on stilbite surface, synthesis of composite samples were carried out at the following seven different crystallization pHs: pH 7, 7.5, 8, 8.5, 9, 9.5 and 10, by keeping other conditions constant as described in [98] or at optimized level. The pH values were adjusted to the desired level either with 0.1 M HCl or 0.1 M NaOH. Likewise two nHAST composite samples were synthesized per each crystallization pH, and tested in fluoride removal in batch mode to identify the best performing nHAST sample.

2.1.3.3. Crystallization time optimization

To examine the effect of crystallization time on the fluoride removal by nHAST composite, synthesis of composite samples were carried out at thirteen different crystallization times: 0, 2, 4, 6, 8, 19, 24, 48, 72, 96, 120, and 144hours, again two composite samples were synthesized per each crystallization time, and similarly tested in fluoride removal in batch mode to identify the best performing nHAST sample.

2.1.4. Synthesis procedure and reproducibility test

Under this section, reproducibility of the best synthesis procedure for the preparation of nHAST composite as proposed based on the experimental results stated in Section 2.3, was tested using different composite samples synthesized following proposed synthesis procedure. Note that different stilbite samples, but having similar composition with natural stilbite sample under investigation are used in a similar fashion as a support as well as source of calcium reagent. Finally, their performance in fluoride removal was tested in batch adsorption experiments under the same conditions as nHAST composite, with which their efficiency compared.

2.2. Characterization Methods

Defluoridation activity is largely dependent on the nature and particle size of adsorbent materials. Thus, combinations of different characterization techniques have been used to analyze the chemical composition and structural properties of nHAST composite materials in order to understand them in depth. The techniques used in this study are described below.

2.2.1. Powder X-ray diffraction

X-ray diffraction, XRD is used to determine the degree of crystallinity of solid materials by measuring the diffraction pattern. It provides information about the distribution of atoms (symmetry) found in the solid structure. Each type of crystalline solid have unique characteristic X-ray diffraction pattern, which is utilized as a “fingerprint” for its identification and classification. In this work the XRD patterns of the adsorbent samples were collected with a XRD machine model of X’pert Pro PANalytical diffractometer equipped with an X’celerator detector using a Cu K_{α} radiation and Ni filter, which has a wavelength of 1.54056 Å. The instrument settings for each test at room temperature were: tension (45 kV), current (40 mA), number of steps of 4368, total run time of 19.3980 s, and intervals between 4.0087° to 89.9737°.

2.2.2. Inductively Coupled Plasma, ICP analysis

Analytical spectroscopic techniques such as inductively coupled plasma, optical/ atomic emission spectrometry, ICP-OES or ICP-AES are used in order to determine the concentration of the atomic and molecular species present in the bulk chemical composition of the samples. In our case, the chemical composition of the adsorbent materials have been studied by Inductively Coupled Plasma Optical Emission Spectrometry (ICP-OES), Optima 3300 DV model; digestion of the samples were carried out by alkaline fusion.

2.2.3. Thermogravimetric analysis

Thermogravimetric analyser, TGA is a very sensitive analytical instrument that is commonly employed in research to follow the reaction process based on weight changes as a function of temperature or time. The thermal stability and weight loss of the adsorbent materials were evaluated using a thermogravimetric analyzer, PERKIN ELMER TGA7. Samples were heated at a rate of 20 °C min^{-1} to a maximum temperature of 900 °C under air.

2.2.4. Infrared Spectroscopy

Infrared transmission measurements were carried out in order to analyze the functional groups in the adsorbent materials. In this work an Attenuated Total Reflectance spectrophotometer (ATR, PIKE TECHNOLOGIES) in the range of 500-4000 cm^{-1} with quartz as detector was used.

2.2.5. Electron Microscopy

The crystal morphology of the adsorbent samples were studied by Scanning Electron Microscopy (SEM) using a Hitachi TM-1000 tabletop microscope. In order to corroborate the distribution of elemental composition determined by ICP-OES, stilbite zeolite sample was studied by scanning electron microscopy coupled with Energy Dispersive X-ray Spectroscopy (SEM-EDS). Furthermore, in order to study the atomic structure and the nature of the composite, Transmission Electron Microscopy was applied. Scanning Transmission Electron Microscopy (STEM) was chosen, as it is less damaging to electron beam sensitive materials. The observations were performed on selected nHASTcomposite samples, 19 and 144 hours. Spherical aberration corrected FEI Titan XFEG which was used at 300 kV, equipped with a corrector for the electron probe allowing a maximum resolution of 0.8 Å, the microscope was also equipped with an EDS detector (Energy Dispersive Spectroscopy) and a Gatan Tridiem energy filter for EELS (Electron Energy Loss

Spectroscopy) measurements. Prior to observations, the samples were crushed, dispersed in ethanol or acetone and placed onto a holey carbon copper micro grid.

2.2.6. Nuclear Magnetic Resonance Measurements

Magic Angle Spinning Nuclear Magnetic Resonance, ^{31}P MAS-NMR was used to confirm the presence of HAp in nHAST composite adsorbents. The spectra were recorded at room temperature using a Bruker AV-400-WB spectrometer and a recycle delay of 20 s, while spinning the samples at 162 MHz.

2.2.7. Point of zero charge determination

It is well known that the study of adsorption from solution strongly demands the knowledge of the point of zero charge (PZC), because the ability of the adsorbent materials to adsorb, either anions or cations, is defined by the charge on the adsorbent surface. In this work PZC was measured by potentiometric mass titrations technique [50, 134]. Point of zero charge was identified as the common intersection point (CIP) of the potentiometric curve of the blank solution with the corresponding curves of the impregnating suspensions containing 0.5, 1.0, and 1.5 g of the adsorbent in electrolytic solution (0.02 N $NaNO_3$ in 50 mL of deionized water. The experiment was performed, under a N_2 atmosphere and the aqueous suspensions were equilibrated for 1 h to reach an equilibrium pH value. Small amount of 1 M NaOH was added to make the pH around 11 and recorded as initial pH after 15-20 min. Then the solid suspensions were titrated by 0.1 N HNO_3, using 665 Dosimat (Metrohm, Switzerland). The pH of each suspension was then measured with 1 min time interval using a digital pH meter standardized by buffers (WTW Inolab pH/ION Level 2, Germany).

2.3. Defluoridation studies

Fluoride removal studies were started with the preparation of standard solutions. A 0.1 M fluoride stock solution was prepared by dissolving 2.0995 g of anhydrous sodium fluoride in a 500 ml round bottom volumetric flask with deionized water, from which the samples of initial concentration of 5 and 10 mg/L have been prepared by appropriate dilution in accordance with the real polluted water compositions obtained in Ethiopia for experimental purpose. In particular cases, different initial fluoride concentrations and adsorbent doses were studied.

Following this, an aliquot of 20 ml of fluoride solution of the required initial concentration and the desired weight of the adsorbent material were added in a plastic bottle for batch adsorption studies. After thoroughly stirring the resulting mixture in a magnetic stirrer for 20 hours contact time at room temperature, the samples were filtered, and to the filtrate total ionic strength adjustment buffer, in this case TISABIII solution was added in 10:1 volumetric ratio of filtrate to TISABIII solution in order to maintain ionic strength and the pH, and eliminate the interference effect of complexing ions. In particular cases, different contact reaction times were studied. Finally the equilibrium fluoride concentration was determined using a pH/ISE meter (CRISON GLP 2^2, China) equipped with combination fluoride-selective electrode (CRISON Code 96 55). The pH was measured with a pH/ion meter (CRISON GLP 2^2) using an unfilled pH glass electrode. The residual fluoride concentration was measured according to the procedure described in the instrument manual. The electrode was calibrated prior to each experiment over a concentration range of interest by using pH calibration buffers. All experiments were performed in duplicate and mean values are reported. All measurements were made at room temperature (23 ± 2 ^{o}C). The adsorption efficency (Q_t), was calculated using eqn 8.

$$Q_t = \frac{C_o - C_t}{C_o} \text{ x } 100 \qquad [8]$$

In this study, besides the defluoridation capacity (Q_e) refers to total mass of the composite material, including the zeolite and the HAp, that is calculated following eq. 9, the intrinsic capacity of HAp ($Q_{e\ (HAp)}$), referred only to the percentage of HAp in the composite material was used to describe the relative activity of the adsorbent material with respect to the amount of HAp, and calculated following eq. 10:

$$Q_e = \frac{C_o - C_t}{\text{dose}} \qquad [9]$$

$$Q_{e\ (HAp)} = \frac{C_o - C_t}{\text{Total dose x } \frac{(\text{wt \% HAp})}{100}} \qquad [10]$$

where C_o and C_t refer to the initial fluoride concentration and to the concentration after the elimination process, respectively, and are given in mg/L. The total dose corresponds to the mass of the composite, including zeolite and HAp, per volume of solution to be treated (in g/L), and (wt % HAp) accounts for the weight percentage of HAp in the composite material, calculated following equation 8. Capacities are given in mg of F^- per gram of HAp. The content of HAp (wt %) in nHAST composite material is calculated from the content in P obtained from the elemental analysis p (wt %) by ICP, according to eq. 11.

$$\text{HAp wt \%} = \text{P wt \%}_{(\text{ICP})} \times \frac{502}{93} \qquad [11]$$

where 502 is the total molecular mass of HAp, ($Ca_5(PO_4)_3OH$) and 93 is the molecular mass of P in HAp.

Intrinsic capacity is a concept used in this work along with the usual defluoridation capacity (Q_e) in order to understand the final properties of the nano HAp itself. Using this data we can gather information regarding the activity of the nanocrytals grown on the STI surface. Although an intrinsic capacity does not give conclusive information towards the actual engineering of the process, instead it provides an important clue that can be used for a simple comparison of HAp based adsorbent materials.

2.3.1. Adsorption kinetics and isotherms

Kinetics and isotherm studies were conducted in order to investigate the reaction mechanism of the adsorption process. Such information plays an important role in designing adsorption processes as it provides adsorption capacity of the adsorbent and kinetics of the fluoride-removal process under the studied conditions. Kinetic experiments were carried out using various contact times (0.5, 1, 2, 8, 16, 20, 24 and 28 hours), at a constant dose of 10 g/L and an initial fluoride concentration of 10 mg/L at room temperature under continuous agitation. Adsorption isotherms were obtained using initial fluoride concentrations of 2, 4, 6, 8, 10, 15, 20, 50, 100, and 200 mg/L, and a constant dose of 10 g/L at room temperature under continuous agitation for 20 hours.

In this study, two most commonly used kinetic models were surveyed, that is pseudo first order and pseudo second order reaction mechanisms were applied in order to analyze the experimental data using equations 12 and 13, respectively.

$$\log(Q_e - Q_t) = \log Q_e - \frac{K_1}{2.303} t \qquad [12]$$

$$\frac{1}{Q_t} = \frac{1}{K_2 Q_e^2} + \frac{1}{Q_e} t \qquad [13]$$

where Q_e and Q_t are the amount of fluoride adsorbed at a time t and equilibrium (mg/g), respectively, and K_1 and K_2 are the rate constants of pseudo first order and second order models, respectively.

Although there are a lot of adsorption isotherm models, the two most frequently used models: Langmuir and Freundlich are applied as these give a good description of experimental behavior in a large range of operating conditions. Langmuir model is expressed by the following equation, eq. 14.

$$Q_e = \frac{Q_o b C_e}{1 + bC_e} \qquad [14]$$

where C_e is the equilibrium concentration of the adsorbate (mg/L), Q_e (mg/g) is the amount of adsorbate per unit mass of adsorbent, Q_o is the amount of adsorbate at complete monolayer coverage (mg/g) that gives the maximum monolayer adsorption capacity of adsorbent. Q_o (mg/L) and b (L/mg) is Langmuir constants related to adsorption capacity and rate of adsorption, respectively.

Q_o and b can be calculated from the slope and intercept of the plot C_e/Q_e versus C_e, respectively from the linear form of the Langmuir model, eq. 15.

$$\frac{C_e}{Q_e} = \frac{C_e}{Q_o} + \frac{1}{bQ_o} \qquad [15]$$

The affinity between F^- and the adsorbents can be predicted using the Langmuir parameter b from the dimensionless separation factor R_L, as shown below.

$$R_L = \frac{1}{1 + bC_o} \qquad [16]$$

where C_o is the initial F^-concentration and b is Langmuir isotherm constant. The value of R_L indicates the type of isotherm to be either unfavorable ($R_L > 1$), linear ($R_L=1$), favorable ($0< R_L< 1$), or irreversible ($R_L = 0$).

The Freundlich model is expressed by the f non-linear equation (eq. 17). The constants K_F and n are obtained from the intercept and the slope of the linear plot, respectively (eq. 18).

$$Q_e = K_F C_e^{1/n} \qquad [17]$$

$$\log Q_e = \log K_F + \log C_e \qquad [18]$$

where K_F and n are the indicators of adsorption capacity and adsorption intensity, respectively.

2.3.2. Effect of process parameters on fluoride adsorption by nHAST

To examine the effects of the adsorbent dose, initial fluoride concentration, contact time and solution pH, a series of batch adsorption experiments were conducted on the selected nHAST composite sample that exhibited better adsorption capacity. Adsorption was performed by varying any one of the parameters, while keeping the others constant.

The effect of adsorbent dose of adsorbent on fluoride removal was studied by varying the dose from 20 g/L up to 100 g/L in test solutions containing initial fluoride concentration of 10 and 20 mg/L in the case of raw stilbite zeolite, whereas in nHAST composite and BC adsorbent samples, the adsorbent dosages were in the range between 4 to 12 g/L (4, 6, 8, 10 and 12 g/L) using test solutions containing initial fluoride concentration of 5 and 10 mg/L at constant reaction time of 20 hours with stirring continuously at room temperature. The effect of initial fluoride concentration and contact time were investigated for both nHAST composite and BC samples by varying initial fluoride concentrations and contact time from 5–200 mg/L and from 0–28 hours, respectively at an optimized adsorbent dose of 10 g/L. The effect of solution pH on the adsorption of fluoride on to the adsorbent was studied by varying the solution pH from 3 to 10. The pH was adjusted to the desired level either with 0.1 M NaOH or 0.1 M HCl. Similarly, batch mode adsorption experiments were carried out using initial fluoride concentration of 10 mg/L and 10 g/L adsorbent dose with stirring continuously for a contact time of 20 hours at room temperature conditions. The effect of co-existing anions (HCO_3^{-}, SO_4^{2-} and Cl^{-}) on fluoride adsorption was studied in the presence of anions that commonly exist in groundwater [135]. The solutions of a series concentration of each target anion (0–500 mg/L) were prepared by dissolving the sodium salts of the respective anions in de-ionized water containing 10 mg/L fluoride solution. The solution pH was determined. Then, 10 g/L of adsorbent material was added and allowed to equilibrate for 20 hours contact time under continuous mixing conditions at room temperature (23 ± 2 °C). The equilibrium fluoride concentration and pH of the solution were determined in the supernatant after filtration as described in section 2.3.

2.3.3. Regeneration experiments

To evaluate the reusability of the adsorbent composite after one removal treatment, prior to regeneration successive defluoridaton treatments were performed to exhaust the material until fully saturated. For this, the adsorbent loaded with fluoride obtained in the previous process is subjected to a new fluoride removal process under the same conditions in batch adsorption experiments, until no further adsorption of fluoride. Regeneration of exhausted nHAST composite was carried out using mild NaOH solutions as follows: 0.50 g of the exhausted composite material is added to 100 ml of 0.01 or 0.1 M NaOH solutions. The mixture is continuously stirred for a contact time of 24 hours or 9 hours (for successive 3 hours treatments each, 3x3 hours, a total of 9 hours) in 0.01 M. and 0.1M NaOH solutions, respectively. The solid regenerated adsorbent thus was filtered off, and washed with water until the washing water has a neutral pH. This regenerated adsorbent is then subjected to same adsorption experimental study in order to test its capacity.

2.3.4. Scaling-up nHAST synthesis and using recovered filtrate solutions

To complete the way to practical application, further experiments on scaling-up were performed based on the best optimized synthesis procedure. Initially, the scaling up experiment was planned to reach the amount of the nHAST composite production to 250 g from the initial 2 g laboratory level. Moreover, in the course of scaling-up, a series of different nHAST adsorbents (nHAST-1, nHAST-2, nHAST-3) are synthesized using the recovered ammonium phosphate (AP) filtrate solutions, which otherwise are a thrown waste material. This is another cost reduction steps besides the environmental law impact perspectives. Here, the initial nHAST composite was labeled as nHAST-0 to differentiate from the other. Illustration of scale-up production process is presented in the result section, refer to Scheme 2 in page 115.

Chapter Three

3. Results and Discussion on Natural Zeolites

3.1. Characterization and Defluoridation test

3.1.1. Powder X-ray diffraction analysis

The diffraction pattern of the natural zeolite sample collected in the Hashenge basalt corresponds to the stilbite family of zeolite minerals (Figure 8) [99]. Stilbite family is composed by three differentiated types of minerals: barrerite ($Na_8(Al_8Si_{28}O_{72})\cdot 26H_2O$), stilbite ($NaCa_4(Al_9Si_{27}O_{72})\cdot 30H_2O$) and stellerite ($Ca_4(Al_8Si_{28}O_{72})\cdot 28H_2O$) [99], which share the same framework topology, but differ in the cation composition and, consequently, in their space group. Barrierite and stellerite are the sodium and calcium-rich end members of the family, respectively, with orthorrombic space groups, and stilbite has a mixture of sodium and calcium, and has a monoclinic space groups. These three minerals can be easily distinguished by their XRD in the 23-24 2θ (°) region: the presence of three differentiated peaks indicate that the phase we have is stilbite [82, 136].

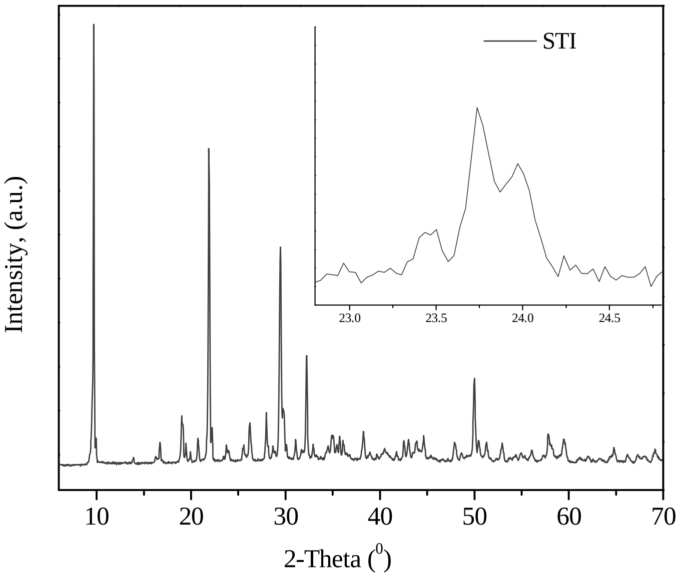

Figure 8: XRD pattern of STI zeolite

3.1.2. Thermogravimetric analysis.

Thermogravimetric analysis was carried out on the support STI zeolite sample. The analysis result, which described as TGA-DTG curves, is presented in Figure 9. As shown in the figure, three differentiated weight losses can be observed, the first weak desorption peak at temperatures below 130 ºC, corresponding to loosely bound water molecules, and two other with temperatures of maximum desorption rate at around 175 and 250 ºC, corresponding to strongly adsorbed water molecules with in stilbite framework structure.

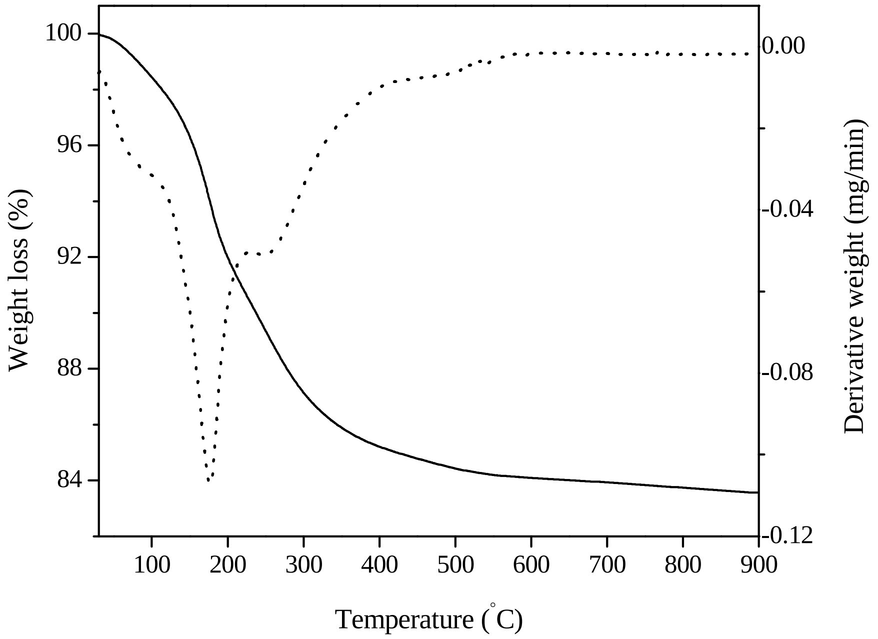

Figure 9: TGA (solid line) and DTG (dotted line) of the STI sample

3.1.3. ICP elemental composition studies

Stilbite samples contain Si and Al as tetrahedral framework atoms, and monovalent and divalent extra-framework cations that compensate for the negative charge introduced by the replacement of Si^{4+} by Al^{3+}. Ca and Na are the most common extra-framework cations; K and Mg are also observed, but to a lesser extent. In the stilbite series of minerals, by far the most common composition is that known as Ca-stilbite, referring to the predominant extra-framework Ca cation. Typically Ca-stilbite contains four Ca and a small amount, less than two of Na, of cations per unit cell. Only a few Na-stilbite samples are known, and these have Na in excess of four and Ca between 1 and 2 cations per unit cell. The H_2O content depends on the number of cations in the channels. Ca-stilbite usually contains between 28 and 30 H_2O molecules per unit cell, while Na-stilbite has 25 to 26 [137]. The ICP elemental analysis result of STI sample indicated the presence of high Ca (4.9 %), confirming that stilbite has a higher affinity for divalent cation in accordance with the common observation of the stilbite mineral, and significant amount of Na (0.5 %) content as shown in Table 1, very similar composition to the previously reported literature value for natural stilbite from Ethiopia [82]. Some impurities were detected in the chemical analysis: 0.5 wt. % of lithium and 0.16 wt. % of iron, both elements too light to be detected by X-ray diffraction.

Table 1: ICP chemical composition analysis of STI sample

Sample	**Element**	Al	Si	Ca	Mg	Fe	K	Na	Li
STI	(% wt)	8.0	20.4	4.9	0.16	1.6	0.3	0.5	0.5
	mol	0.296	0.729	0.123	0.007	0.029	0.008	0.022	0.071
	mol.ratio	1	2.5	0.4	0.02	0.1	0.02	0.07	0.24

The experimental chemical composition of the stilbite sample was also very similar with the theoretical composition. The experimental Si/Al and Al/Ca ratio as calculated from the experimental data in Table 1 was found to be 2.5 and 2.5, respectively, while the theoretical ideal composition, deriven from the stilbite ideal chemical formula of $NaCa_4(Al_9Si_{27}O_{72})\cdot 30H_2O$, is 3 and 2.25, respectively.

The morphology of STI sample was studied by SEM-EDX [82]. Figure 10 shows an EDX-mapping of the sample. It can be observed that the composition is nearly homogeneous, showing quite a uniform distribution of the framework atoms, Si, Al and O, and also of the extra-framework atoms, Ca and Na.

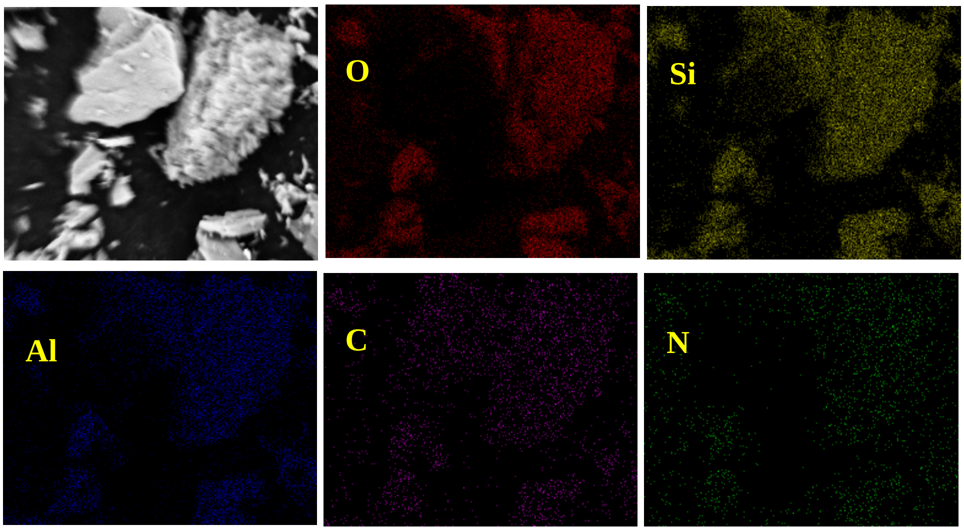

Figure 10: SEM-EDX mapping of STI sample

3.2. Defluoridation test

The main purpose of this study was to test the potential of natural stilbite from Ethiopia for useful local applications. As previously mentioned, our particular interest is in defluoridation of fluoride contaminated water based on the use of calcium from calcium rich Ethiopian natural stilbite (refer to Table 1) through CaF_2 precipitation, according to eqns. 19 and 20, assuming that the Ca^{2+} is transferred into the solution from the STI framework by ion-exchange with Na^{+}(F^{-} is present as NaF in the solution).

$$\text{STI-Ca}^{2+} + 2\text{Na}^{+}\,(aq) \longrightarrow \text{STI-(Na}^{+})_2 + \text{Ca}^{2+}\,(aq) \qquad [19]$$

$$Ca^{2+}(aq) + 2F^{-}(aq) \longrightarrow CaF_2\ (\downarrow) \qquad [20]$$

Adsorption studies were carried out in batch mode using specified amount of an adsorbent material of various doses (20, 40, 60, 80 and 100 g/L) at 5 and 20 mg/L initial fluoride concentrations and 20 hours contact time continuously agitating on magnetic stirrer at room temperature, Figure 11.

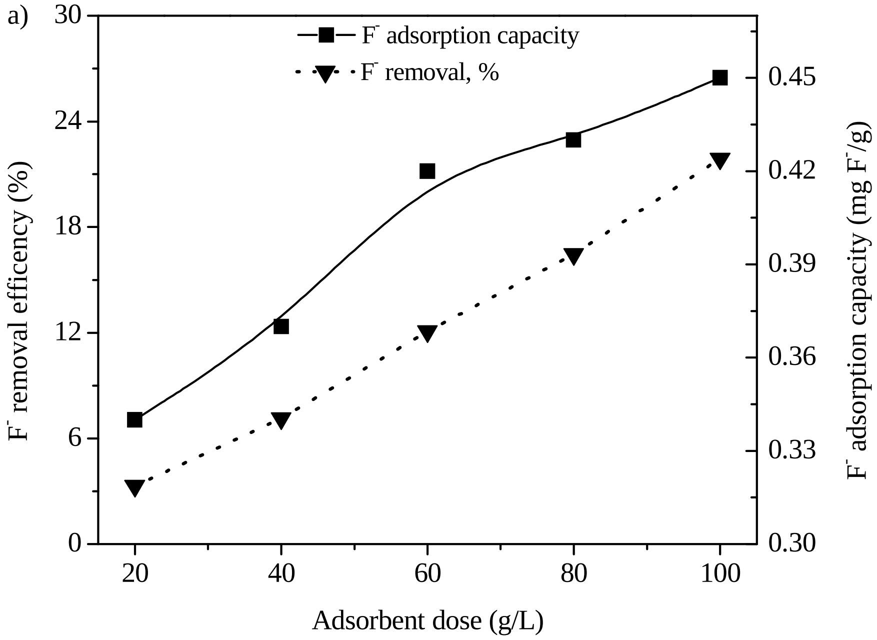

As observed in Figure 11a, the natural stilbite shows a very low fluoride removal capacity; only 0.45 mg F^-/g maximum defluoridation capacity was recorded from initial F^- concentration of 20 mg/L at such a very high adsorbent dose of 100 g/L. This is possibly ascribed to inefficiency or a failed ion exchange of the Ca^{2+} ions by Na^+ ions in the solution. However, the fluoride removal efficiency increases as a function of adsorbent dose. A maximum of about 22 % of F^- ion removal can be achieved from solutions with initial concentration of 20 mg/L using a dose of 100 g/L. More interestingly, about 30 % of F^- ion is removed from a solution with initial concentration of 5 mg/L at the same dose, Figure 11b.

Nevertheless, in both cases the equilibrium final fluoride concentrations remain high, 16.09 and 3.52 mg/L from initial fluoride concentrations of 20 and 5 mg/L, respectively, significantly higher than WHO maximum limit, 1.5 mg/L. This indicates that natural STI from Ethiopia is not an effective adsorbent for fluoride removal.

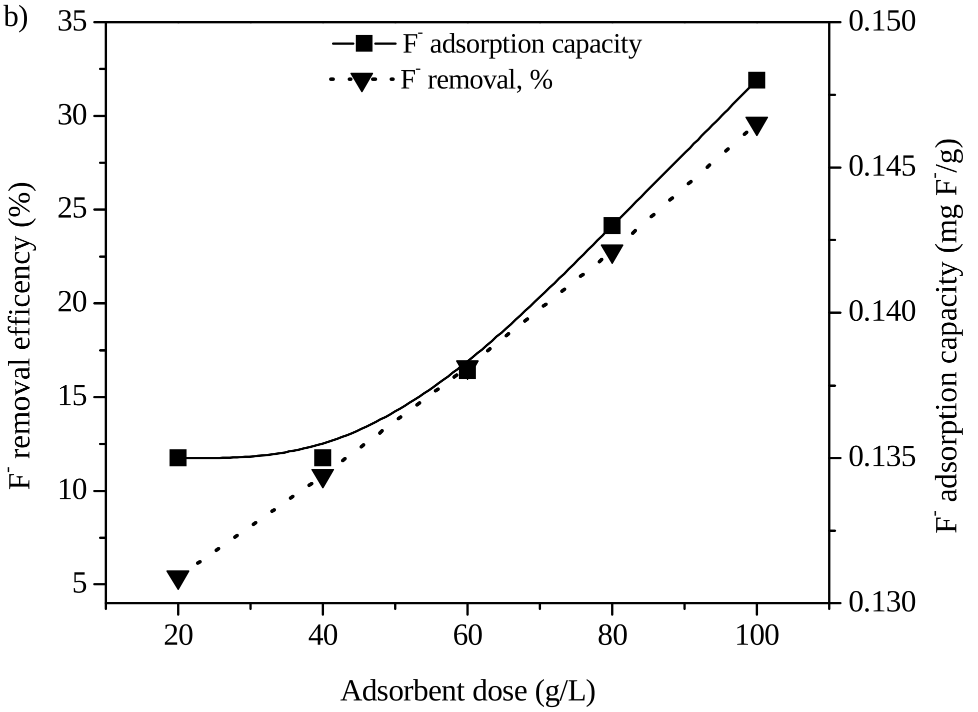

Figure 11: F⁻ removal performance of the STI from Ethiopia from a) 20 and b) 5 mg/L initial fluoride concentrations as a function of dose

3.3. Comparison of Defluoridation capacity of zeolites from Ethiopia and Mexico

3.3.1. Characterization of zeolites

The structural identification of zeolites from Ethiopia and Mexico was carried out by X-ray diffraction, Table 2. The samples are rather pure; the only compounds were quartz and montmorillonite in clinoptilolite-heulandite zeolite of Mexico and vermiculite in analcime of Ethiopian zeolite, all of which are not dangerous for health

[138]. The features of the zeolites as reported in the bibliography are again compared in Table 3. Note how different the channel dimensions and the free pore volumes are.

Table 2: Structural identification by XRD analysis of the natural zeolite from Ethiopia and Mexico

Sample	Main compound	Minor compounds
Zeocat ECO	Clinoptilolite-Heulandite	------
San Luis Potosí, Mexico	Clinoptilolite-Heulandite	Quartz, Montmorillonite
Puebla, Mexico	Clinoptilolite-Heulandite	Amorphous
Hashenge, Ethiopia	Stilbite	---
Tigray, Ethiopia	Analcime	Vermiculite, small fraction of non-crystalline material

As expected, with this characterization technique it is not possible to distinguish between clinoptilolite and heulandite [139, 140]. Only by complementing XRD studies with temperature-based analyses, such information may be obtained.

A major difference between the two zeolites is that heulandite undergoes a sluggish phase transition at about 230 ^{o}C, whereas clinoptilolite does not [139]. Clinoptilolite is more stable towards dehydration than heulandite. If heulandites are slowly heated, part of their water is lost rapidly at first and then slowly up to 200 ^{0}C, at this temperature the mineral again begins to dehydrate rapidly. Besides, heulandites and clinoptilolite have been distinguished on the basis of their cation contents and Si/A1 ratios, with clinoptilolite having (Na + K) > Ca and Si/A1 > 4, and heulandite having Ca > (Na + K) and Si/A1 < 4 [140].

Table 3: Categorization and structural properties of clinoptilolite, heulandite, stilbite, and analcime taken from the Atlas of natural zeolite framework

Natural Zeolites	Primary cell formula, crystal system structure	Channel dimension, nm	Free volume	Exchangeable cations
Heulandite	$(Na,K)Ca_4(Al_9Si_{27}O_{72})\cdot 24H_2O$ 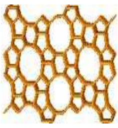 Monoclinic	0.44×0.72	0.39	Na, K, Ca, Sr, Ba
Clinoptilolite	$(Na,K)_6Ca_4(Al_6Si_{27}O_{72})\cdot 20H_2O$ 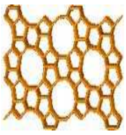 Monoclinic	0.44×0.72	0.34	Na, K, Ca, Sr, Ba
Stilbite	$NaCa_4(Al_9Si_{27}O_{72})\cdot 30H_2O$  Monoclinic	0.54×0.69	0.341	Na. K, Ca, Mg
Analcime	$Na_{16}(Al_{16}Si_{32}O_{96}).16H_2O$ 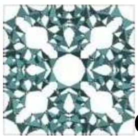 Cubic	0.16×0.42	0.18	Na, K, Ca, Rb, Cs

In Figure 12, the TGA curves obtained in air atmosphere are shown. The TGA curves show that the zeolites from San Luis Potosí (Mexico) and Zeocat ECO have higher thermal stability towards dehydration than the zeolite collected in Puebla (Mexico). Therefore, the zeolites San Luis Potosí and Zeocat ECO are clinoptilolite, but the Puebla zeolite is heulandite, bearing in mind that Si/Al ratio is higher in clinoptilolite.

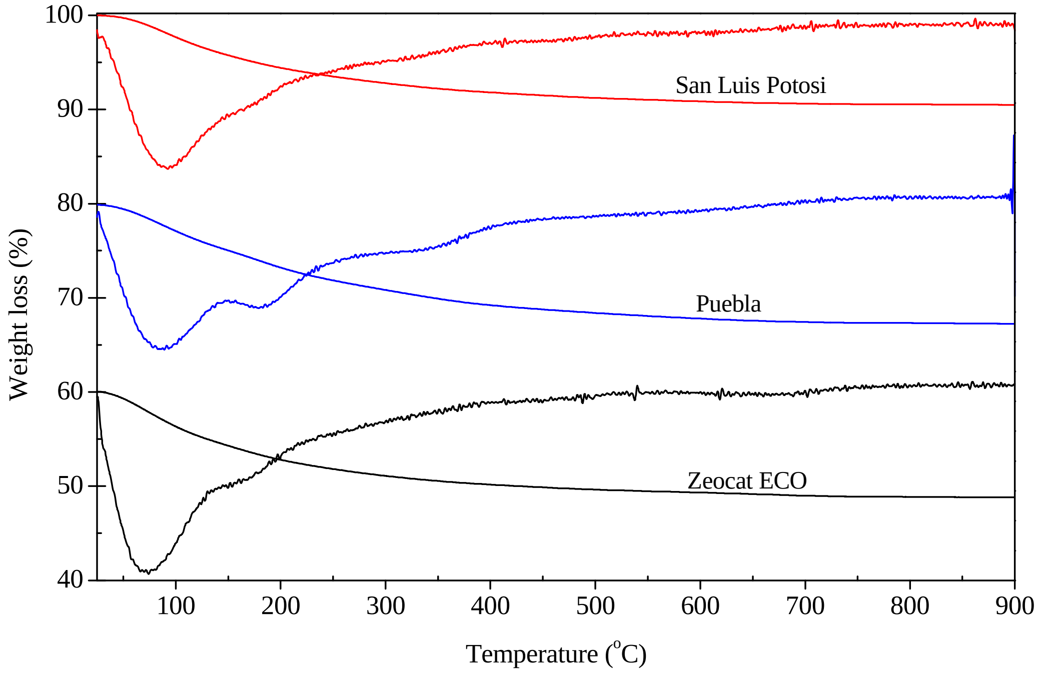

Figure 12: Thermogravimetric analyses of Mexican natural zeolites

3.3.2. Defluoridation test results

Three natural zeolites from Mexico were tested for fluoride removal and the results are compared with the performance of two zeolites from Ethiopia as described in Table 4 for two different initial fluoride concentrations of a) 20 mg/L, and b) 5 mg/L. In both cases, the fluoride retention percentage increases with the increasing adsorbent dose. If the initial fluoride concentration is 5 mg/L, the performance of the clinoptilolite samples (San Luis Potosí and Zeocat ECO) reaches 10 % and around 20 % of fluoride retention for low (20 g/L) and high (100 g/L) adsorbent doses, respectively. These values are ca. 5 % higher than the values obtained for stilbite but about four times lower than the fluoride retention of analcime.

Table 4: Fluoride removal efficiency as a function of adsorbent dose from initial fluoride concentrations of a) 20 mg/L and b) 5 mg/L, respectively

a) dose (g/L)	Fluoride removal (%)				
	Zeocat ECO	San Luis Potosi	Puebla	Analcime	Stilbite
20	0.4	2.0	2.8	23.5	3.3
60	3.8	5. 6	12.4	56.3	12.1
100	5.6	16.2	19. 6	76.5	21.9

b) dose (g/L)	Fluoride removal (%)			
	Zeocat ECO	San Luis Potosi	Analcime	Stilbite
20	10.2	10.4	32	5.4
60	16.5	14. 6	76	16.6
100	22.1	20.4	84	29.6

If the initial fluoride concentration is 20 mg/L, the performance of the clinoptilolite sample from San Luis Potosí only reaches 16 % of fluoride retention for high (100 g/L) adsorbent doses. Instead, the analcime from Ethiopia retains more than 76.5 %, i.e. more than 5 times.

Although zeolites differ in their structure, their Si/Al ratio, and their exchangeable cations among other parameters, some clear trends can be established. In all cases the best zeolite to retain fluoride, among the five studied in this work is analcime. This zeolite presents the smallest channel dimensions and the lowest free pore volume. Therefore, at this level, any mechanism based on diffusion has to be rejected. Indeed, fluoride is a very small ion (ionic radius of 0.136 nm) and it is expected to move easily into clinoptilolite, heulandite, or stilbite networks; in analcime it cannot enter.

The rather good retention of analcime may be attributed to extraframework aluminum compounds (alumina or aluminum hydroxide) and/or to connectivity defects. Such hypothesis is in agreement with NMR results, which showed the presence of octahedral aluminum atoms [26]. On the other hand, if the clinoptilolite samples do not retain as much fluoride, it must be due to the absence of octahedral aluminum atoms. However, they do retain some fluoride, and furthermore, the amount is higher than in stilbite or heulandite. Clinoptilolite is known to have a Si/Al ratio higher than 4, whereas heulandite possess Si/Al ratio lower than 4 [108]. Then, as clinoptilolite has less aluminum atoms, it is less negatively charged and should offer less resistance to fluoride acceptance. But, clinoptilolite exchangeable cations are Na^+ and K^+, which exceed those of Ca^{2+}; instead heulandite has also Na^+ as well as K^+ cations which are less than those of Ca^{2+}. Highly charged cations as Ca^{2+} are efficient sites for fluoride retention. Therefore, the difference between the performances of those zeolites cannot be assigned to their slight structural differences but to the amount of amorphous compound present in the heulandite from Puebla, which most probably partially blocks the pore entrances.

However, the above discussion is not valid for stilbite whose Si/Al ratio is 2.7 and whose free pore volume is the same as the free pore volume of clinoptilolite. To explain the differences in fluoride retention we have mentioned first the presence of extra framework aluminum, then the importance of Si/Al ratio; but, we have not taken into account the type of exchangeable cation present into the zeolite network. Zeolites are cation exchangers and are not prone to retain anions. Still the charge balance into the zeolite network may be reversed or at least altered introducing, into the cavities and channels, highly charged cations. For instance, silver exchanged zeolites have been reported to retain efficiently iodine anions. Silver zeolite cartridges are typically used in nuclear power plants to adsorb gaseous iodine [141]. The introduction of sulfur into zeolite networks modifies remarkably the charge equilibrium into the zeolite lattice [142]. It is not surprising, then, that if the compensation cations of stilbite are fully exchanged to calcium the performance of the sample in fluoride retention is increased, not only because connectivity defects are generated during the exchange treatments [82], but, because the calcium ions are divalent and highly charged. If stilbite contains compensation cations, which only balance the charge network and do not create zones highly charged, fluoride is not retained.

Therefore, in this work, two mechanisms of fluoride retention in zeolites are proposed. On the one hand, fluoride retention may be attributed to a high number of connectivity defects and to a high amount of extra framework aluminum compounds present in some zeolites, as already proposed by L. Gómez-Hortigüela et al. in a previous work [26]. This mechanism is independent of the type of zeolite structure. In this scenario, fluoride substitutes OH^- ions and it is strongly retained.

On the other hand, fluoride retention may be attributed to a typical adsorption force generated around some highly charged cations, for instance calcium. Of course, the amount of exchangeable cations, proportional to the Si/Al ratio, is crucial. This adsorption bond is weak and fluoride is expected to leach easily. These two propositions are not exclusive, most probably in some zeolites containing calcium, or any other divalent cation, on a first step some fluoride is adsorbed in the vicinity of the calcium atoms and, then, the remaining fluoride, in a second step, or simultaneously, is exchanged with the OH^- group of the extra framework material. Both mechanisms may be schematized in Figure 13 as shown below.

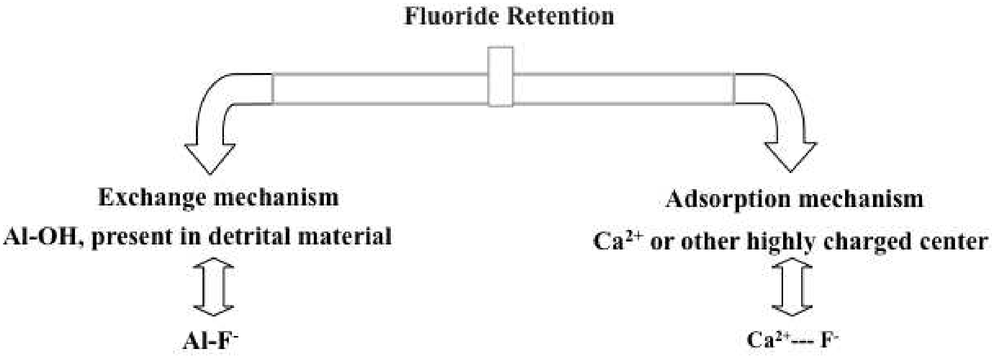

Figure 13: Suggested mechanisms for fluoride retention in natural zeolites

Even if zeolites represent a class of materials that have all the required properties to be used as adsorbents [26], the experimental outcome of this study indicated that they are not good adsorbent materials for fluoride removal. This is because they have negative surface charges almost at all pH values, and thus have low adsorption capacity for anions.

Nonetheless, the surface of zeolites can be modified through suitable chemical treatments. In recent years, for example researchers have tried in growing the HAp crystals on the surface of zeolites [98, 103, 143]. In 2004, Y. Watanabe et al. reported HAp crystallization on the surface of a synthetic zeolite, zeolite A [143]. They prepared a novel type-A zeolite with hydroxyapatite layers on its surface using a hydrothermal method based on the cation exchange of Ca^{2+} in zeolite for NH_4^+ in solution. Their aim was to achieve a total coverage of the zeolite surface with HAp crystals in order to trap radioactive ions or other contaminants within the zeolite void volume, preventing their release. The reported method yields large HAp crystals on the zeolite surface. However, a recent study in 2014 was proposed an interesting option based on natural stilbite zeolite from Ethiopia [98]. This our precedent work reported the development of high performing nanohydroxyapatite on stilbite surface, similarly based on the cation exchange of Ca^{2+} in zeolite for NH_4^+ ions in solution. In this case, however with the aim of fluoride removal from drinking water. In the present work as well, we are studying stilbite modification based on the growth of nanohydroxylapatite on its surface, nanohydroxyapatite/stilbite (nHAST) composite with the aim of fluoride removal from drinking water. In this, stilbite plays a dual role: as a support material to hold the smaller HAp nanoparticles not free, and as a source of calcium, one of the reagent materials for the synthesis of HAp materials. Besides, the current study is dealt with the optimization of the synthesis conditions of the nHAST composite.

Chapter Four

4. Results and Discussion on nHAST composite

Initially, nHAST composite was synthesized according to procedure described in the Section 3.1.2 [98]. The nHAST composite then characterized thoroughly in order to understand material properties: chemical composition, morphology and structure. Afterwards, the performance in fluoride removal has been tested in batch mode.

4.1. X-ray diffraction analysis results

Qualitative X-ray diffraction analysis was used to determine whether the support precursor STI framework went through any transformation during the preparation process. The XRD pattern (Figure 14) of the as synthesized nHAST composite sample and the parent STI zeolite are very similar.

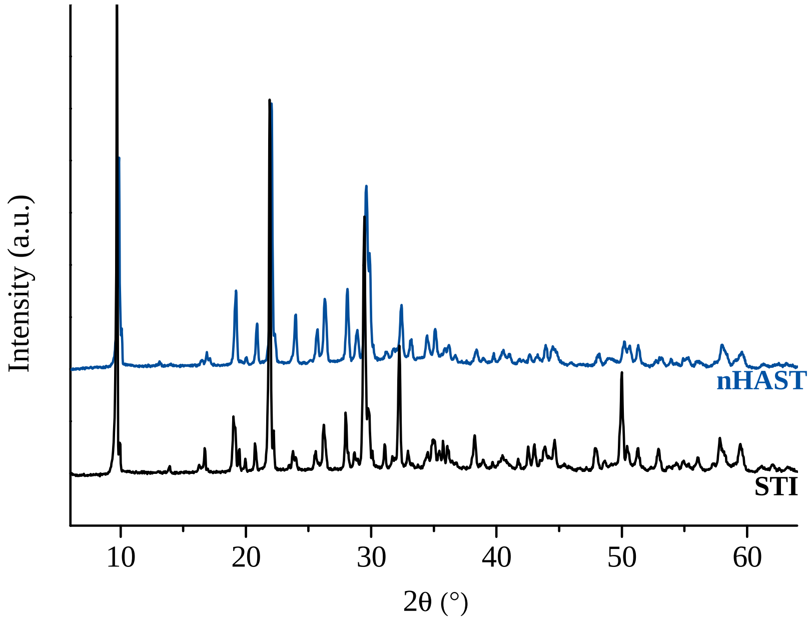

Figure 14: XRD profiles of the support STI and nHAST composite samples

The peaks at 2θ angles of 9.70, 19, 22, 26, 28, 29.5, 32 and 50 degrees displayed characteristic peaks identical to those of stilbite [99], evidencing the resistance of the STI framework. The identification of the bands was difficult in the case of the nHAST composite, possibly because of the low concentration of HAp in the composite, or its smaller crystal size as well as the possibility of overlapping with the zeolite diffractions. However, after the growth of HAp on STI surface these peaks slightly decrease in intensity.

4.2. IR-ATR analysis result

Further structural studies on nHAST composite sample by IR-ATR also provided an important clue in the formation of HAp structure on STI surface. Figure 15 shows IR-ATR spectra of (a) as synthesized nHAST composite and (b) the original support precursor STI zeolite. In the original STI zeolite (Figure 15b), the absorption bands appear at 1145 and 994 cm^{-1} are due to the external and internal T-O asymmetric stretching vibrations, while bands at 790 and 701 cm^{-1} are attributed to the symmetric stretching vibrations The band at 560 cm^{-1} arises from double ring vibrations, and that at 430 cm^{-1} comes from T-O bending [144]. Finally, a broad low intense band observed at about 1650 cm^{-1} indicates adsorbed water molecules within the STI framework.

After the chemical treatment of STI to produce the nHAST composite (Figure 15a), the main bands due to the STI framework remained. However a new band arose at about 1430 cm^{-1} due to the presence of NH_4^+ ions after the ion-exchange process during the HAp crystallization. This indicates that the chemical treatment caused the cation exchange of Ca^{2+} by NH_4^+, agreed well with the ICP result, refer to Table 5.

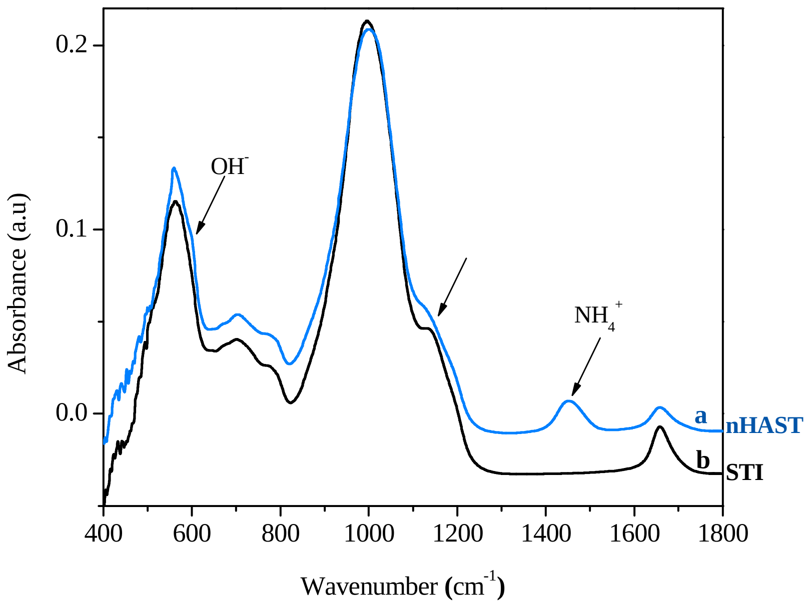

Figure 15: IR-ATR spectra of a) nHAST composite and b) STI zeolite

After the chemical treatment, only few characteristic absorption bands of very weak intensities that confirm the growth of HAp on the STI surface was identified with a careful observation due to vibration of OH$^-$ group (602 cm^{-1}) [143]. At around 1125 cm^{-1} (indicated in black arrow) the new feature seems shoulder start originating in nHAST composite sample, probably due to the growth of HAp film on the surface of STI zeolite.

4.3. ICP elemental analysis results

Quantitatively the formation of HAp on the STI surface can be easily assured by the presence of P in the final nHAST composite, by ICP elemental analysis (Table 5). The content of HAp ($Ca_5(PO_4)_3OH$) in the composite in weight % (% HAp) is calculated from the content in P obtained from the weight % of P (by ICP), according to eq. 11 in section 2.3.

Table 5: ICP elemental analysis of STI and nHAST composite samples

Samples	**Al** %wt	**Si** %wt	**Ca** %wt	**K** %wt	**Na** %wt	**P** %wt	**HAp** %
STI	8.0	20.4	4.9	0.3	0.5	0.0	---
nHAST	7.8	20.3	4.8	0.3	0.1	0.8	4.3

As shown in Table 5, the natural STI zeolite used as a support material has a remarkably high content of Ca^{2+}, which supplies for the HAp formation in its reaction with $(NH_4)_2HPO_4$. As determined by ICP elemental analysis the presence of 0.8 % of P is confirmed, suggesting the growth of the amount equal to 4.3 % HAp, as calculated using eq. 11stated in section 2.3, on the STI surface, which is in the final nHAST composite material.

4.4. Defluoridation test results

Adsorption experiments were initially performed for nHAST composite as well as the support STI zeolite at different doses, 10 and 100 g/L, respectively using a constant initial fluoride concentration of 5 and 10 mg/L and a contact time of 20 hours with continuous agitation at room temperature. The preliminary defluoridation test result shows higher performance of nHAST composite, about 46.9 % fluoride removal as compared with the original STI zeolite with very low removal efficiency of 24.7 % at 100 g/L high dose (Table 6). Interestingly, if the initial fluoride concentration lowers to 5 mg/L while keeping other conditions constant, the removal efficiency reach about 63.6 % and 29.6 %, for nHAST and STI adsorbents, respectively. Thus, the chemical treatment process brings about a significant improvement in fluoride removal conditions [28, 98]. The observed increase in fluoride removal efficiency at lower initial concentration, 5 mg/L is due to the availability of new adsorption sites of HAp on the STI surface, possibly more active smaller crystal of HAp was formed

Table 6: Fluoride removal efficiency of the support STI and nHAST composite

[F]$_0$, mg/L	Fluoride removal efficiency, %	
	at 100 g/L dose	at 10 g/L dose
	STI	nHAST
5	29.6	63.6
10	24.7	46.9

Because the WHO maximum permissible limit was not met, even from such a lower fluoride concentration of 5 mg/L, further enhancement in fluoride removal performane of nHAST adsorbent has been carefully assessed. This is done through optimization of synthesis procedural parameters as described in the following section.

4.5. Optimization of synthesis procedure for nHAST composite

4.5.1. Synthesis time optimization

Optimization of synthesis time was started with the synthesis of two nHAST composite samples per each synthesis time of 0, ½, 1, 2, 4, 24, and 48 hours. All the synthesized composite samples were fully characterized using the available characterization means such as X-ray diffraction, IR-ATR, and ICP-OES elemental analyses techniques. Finally, their fluoride removal capacity was tested in batch adsorption experiments on a demanding situation, using initial fluoride concentrations of 5 and 10 mg/L.

4.5.1.1. X-ray diffraction analysis results

As shown in Figure 16, the XRD profiles of the composite samples prepared at different synthesis time are very similar with one another as well as with the support STI zeolite. There is no new crystalline peaks that confirm the formation of HAp on the surface of STI, probably due to the lower concentration of HAp in the nHAST composite or its small crystal size, and the overlapping with the zeolite diffractions. However, with careful observation in nHAST composite samples, it was clearly identified from the figure that the intensity of the XRD peaks was slowly decreasing with time. This is more noticeable in nHAST composite samples at the longer synthesis time (nHAST at 24 and 48 hours) probably due to the formation of higher amount of hydroxyapatite as a function of time on zeolite surface.

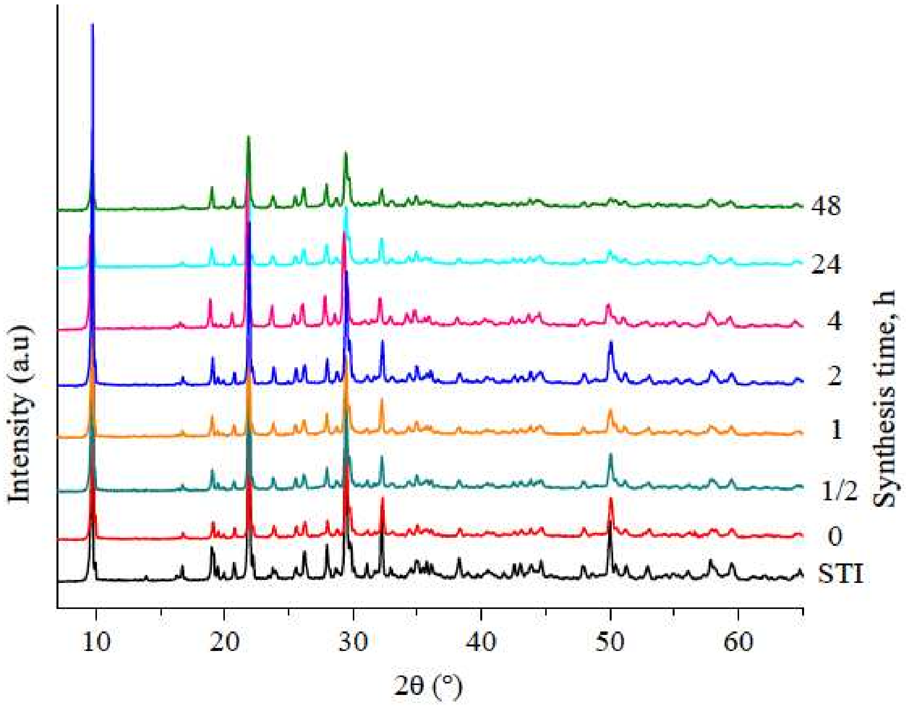

Figure 16: XRD profiles of the support STI zeolite and the nHAST composites synthesized as a function of synthesis time

4.5.1.2. IR-ATR analysis results

Figure 17 shows IR-ATR spectra of the STI and nHAST composite samples prepared at different synthesis time. The two strong bands at about 1040 and 565 cm^{-1} attributed to stilbite structure as described above. However, closer to these, the expected bands due to hydroxyapatite are unable to be seen, probably overlapped by the stronger and more abundant zeolite band. It is interesting to note that the band intensity decreased with time, as clearly identified at the longer synthesis time of 24 and 48hours, possibly due to the particle size effect. Because the hydroxyapatite particles crystallized on stilbite surface most likely growing larger in size with time in the expense of the zeolite band, with which in the beginning posses similar intensities.

The new band at about 1430 cm^{-1} is due to the presence of ammonium ion, NH_4^+. The other new band at about 1650 cm^{-1} is attributed to the attached water molecules within the framework of stilbite. As the latter band due to water is a structural sensitive, adsorption and desorption of water may be easily monitored based on the change occurred at it. In our case, as depicted from Figure 17, it is clearly decreasing with time, showing the release of more and more water as a function of time. This in turn might indicate the release of more extra fame work Ca^{2+} ions that initially surrounded by the water molecules. More release of Ca^{2+} ions means that more and more hydroxyapatite particles are formed on the surface of zeolite. This complements well with the XRD investigation described earlier.

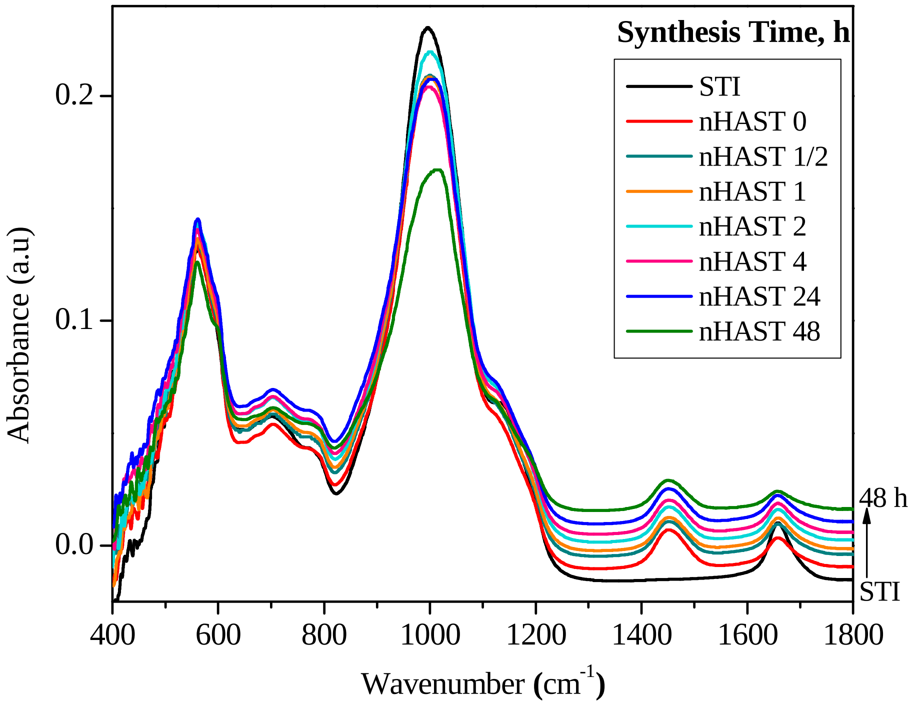

Figure 17: IR-ATR spectrum of the support STI zeolite and nHAST composites at various synthesis times

In general, although a slight change was identified in diffraction intensities in XRD pattern and in IR-ATR absorption bands, after and before modification there is no clear presence of the characteristic crystalline peaks or bands that clearly confirm the formation of hydroxylapatite on stilbite surface.

4.5.1.3. ICP elemental analysis result

As shown in Table 7 ICP elemental analysis result, the formation of hydroxylapatite on stilbite surface can easily be assured by the presence of P in the final synthesized nHAST composite materials.

Table 7: ICP elemental analysis results on STI zeolite and nHAST composites

Samples	Al (% wt)	Si (% wt)	Ca (% wt)	K (% wt)	Na (% wt)	P (% wt)	HAp %
STI	8.0	20.4	4.9	0.3	0.50	0.0	----
nHAST 0	7.8	20.4	4.8	0.3	0.1	0.8	4.3
nHAST1/2	7.8	20.7	4.8	0.3	0.1	0.8	4.3
nHAST 1	7.9	20.6	4.8	0.3	0.1	0.8	4.3
nHAST 2	7.8	20.2	4.9	0.3	0.2	0.8	4.3
nHAST 4	8.0	20.2	4.9	0.3	0.2	0.9	4.9
nHAST 24	7.7	20.2	5.1	0.3	0.2	1.0	5.4
nHAST 48	7.8	19.8	5.6	0.3	0.2	1.3	7.0

The study result of ICP elemental analysis indicates the release of more Ca^{2+} ions as function of synthesis time. This is clearly manifested in the longer time of 24 and 48 hours, suggesting the crystallization of more hydroxyapatite crystals with time. Similarly, the amount of P in the final synthesized nHAST materials increasing slowly with time, probably due to the presence of enough contact among the reacting species at a longer synthesis time; therefore the quantity of HAp crystallized as calculated from eq. 11 stated in section 3.3 based on the P content produced in the final nHAST composite materials by ICP also increasing proportionately as clearly identified at nHAST composites with longer synthesis time, Table7.

4.5.1.4. Defluoridation test results

Batch adsorption mode was used to test the fluoride removal capacity of nHAST samples synthesized at different synthesis time. The findings of the study as presented in Figure 18 clearly show the relationship that may be found between the amount of HAp crystallized (in nHAST composite samples) as a function of synthesis time and the associated defluoridation capacity. Interestingly, in nHAST samples with the shorter synthesis time the defluoridation capacity starts increasing, and reached at maxima just at nHAST sample synthesized at 2 hours synthesis time. Soon after this the capacity declining sharply, refer to the nHAST sample synthesized at 4 hours synthesis time. Then slowly until it attained the lowest minimum point in nHAST sample synthesized at 48 hours synthesis time, regardless of the fact that more amount of HAp was crystallized as a function of synthesis time (see Table 7).

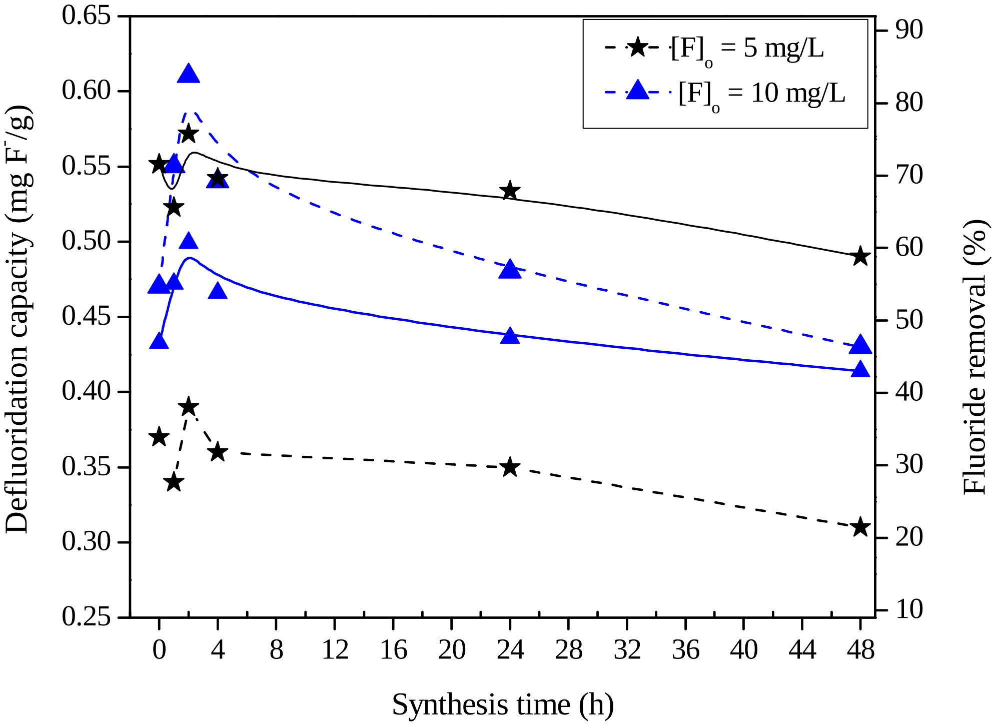

Figure 18: F^- removal capacity (dashed lines) and removal efficiency (solid lines) of nHAST composite samples as a function of synthesis time

Such unexpected behaviour may be due to the formation of larger crystal size of HAp on the stilbite surface at a longer synthesis time. At the same initial fluoride concentration of 10 mg/L, the corresponding fluoride removal efficiency at maxima (nHAST at 2 hours synthesis time) was significantly higher, about 60.9 %, than nHAST at 0 hour (un-optimized composite sample) with fluoride removal efficiency of only about 46.9 %. Interestingly, from a lower initial fluoride concentration, 5 mg/L the efficiency increases noticeably, and reaches about 79.2 % in nHAST at 2 hours synthesis time. Therefore, 2 hours time is considered as the optimum synthesis time for further preparation of nHAST composite.

4.5.2. Crystallization pH optimization

Under this section, the effect of crystallization pH on morphology or crystal size of HAp crystals in nHAST composite was investigated at pH of 7, 7.5, 8, 8.5, 9, 9.5 and 10. The pH was adjusted at a given value using0.1M NaOH/HCl solutions. Two composite samples were synthesized per each crystallisation pH at the optimized synthesis time of 2 hours, while keeping other experimental conditions constant. The resulting nHAST composite samples were characterized similarlyby XRD, IR-ATR, and ICP-OES techniques. Finally, their performance in fluoride removal was analyzed in batch adsorption experiments in order to differentiate the best performing one.

4.5.2.1. X-ray diffraction analysis results

Figure 19 demonstrates the X-ray diffraction profiles of the support STI zeolite and nHAST composite samples synthesized as a function of crystallization pH as shown below. As clearly observed from the figure, all the nHAST composites synthesized from different crystallization pH media as well as the parent support STI have very similar XRD patterns. All the samples: nHAST pH 7/7.5 treated with 0.1M HCl acidic solution and those nHAST pH 8.5-10 treated with 0.1M NaOH basic solution including the untreated nHAST pH 8 resisted the chemical treatments. Interestingly, the diffraction intensities as a function of the crystallization pH remain unchanged, unlike in the synthesis time optimization case. However, X-ray diffraction analysis provides very little or no information concerning the effect of crystallization pH on the formation or nature of HAp crystals on STI surface.

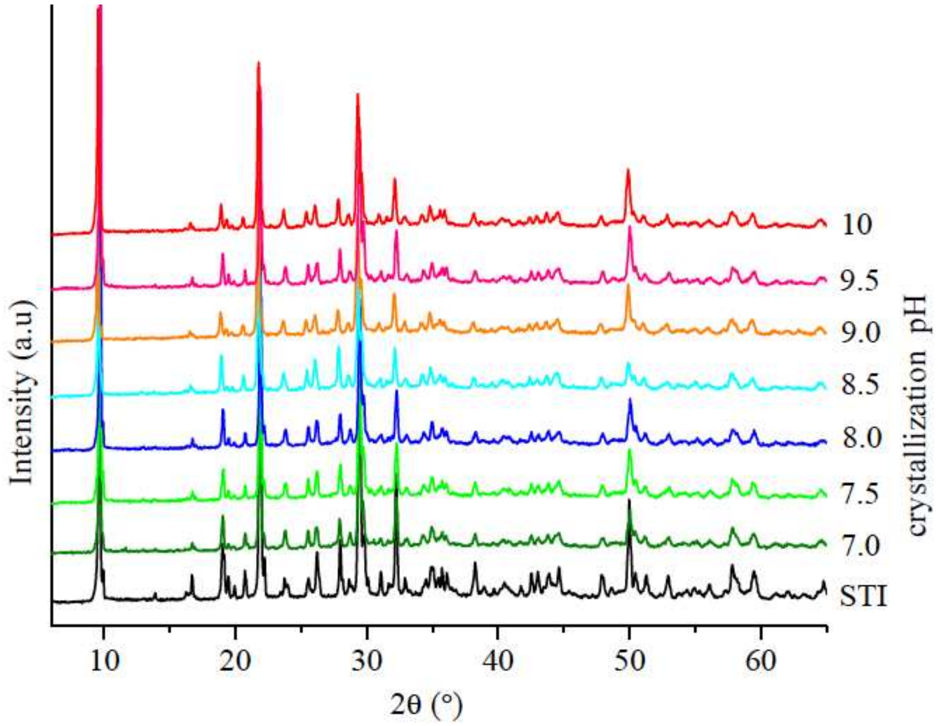

Figure 19: XRD profiles of the support STI zeolite and nHAST composite samples as a function of crystallization pH

4.5.2.2. IR-ATR analysis results

Figure 20 describes the IR-ATR spectra of the support STI zeolite and nHAST composite samples. In the original support STI the absorption bands at 1145 and 994 cm^{-1} was attributed to T-O asymmetric stretching vibrations, whereas those bands at about 790 and 701 cm^{-1} were assigned to symmetric stretching vibrations of the framework aluminosilicate in the STI structure. The band at 560 cm^{-1} arise from double ring vibrations, and very weak band at about 430 cm^{-1} comes from T-O bending in the STI structure [144, 145].

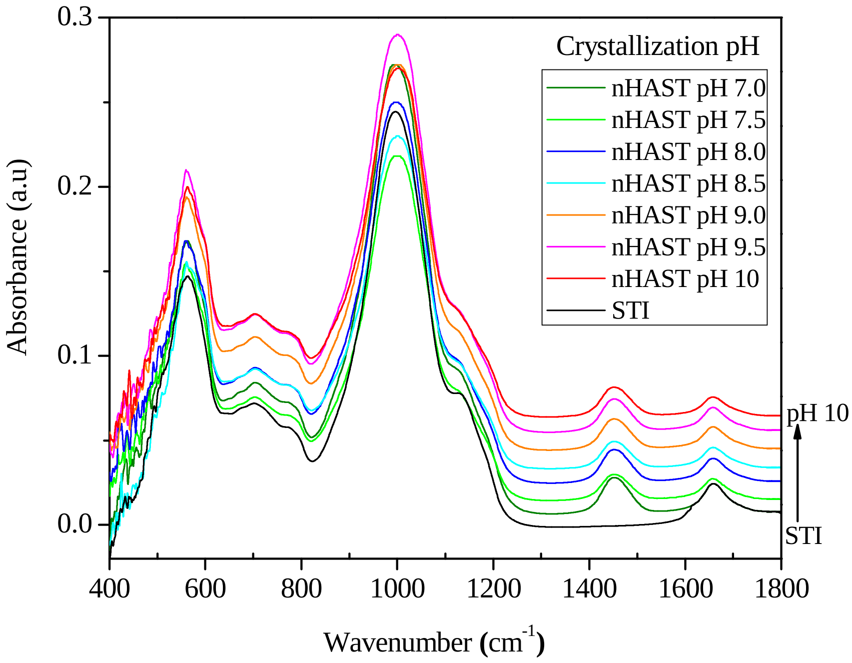

Figure 20: IR-ATR spectra of a support raw precursor, STI and nHAST composite samples as a function of crystallization pH

The new originating broad band at around 1430 cm^{-1} was due to the presence of ammonium ion, $NH_4^+$and the last band at about 1650 cm^{-1} was attributed to the structural water molecules within the STI framework. As identified in the figure with closer look, both of these bands remain almost constant irrespective of crystallization pHs, indicating the independence of cation exchange process (Ca^{2+} by NH_4^+) on crystallization pH. This perhaps suggests the possibility of equilibrium establishment without the addition of NH_3/NaOH, or HCl solutions for pH adjustment.

Interestingly, with a closer observation at the band around 1100 cm^{-1}, the growth of shoulder that seems increasing with crystallization pH was identified. As shown in the figure, this is clearly visible at higher pH values of pH 9.5 and 10, probably indicating the growth of more and more HAp particles on STI surface as a function of crystallization pH.

4.5.2.3. Thermogravimetric analysis results

Thermogravimetric analysis was carried out on the selected nHAST samples: nHAST pH 7 and nHAST pH 7.5 (treated with 0.1 M HCl acidic solution), nHAST pH 8 (without chemical treatment), and nHAST pH 9 and nHAST pH10 (treated with 0.1 M NaOH basic solution). The TGA analysis results presented in Figure 21 show TGA-DTG curves of the nHAST composite samples and support STI zeolite. It is clearly seen from the figure that in low temperature region alone, two differentiated weight losses can be observed in both the support STI and nHAST composite samples. In both STI and nHAST composite samples, the first weak desorption peak at temperature below 130 ºC, corresponding to loosely bound water molecules. In STI zeolite, the second strong weight loss with maximum desorption rate at around 175 ºC and other of a lower desorption rate at about 250 ºC are corresponding to strongly adsorbed water molecules within the STI structure by coordination with exchangeable extra framework cations such as Ca^{2+} and Na^{+} ions.

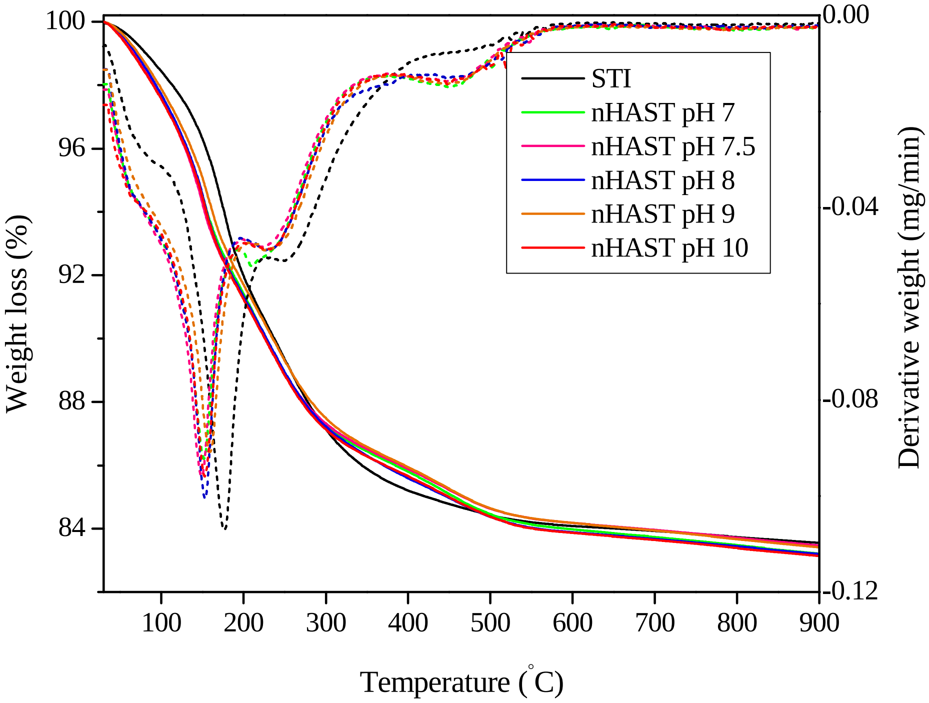

Figure 21: TGA (solid lines) and DTG (dotted lines) of the nHAST composites synthesized at various crystallization pH, and the support STI zeolite

However, in nHAST composite samples there is a slight shift of weight loss for dehydration at lower temperatures. In this case, a second weight loss of strongly adsorbed water molecules inside the zeolite structure takes place at around 240 ºC. Desorption of poorly-retained water at temperatures below 130 ºC is much more intense for the STI and nHAST composite samples. Interestingly, desorption of strongly-retained coordinated water molecules at higher temperatures is much smaller in the case of nHAST due to the exchange of divalent Ca^{2+} by monovalent NH_4^+ ions, which weakly coordinate water molecules, and hence the major water desorption occurs at low temperature. Interestingly, in nHAST composite samples, an additional new broad desorption band showed up at around 450 ºC due to deammoniation, the release of NH_3 as NH_4-STI transforms into H-STI [82, 144, 146, 147]. The constant nature of this band indicates the existence of balanced exchange between Ca^{2+} and

NH_4^+ ions. This in turn suggests the release of constant amount of Ca^{2+} ions and thus the independence of ion-exchange process on crystallization pH.

4.5.2.4. ICP elemental analysis results

Finally, the chemical compositions of the nHAST samples were determined by ICP as presented in Table 8. The ICP analysis result also confirmed the constant release of Ca^{2+} ions, regardless of the crystallization pH. As quantified by the content of P by ICP, the % HAp in the final nHAST composites synthesized from different crystallization pH was look alike. This finding agrees well with both the IR-ATR and TGA analyses results. Thus, the growth of the shoulder in IR-ATR spectrum result is not due to the amount of HAp produced, possibly the result of the particle size effect.

Table 8: ICP elemental analysis result of the support STI and nHAST composites synthesized as a function of crystallization pH

Samples	**Al** (% wt)	**Si** (% wt)	**Ca** (% wt)	**Na** (% wt)	**P** (% wt)	**HAp** %
STI	8.0	20.4	4.9	0.50	0.0	—
nHAST 7.0	7.7	22.2	4.7	0.3	0.9	4.9
nHAST 7.5	7.7	22.6	4.8	0.3	0.8	4.3
nHAST 8.0	7.3	20.9	4.7	0.2	0.9	4.9
nHAST 8.5	7.5	20.4	4.7	0.2	0.8	4.3
nHAST 9.0	7.5	20.2	4.7	0.2	0.9	4.9
nHAST 9.5	7.7	20.5	4.7	0.3	0.9	4.9
nHAST 10.0	7.7	20.2	4.8	0.3	0.9	4.9

4.5.2.5. Scanning electron microscopy

The SEM micrographs in Figure 22 show crystals of different sizes and shapes for nHAST composite and STI. With careful observation at the micrographs, the small particles of HAp grown on support large STI crystals (at micron size) with smooth surface can be seen in irregular manner. The SEM image of nHAST pH 8 sample in Figure 22, composite sample synthesized at crystallization pH 8 without the addition of chemical for pH adjustment, shows an aggregate of more amount of smaller HAp particles grown on STI large smooth crystals, unlike in nHAST composites treated either with acidic (nHAST pH 7) or basic (nHAST pH 9/10) chemicals.

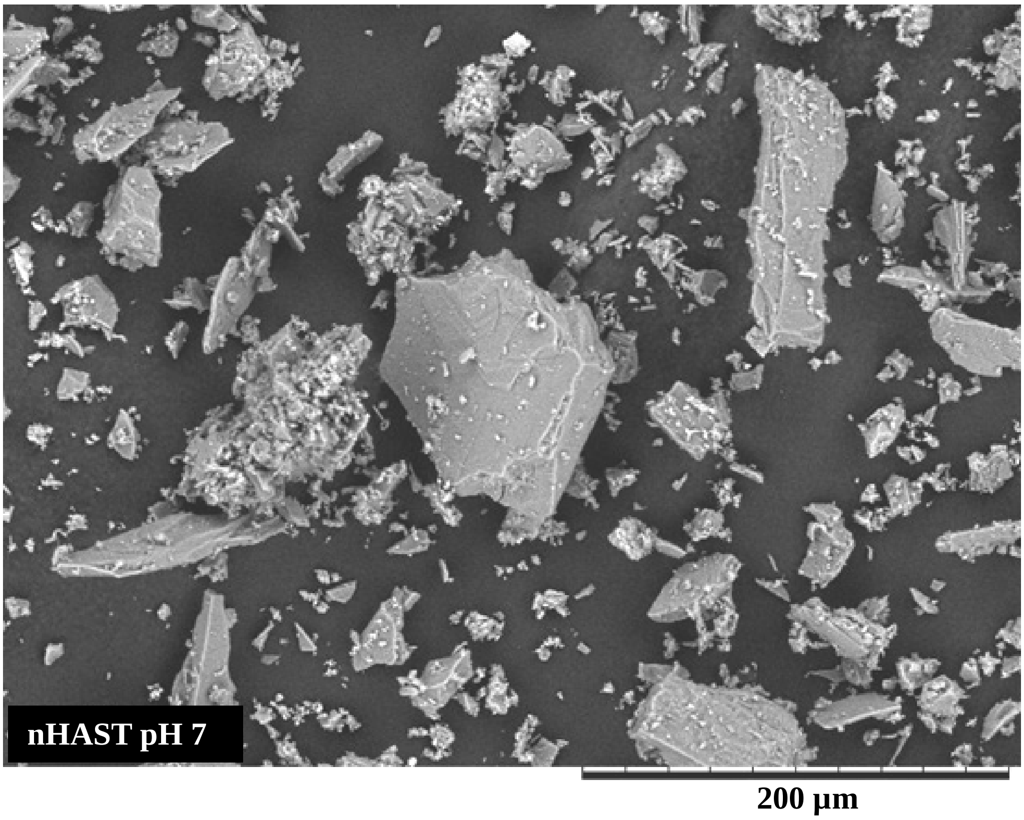
nHAST pH 7
200 µm

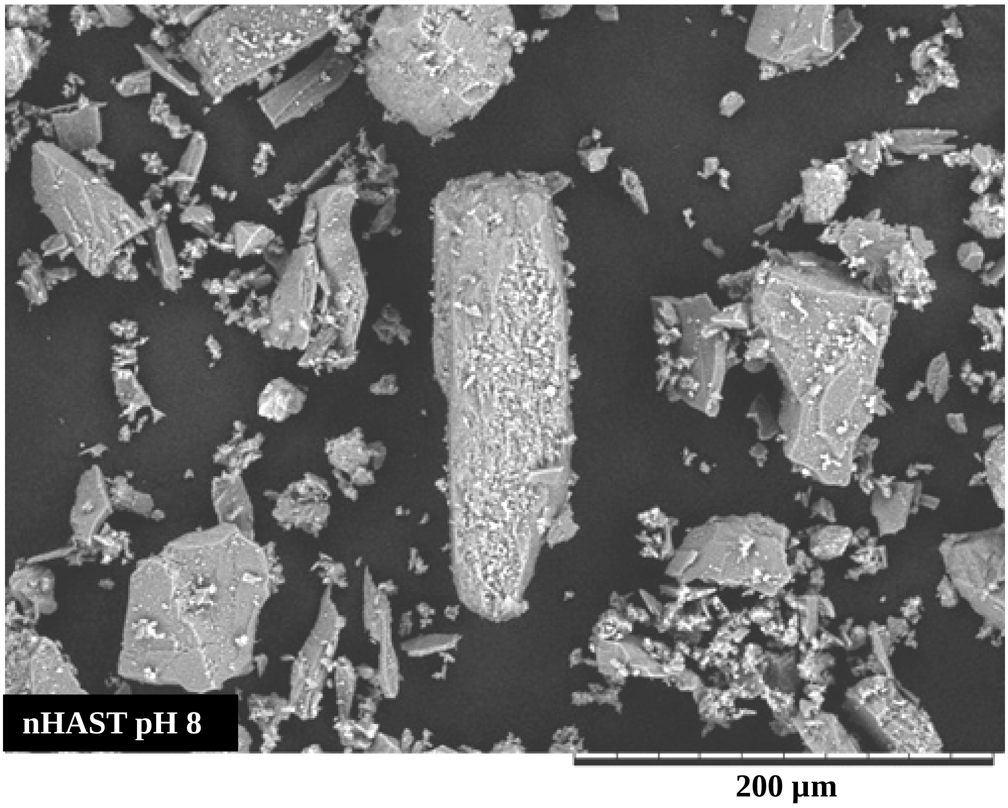
nHAST pH 8
200 µm

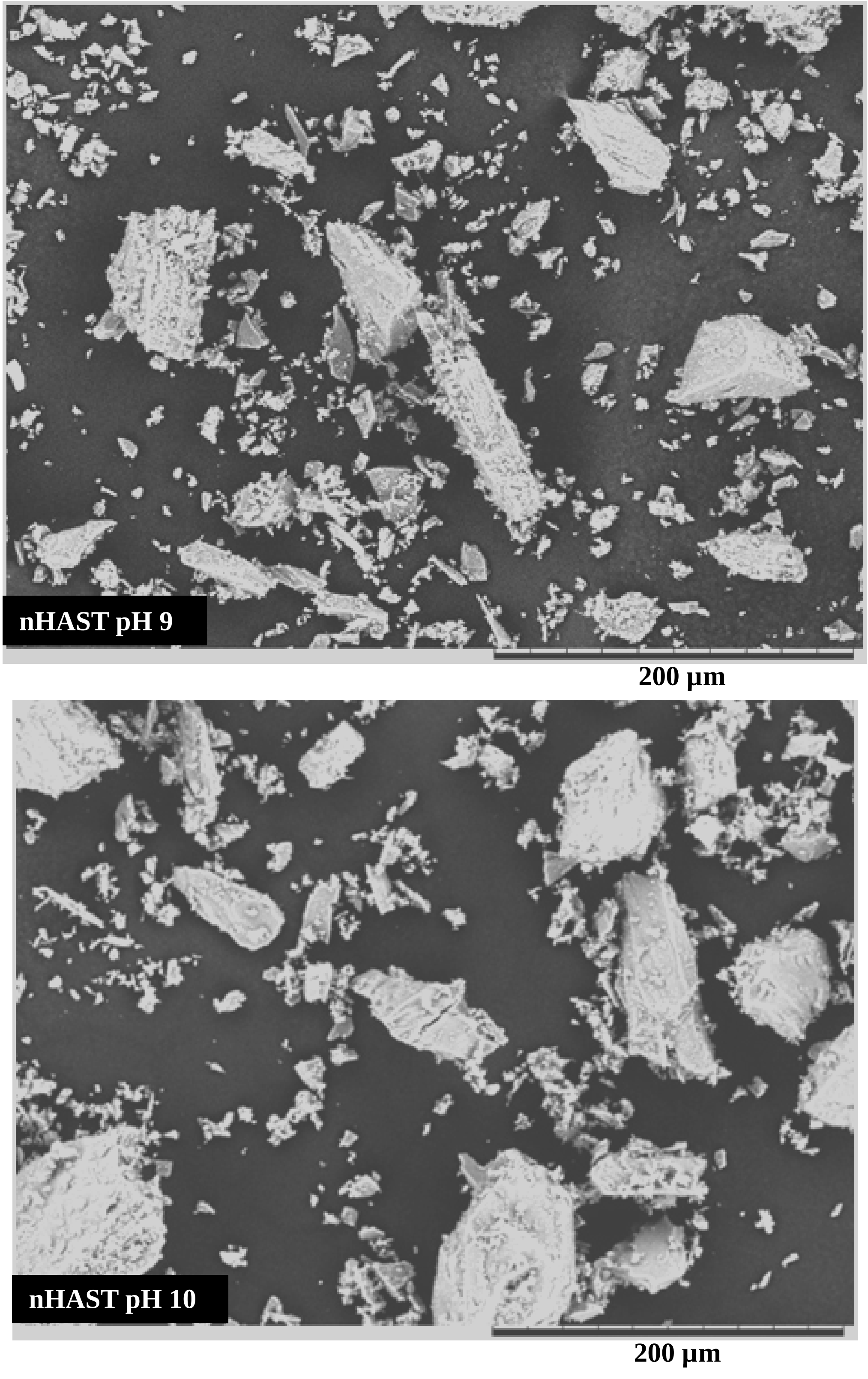

Figure 22: SEM micrographs of nHAST composite samples synthesized at various pH of crystallization

Still, based on SEM images, it was difficult to generalize the clear relationship that may exist between the HAp crystal size in different nHAST composite samples and the corresponding crystallization pH. However, it can be clearly seen from the SEM micrographs that the surface morphology of STI on which the nHAST composites have been synthesized was stable under synthesis conditions, in which both acidic and basic chemical treatments have involved during the crystallization processes while synthesizing nHAST samples at crystallization pH 7/7.5, and at crystallization pH 9/10, respectively.

4.5.2.6. Dfluoridation test results

Batch mode fluoride removal adsorption experiments were used to analyze the efficiency of various nHAST composite samples synthesized at different crystallization pH values of 7, 7.5, 8, 8.5, 9, 9.5 and 10. The experiments were conducted from initial fluoride concentrations of a) 5and b) 10 mg/L, using 10 g/L adsorbent dosage for a contact time of 20 hours agitating continuously at room temperature. The study finding results were presented in Figure 23 as shown bellow.

As clearly observed in Figure 23, the defluoridation capacity of nHAST pH 7.5, nHAST sample synthesized at crystallization pH value of 7.5 is low. However, the scenario was different in another acid treated nHAST pH 7 sample. This shows better fluoride removal performance, possibly acid treatment may generates more adsorption defect sites or brings about smaller size HAp crystals. Worth nothing to mention that nHAST pH 7 (adjusting of crystallization pH at value of 7) consumes more acid than nHAST with crystallization pH value of 7.5. Interestingly, nHAST pH 8 composite synthesized at crystallization pH of 8, which is not treated at all shows higher performance in fluoride removal, about 67 and 89 % from initial fluoride concentrations of 10 and 5 mg/L, respectively. This is significant as compared with the removal efficiency due to nHAST pH 9 (nHAST composite synthesized according to the patented recipe) with about 61 and 76 % from the same initial fluoride concentrations, respectively.

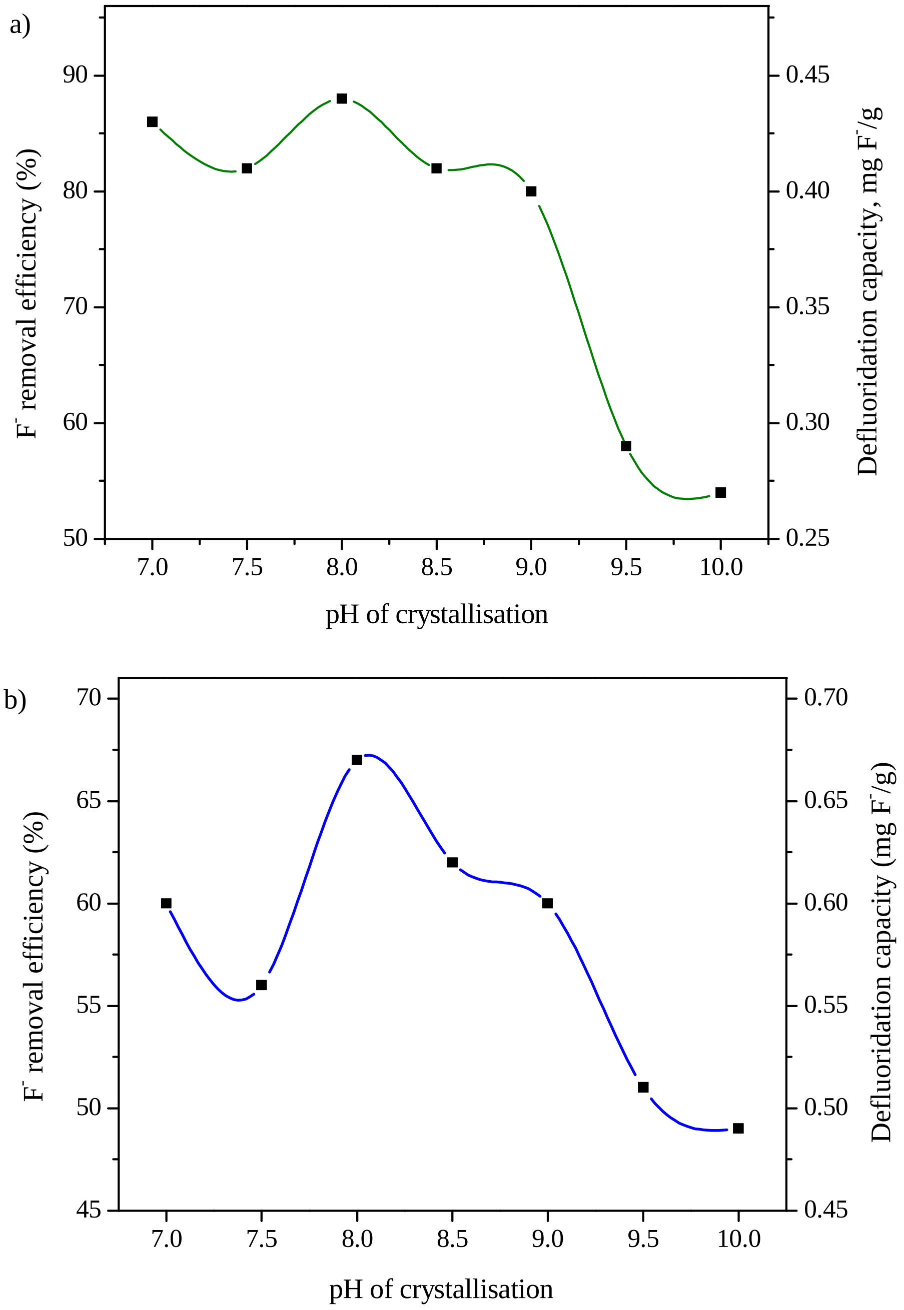

Figure 23: F^- removal performance of the nHAST composites synthesized at different crystallization pH at a) 5 mg/L and b) 10 mg/L initial fluoride concentrations

In the case of nHAST composite samples treated with basic solution, (nHAST pH 8.5/9/9.5/10) the defluoridation capacity starts declining, immediately after nHAST pH 8.5. The lowest minimum fluoride removal capacity was recorded for nHAST pH 10 composite sample (Figure 23a, and b), although the quantity of HAp crystallized remain almost the same as quantified by ICP, Table 8. The variation in fluoride removal capacity among the samples may be explained based on the particle size effect, probably indicating the smallest HAp particles in nHAST pH 8 composite sample. However, the lower defluoridation capacity due to nHAST composite samples synthesized at basic crystallization pH, perhaps indicate the favourability of larger HAp crystals formation in basic media. As identified from Figure 23, this is significant at higher crystallization pH values of pH 9.5 and 10 (nHAST samples treating with more basic solution) as evidenced by their corresponding lower performance in fluoride removal.

In general, the respective order in fluoride removal performance of these samples is as follow: nHAST pH 8 (untreated sample) > nHAST pH 8.5 > nHAST pH 9 > nHAST pH 9.5 > nHAST pH 10. Therefore, the best performing (optimized) crystallization pH for further synthesis of nHAST composite is considered as an autogenous pH value of 8 (without chemical treatment). This is of great importance in contributing to the greener synthesis of nHAST composite preparation, besides to the minimal production cost, both of which are attributed to the elimination of ammonia, the most environmentally hostile among the reagent chemicals used in nHAST composite synthesis.

4.5.3. Crystallisation time optimization

Crystallization time is known to have an important effect on the nature of HAp crystals. In order to investigate the effect of crystallization time in defluoridation performance by nHAST composite, a series of nHAST samples were synthesized at different crystallization time, ranging from 2 to 144 hours while keeping synthesis time and crystallization pH constant at optimum value of 2 hours and pH 8, respectively. The as synthesized nHAST samples were first characterized and then tested in fluoride removal in batch mode as described below.

4.5.3.1. X-ray diffraction analysis result

The X-ray diffraction profiles of the nHAST composite samples as a function of crystallization time are presented in Figure 24. As observed, all the composite samples including the support STI shows very similar diffraction pattern, evidencing the resistance of the STI framework under the synthesis conditions [99]. Moreover, after the growth of HAp on STI surface most of the peaks did not change, but slightly decrease in intensity with respect to the zeolite peak with crystallization time. In this case the scenario was similar to the one in the synthesis time optimization.

However, a closer look at the diffraction patterns of the nHAST composites with respect to STI reveals slight variations in the region between 23 and 25° 2θ angles (Figure 24 sect). In this angle range the initial STI mineral showed three clearly distinguishable peaks characteristic of a monoclinic STI space group, while the nHAST composite samples showed a single diffraction as marked by downward arrow, evidencing a change of the space group to orthorhombic [82, 136]. This can be caused by the almost-complete exchange of Ca^{2+} and Na^{+} ions in the original STI by NH_4^+ ions during the preparation of the composites.

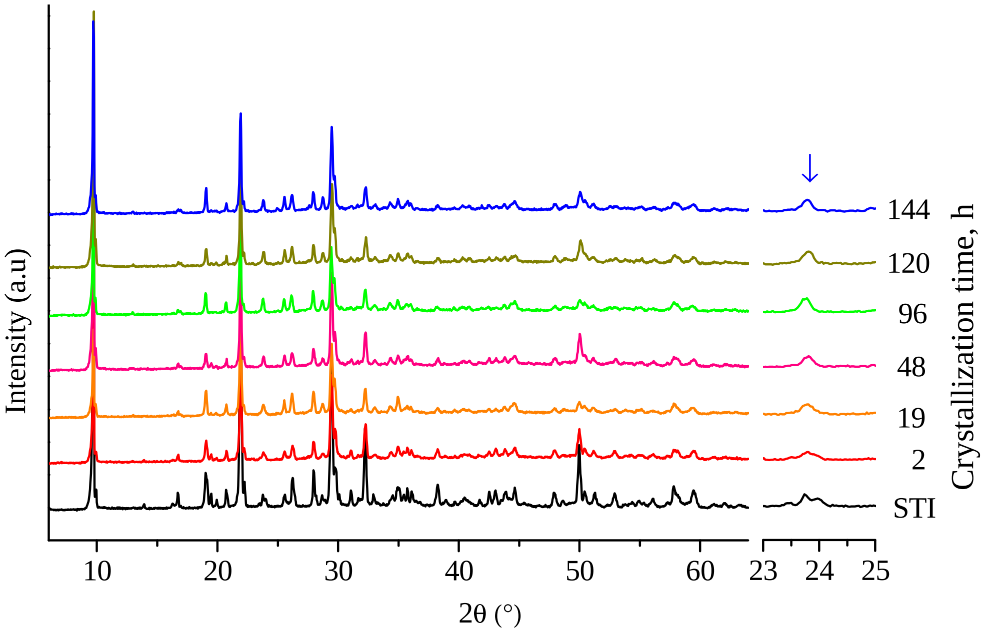

Figure 24: XRD profiles of the support STI zeolite and nHAST composite samples as a function of crystallization time

However, the identification of the characteristic crystalline peaks that confirm the formation of HAp on STI surface by XRD was not possible due to the low concentration of HAp in the composite, its small (nanometric) crystal size or possibility of overlapping with the more abundant and intense STI zeolite diffractions.

4.5.3.2. IR-ATR analysis result

Figure 25 shows the IR-ATR spectra of the nHAST composite samples synthesized at different crystallization time and the support STI zeolite. As shown in the figure, all the spectra look alike. In the support STI zeolite, the band at 1630 cm^{-1} can be assigned to the deformation band of adsorbed water. The STI framework (T-O) asymmetric stretching vibrations appear at 1145 and 994 cm^{-1}, while bands at 790 and

701 cm^{-1} are assigned to the symmetric stretching vibrations. The band at 560 cm^{-1} arises from double ring vibrations, and that at 430 cm^{-1} comes from T-O bending [144, 145]. After the chemical treatment of STI as a function of crystallization time to produce the nHAST composites, the main bands due to the STI framework remained, and a new band arose at about 1430 cm^{-1} due to the presence of NH_4^+ ions after the ion-exchange process during the HAp crystallization. This indicates that the chemical treatment caused the cation exchange of Ca^{2+} by NH_4^+, and agrees with the XRD analysis result. Additionally, new features in the double ring vibration band of the STI framework at around 560 cm^{-1} showed up at about 565 and 606 cm^{-1}, which are consistent with the presence of PO_4^{3-} groups [143] and increases with time. As a result, it is clearly manifested in nHAST samples at longer crystallization time of 144 hours, possibly indicating the crystallization of more HAp as a function of time.

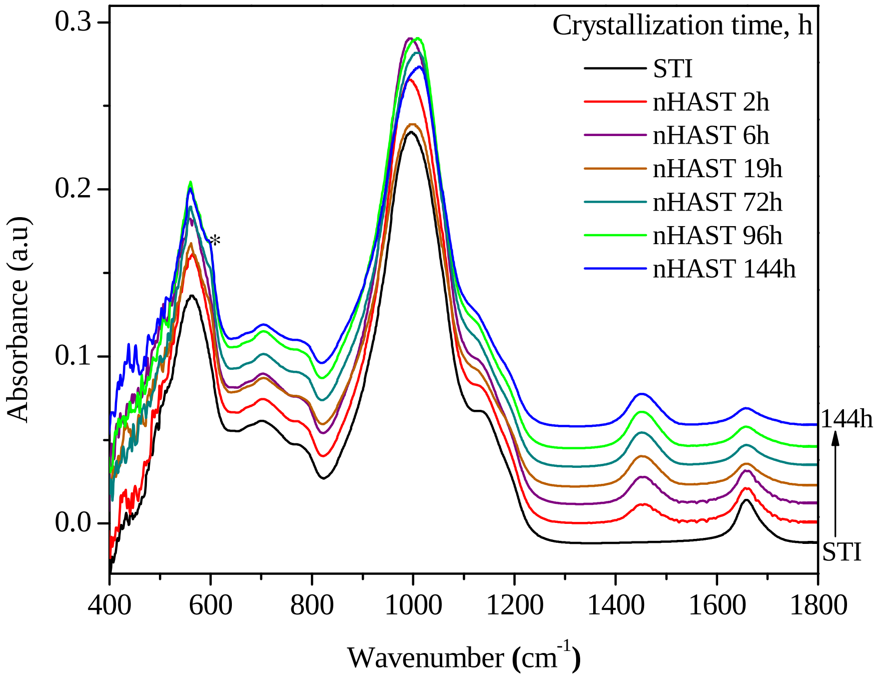

Figure 25: IR-ATR spectra of a support STI zeolite and nHAST composite samples as a function of crystallization time

4.5.3.3. Thermogravimetric analysis

Thermogravimetric analysis, TGA was carried out on selected nHAST composite samples synthesized as a function of crystallization time. The thermogravimetric analysis result presented in Figure 26 shows TGA-DTG curves of the support STI and nHAST composite samples. It is clearly seen from the figure that in low temperature region alone, two differentiated weight losses can be observed in both the STI sample and the nHAST composite samples. In STI, a first weight loss at temperatures below 130 ºC is assigned to loosely attached water, while a second strong weight loss with maximum desorption rate at around 170 ºC and other of a lower desorption rate at about 260 ºC are due to desorption of strongly retained water molecules within the STI framework by coordination with exchangeable Ca^{2+} ions.

The slight shift of weight loss for dehydration to the lower temperatures was clearly observed in the case of nHAST samples, possibly because of the weaker interaction of water molecules with monovalent NH_4^+ ions exchanged for Ca^{2+} ions in nHAST case as compared to stronger interaction with divalent Ca^{2+} ions in original STI sample.

Furthermore, maximum weight loss in nHAST 2h sample, synthesized at shorter crystallization time of 2 hours, was observed at a slightly higher temperature of around 160 ºC as compared to other nHAST samples synthesized at longer crystallization time, due to structural absorbed water molecules with stronger interactions. The maximum water desorption shift finally showed up at about 150 ºC in nHAST 144h sample, synthesized at crystallization time of 144 hours. The slow water desorption shift of nHAST samples toward the lower temperature region with crystallization time is due to the exchange of more and more divalent Ca^{2+} by monovalent NH_4^+ ions, Figure 26. This one indicates a slow shift from strong water-Ca^{2+} ion (divalent) interaction toward the lesser interaction of water-NH_4^+ ion (monovalent) with crystallization time.

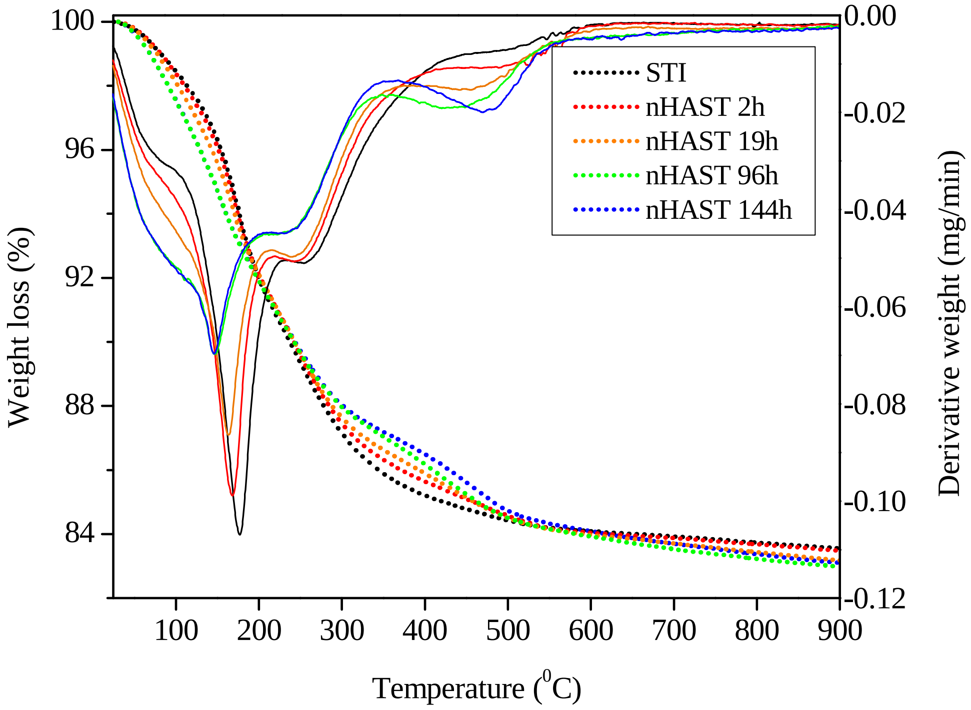

Figure 26: TGA (doted lines) and DTG (solid lines) of STI and nHAST composite samples

Similar scenario was also observed in another water desorption band of lower weight loss, again due to structurally absorbed water molecules. In this case, the maximum weight loss in nHAST 2h sample was observed at about 260 ºC whereas the maximum water desorption shift expected in nHAST 144h sample with the longest crystallization time showed up at about 250 ºC, Figure 26. Interestingly, in both situations the water desorption intensity decreases significantly with time until the equilibrium was fully established at nHAST 144h composite sample, suggesting minimal or no more exchange of Ca^{2+} by NH_4^+ ions. Furthermore, desorption of water at temperatures below 160 ºC is much more intense for the nHAST composite samples, while desorption of strongly-bonded coordinated water molecules at higher temperatures is much smaller as a consequence of the exchange of more amount of Ca^{2+} by NH_4^+ ions, which weakly or do not coordinate water molecules, and hence the major water desorption occurs at low temperature.

Besides, in nHAST composite samples additional new broad peak was arose at around 450 ºC due to deammmoniation, indicating the release of NH_3 as NH_4-STI transforms into H-STI [82, 144]. The deammmoniation band shows an increasing trend, indicating the release of more and more $NH_3$with time and thus, shows increasing ion exchange of Ca^{2+} by NH_4^+ ions. Therefore, an indirect conclusion would be that the amount of Ca^{2+} ions released to the solution has increased as a function of crystallization time, leading to the crystallization of proportionate increasing amount of HAp on STI surface. However, the deammmoniation peak of nHAST 144h sample showed up at slightly higher temperature of about 465 ºC possibly attributed to the phase transition of the support STI zeolite from monoclinic to orthorrombic due to the total exchange of Ca^{2+} in STI by NH_4^+ ions in nHAST 144h sample.

4.5.3.4. ICP elemental analysis result

As shown in Table 9, the ICP analysis detected the release of significant, but constant quantity of Ca^{2+} ions in the final nHAST composite samples, irrespective of crystallization time. No P was detected at all in the original STI, while small amount of P was detected in nHAST composite samples. As observed in the figure, the % of P content in the composite samples is slowly increasing as a function of crystallization time.

Table 9: ICP elemental analysis result of the support STI and nHAST composites synthesized at different crystallization time

Samples	**Al** (% wt)	**Si** (% wt)	**Na** (% wt)	**Fe** (% wt)	**Ca** (% wt)	**P** (% wt)	**HAp** %
STI	8.0	20.4	0.5	1.6	4.9	0.0	—
nHAST, 2h	8.2	19.4	0.4	2.0	5.4	0.3	1.6
nHAST, 6h	8.5	20.6	0.4	2.0	5.5	0.6	3.2
nHAST, 19h	8.2	19.3	0.4	2.0	5.6	0.9	4.9
nHAST, 72h	8.2	20.4	0.2	2.0	5.6	1.4	7.6
nHAST, 96h	8.4	20.1	0.2	2.1	5.6	1.6	8.6
nHAST, 144h	8.5	20.5	0.2	2.1	5.5	1.7	9.2

The amount of HAp crystallized on the STI surface was determined as usual from the P wt % content measured by ICP, according to eq. 11. As shown in the table, a notable increase of the HAp crystallization is observed when increasing the time, possibly due to the reagent materials may have better contact with time. This is significant in nHAST 144h sample synthesized at longer crystallization time, 144 hours, where possibly most of all the exchanged Ca from the zeolite is reacted and crystallizes as HAp as compared with others. This finding fits very well with both IR-ATR and TGA investigation results.

4.5.3.5. Defluoridation test results

Batch adsorption experiments were carried out to test the fluoride performance of nHAST composite samples synthesized at different crystallization time using initial fluoride concentrations of 5 and 10 mg/L at 10 g/L adsorbent dose for a contact time of 20 hours with continuous agitation at room temperature. Figure 27 describes the fluoride removal efficiency as well as the corresponding final equilibrium fluoride concentrations as a function of crystallization time.

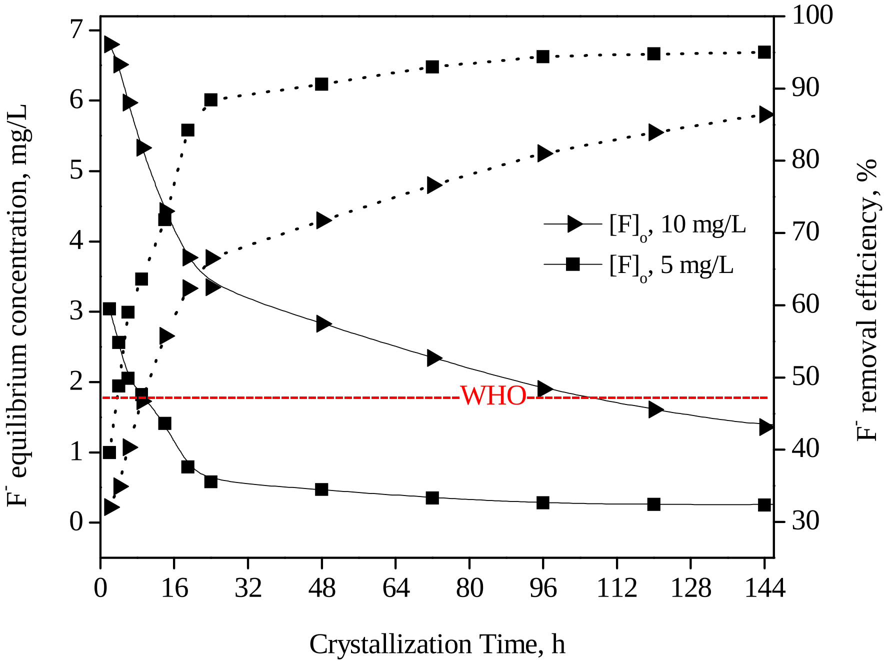

Figure 27: F^- equilibrium concentration (solid lines) and removal efficiency (dotted lines) as a function of crystallization time of nHAST composite samples

As clearly observed from the figure, nHAST 2h synthesized at shortest crystallization time (2 hours) shows low fluoride removal performance, only 39.6 and 32 % from 5 and 10 mg/L initial fluoride concentrations. However, the trend in fluoride removal has improved significantly with time, and rapidly increasing up to nHAST 24h, sample at 24 hours crystallization time, where the equilibrium was nearly achieved with high fluoride removal efficiency of 88.4 and 66.5 % from initial fluoride concentrations of 5mg/L (blue line) and 10 mg/L (green line), respectively. The corresponding final equilibrium fluoride concentrations were found to be 0.58 and 3.35 mg/L, from 5 and 10 mg/L initial concentrations. Because the final equilibrium fluoride concentration with respect to 10 mg/L, 3.35 mg/L, was significantly exceeded the WHO maximum permissible level of 1.5 mg/L, further optimization of nHAST at higher crystallization time, up to 144 hours were studied. As shown in Figure 27, the fluoride removal study results of these samples also indicated the increasing trend, but slowly until at nHAST 144h sample at crystallization time of 144 hours. At this sample the measured final equilibrium fluoride concentration was found to be 1.60 mg/L, very close to the WHO maximum permissible limit at 10 mg/L initial fluoride concentration with fluoride removal efficiency of about 84 %. At the same adsorbent dose if the initial fluoride concentration lowers to 5 mg/L, the fluoride removal efficiency increases significantly, 95 %. This yields lower equilibrium fluoride concentration of about 0.25 mg/L, significantly lower than the WHO stetted safe range. Therefore, crystallization time of 144 hours is considered as an optimum time for further preparation of nHAST composite.

Following, the associated fluoride removal capacities of the composites as a function of crystallization time were investigated using 10 mg/L fluoride initial concentration at a dose of 10 g/L. Figure 28 shows the clear relationship between the amounts of HAp (in wt %) crystallized in nHAST composites and the associated fluoride removal capacity as a function of crystallization time. When the crystallization time increases, both the amount of HAp crystallized and the corresponding defluoridation capacity notably increased, even if the presence of large amount of low performing STI zeolite in nHAST composite materials. This possibly indicates the growth of smaller HAp crystals in the longer crystallization time. Therefore, the fluoride removal capacity as a consequence of the amount and crystal size of HAp crystallized can be controlled by adjusting the crystallization time.

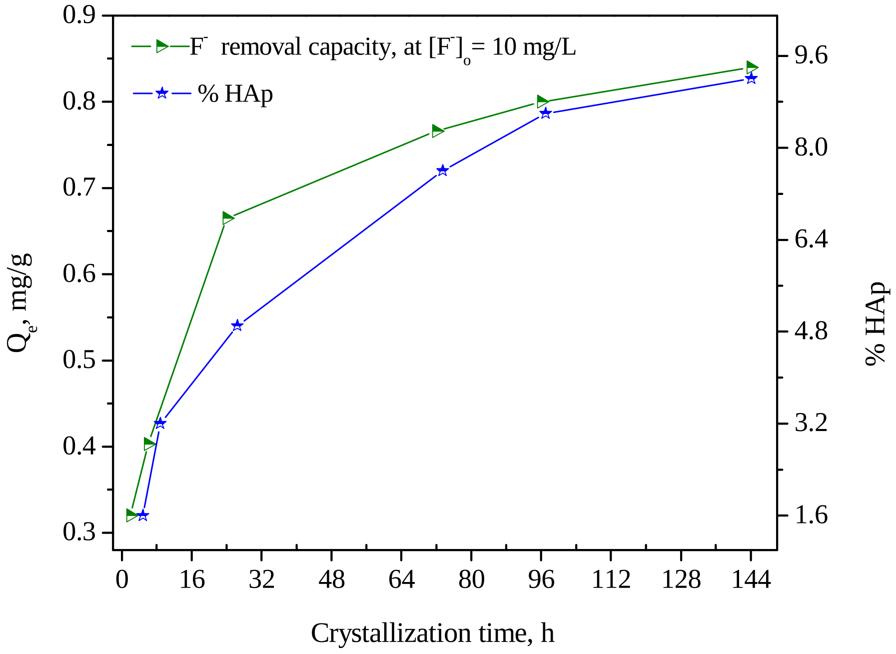

Figure 28: Percent HAp crystallized in nHAST composites and the corresponding defluoridation capacity as a function of crystallization time at 10 g/L dose

In order to fully understand the nature of the nHAp crystals and how it affects the high fluoride removal performance, further structural studies were conducted using ^{31}P MAS-NMR and advanced Electron Microscopy Techniques (STEM/HAADF/EELS). Selected samples were further studied: nHAST 144h and nHAST 19h in order to evaluate the growth of the nHAp crystals with crystallization time.

4.5.3.6. ^{31}P MAS-NMR analysis result

The ^{31}P MAS-NMR analysis carried out on the selected composite samples nHAST 19h (solid line) and nHAST 144h (solid line) synthesized at crystallization pH 8. Two other NMR spectra, nHAST 19h at crystallization pH 9 (dashed line), from the previously patented research work and atypical HAp (dotted line) samples were included for comparison purpose. As shown in Figure 29, in all composite samples the same signal as typical HAp (dotted line) is observed at around 2.85 ppm, characteristic of P in HAp, confirming the formation of HAp in the composites [125, 148]. However, in nHAST 19h (solid line) and nHAST 144h (solid line) composites synthesized at crystallization pH 8 of this study, the band is broader as compared to the typical HAp materials (dotted line). Furthermore, it developed a shoulder at around 0 ppm, both being features related to the nanometric nature of HAp crystals [98, 149].

Interestingly, the NMR spectra of our composites, nHAST 19h and nHAST 144h at crystallization pH 8 were even broader than nHAST 19h composite synthesized at crystallization pH 9 (dashed line), suggesting the presence of even the smaller HAp particles in nHAST 19h and nHAST 144h composites at pH 8, Figure 29. If nHAST 19h and nHAST 144h composites from this study compared with one another, the band due to nHAST 144h (solid line) is still slightly broader, again suggesting the crystallization of even smaller size HAp at longer 144 hours crystallization time and room temperature conditions. Therefore, with ^{31}P NMR technique we can confirm the notably reduced HAp particle to nanometric size in nHAST 144h composite under investigation.

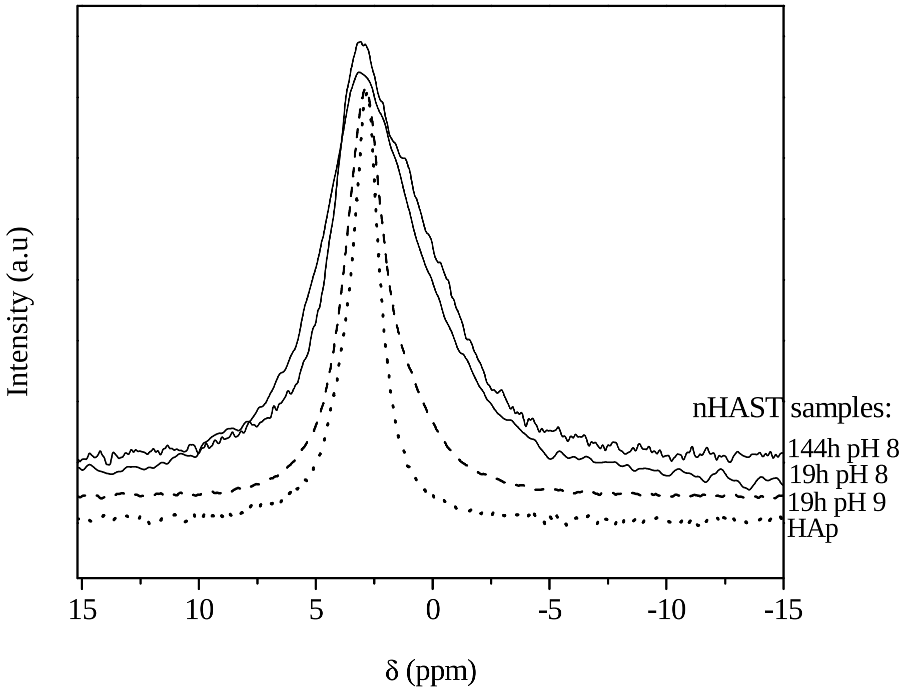

Figure 29: ^{31}P MAS-NMR spectra of nHAST 144h at pH 8 and nHAST 19h at pH 8 (solid lines), and nHAST 19h at pH 9 (dashed line), and HAp (dotted line)

4.5.3.7. Advanced electron microscopy results

Scanning transmission electron microscopy (STEM) coupled with High Angular Annular Dark Field (HAADF) detector was chosen to study nHAST 19h and nHAST 144h composite samples in order to fully comprehend the evolution of the HAp crystallized on STI surface as a function of crystallization time. Cs-corrected STEM/HAAD F mode was selected given the beam sensitivity of both materials under the electron beam. These high-resolution observations may allow investigating the growth of the hydroxyapatite crystals over the surface of stilbite. Figure 30 demonstrates the crystallization of HAp on the external surface of STI zeolite. In Figure 30a HAp nanocrystals are clearly shown in the images as very thin hairy crystals protruding from the STI homogeneous surface. Using this mode, we managed to obtain high-resolution images of the HAp layered structure with a d spacing of 2 Å (in the inset of Figure 30b) which highest resolution ever reported for HAp structure. Furthermore, chemical composition could be identified using Electron Energy Loss Spectroscopy (EELS). STEM/HAADF/EELS mapping (Figure 30c) analyses performed over the area marked in green clearly show the crystallisation of HAp on the external surface of the STI zeolite, distinguishable by its main constituent element P, blue colour (not present in the STI zeolite) and Ca, green colour (present in both, as originating from STI itself), attached to the surface of the zeolite crystals, whose identifying element is Si (red colour). As it can be observed in nHAST composite samples, red color follows a sharp surface corresponding to the STI crystal, whereas green color, Ca and blue color, P of the HAp draws thin irregular forms on the surface of STI zeolite.

As crystallization time increases to 144 hours, the growth of HAp will cover the surface of the stilbite crystals in a heterogeneous manner but yet, linked to the zeolite crystals, i.e. no separate HAp crystals are observed, which means that the surface of the stilbite acts as source of nucleation points, and later on, the crystals grow to connect these nuclei leading to a full covered surface, as shown in Figure 30a.

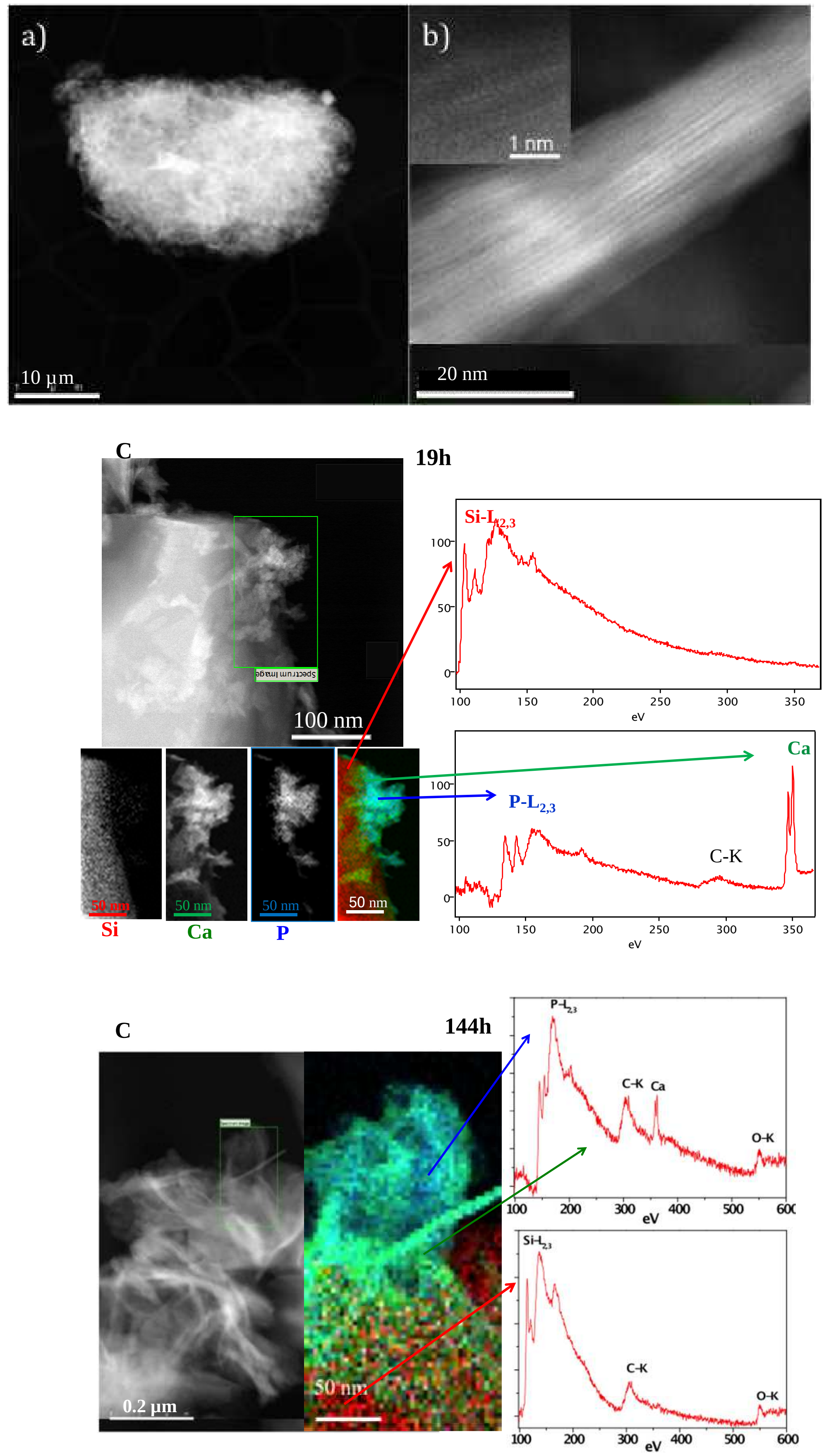

Figure 30: STEM/HAADF/EELS results on nHAST 19h and nHAST 144h

STEM/HAADF/EELS mapping observations clearly show a notable increase of HAp crystallization on the external surface of the zeolite at longer time, suggesting that most of the Ca^{2+} from the zeolite is exchanged and crystallizes as HAp at higher crystallization time. Figure 30c includes an EELS analysis of the area marked with the green box, confirming that P and Ca are the main components of the thin hairy crystals, while Si is the main component of the uniform larger crystals underneath. In this case, the STI crystals are rather well covered by HAp thin-layered crystals. Indeed, significantly higher amount of HAp crystals are clearly observed in nHAST 144h sample as hairy needles as shown in Figure 31. This is in good agreement with the ICP analysis result in Table 9. Thus, adjusting the crystallization time can control the amount of HAp crystallized.

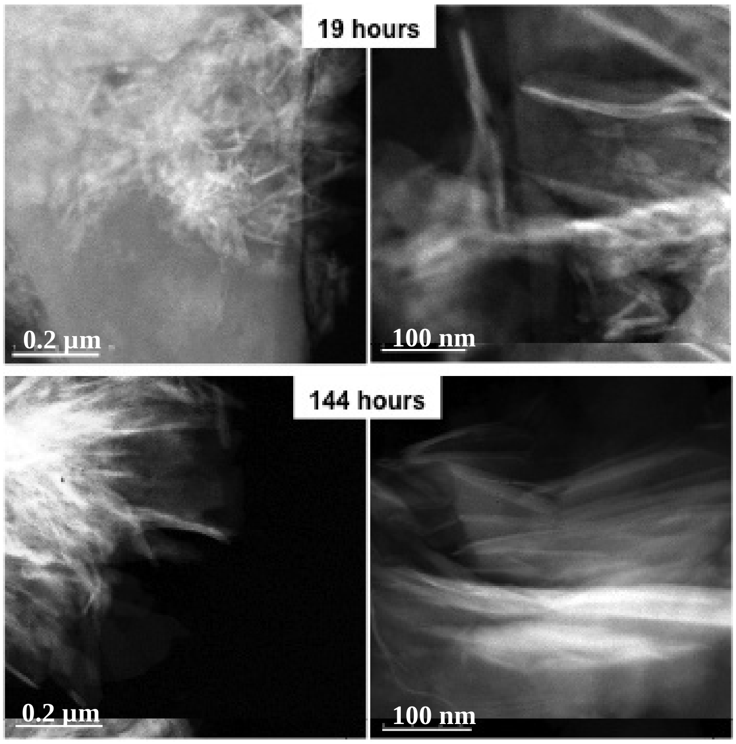

Figure 31: Comparison of STEM images at different magnification for HAp grown on stilbite surface for nHAST 19h and nHAST 144h samples

4.5.3.8. Point of zero charge determination

Potentiometric mass titration technique was used for the determination of the PZC of the support STI zeolite and nHAST 144h composite samples. Figure 32 and 33 clearly show the pH of point of zero charge, as identified by the common intersection point of the potentiometric curve of the blank solution with the corresponding curves of the support STI zeolite and nHAST 144h adsorbent materials, respectively, containing 0.5, 1.0, and 1.5 g in 0.02 N $NaNO_3$ electrolytic solutions. The PZC value of natural STI was confirmed to be very low, about 2.1, indicating that only small portion of the surface, that is below pH 2.1 was positively charged, this in turn shows that fluoride adsorption through electrostatic attraction is not favorable.

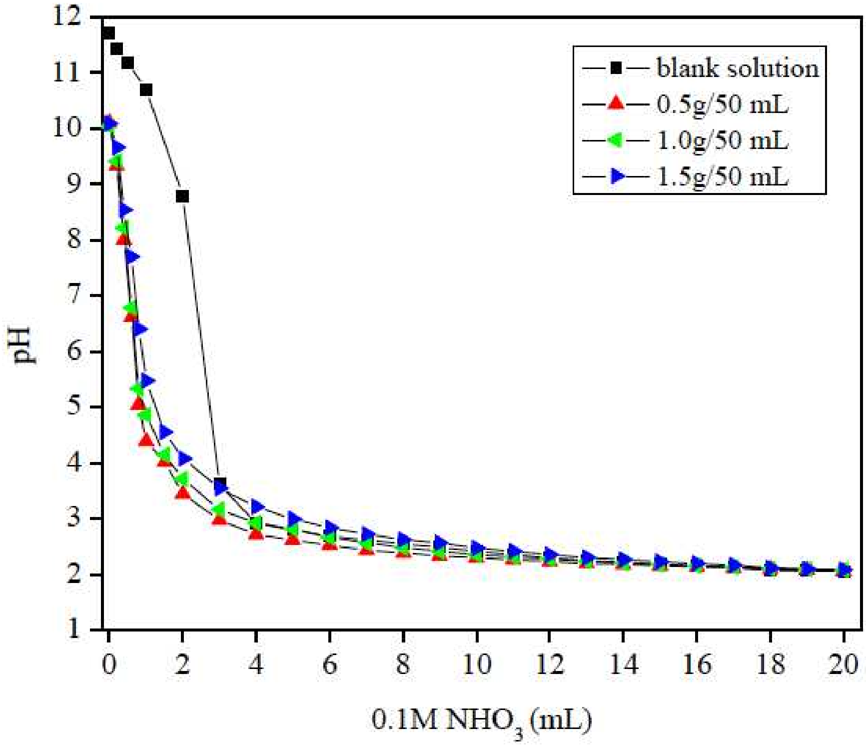

Figure 32: Experimental curves corresponding to the potentiometric mass titration technique for the determination of the PZC of natural STI zeolite

However, the PZC of nHAST 144h was confirmed to be very high, about 10, as compared to the parent support STI zeolite, as identified from Figure 33. This shows significantly large portion of nHAST 144h surface, below PZC 10, positively charged. Therefore, nHAST 144h composite is highly suitable for fluoride adsorption through electrostatic attraction. The experimental finding from PZC is agreed well with the defluoridation test result, which reported high defluoridation capacity for nHAST 144h adsorbent and low in STI zeolite case. Note that nHAST 144h sample now on simply called nHAST composite.

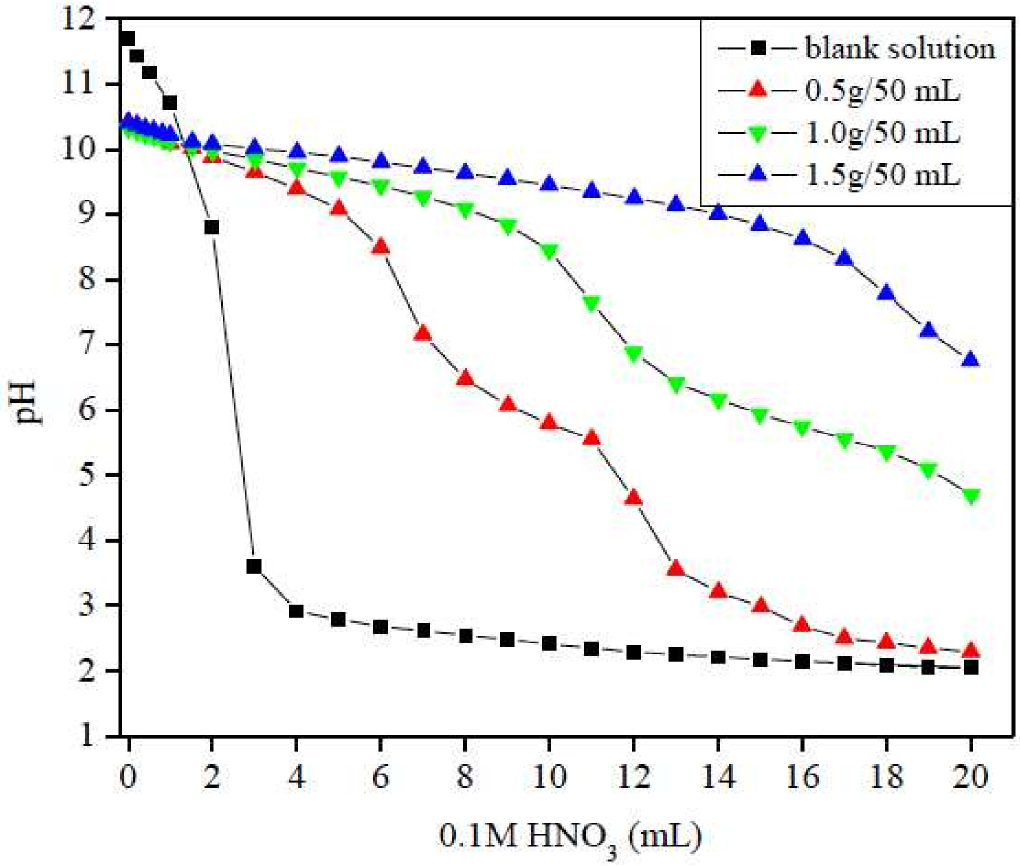

Figure 33: Experimental curves corresponding to the potentiometric mass titration technique for the determination of the PZC of nHAST 144h

4.6. Factors affecting fluoride adsorption onto nHAST

The effect of most important process parameters such as adsorbent dose, contact time, effect of initial fluoride concentration, solution pH effect, effect of co-ions on the adsorption of fluoride ions by nHAST composite as well as the possibility of regenerating have been explored under this section.

4.6.1. Effect of adsorbent dose

The influence of adsorbent dose on fluoride removal efficiency of nHAST was studied at 4, 6, 8, 10 and 12 g/L dose. The study was performed using initial fluoride concentrations of 5 and 10 mg/L for a contact reaction time of 20 hours at room temperature. As described in Figure 34, the fluoride removal efficiency notably increases with increasing adsorbent dose up to 10 g/L due to the availability of more number of fluoride binding sites. As identified, the equilibrium was fully established at 10 g/L dose with high fluoride removal of about 95 and 84 % from 5 and 10 mg/L initial fluoride concentrations, respectively. Because the equilibrium fluoride concentration falls within the WHO limit, and no significant change on the efficiency beyond this, a dose of 10 g/L was considered as an optimum dose for further adsorption experiments.

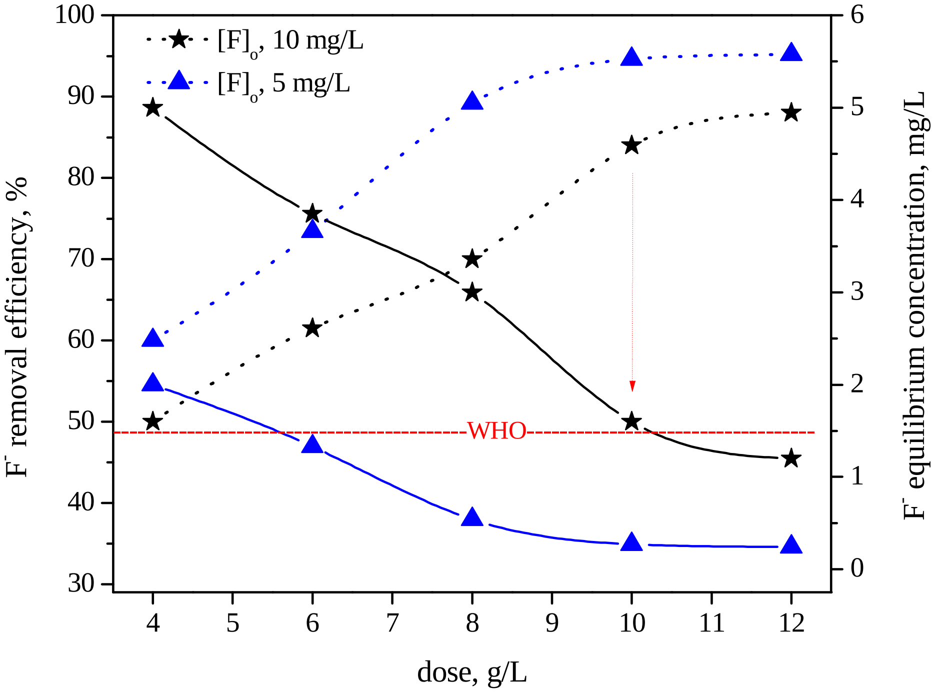

Figure 34: The effect of adsorbent dose on fluoride removal efficiency (dotted lines) and fluoride equilibrium concentrations (solid lines) by nHAST composite

4.6.2. Effect of contact time

In order to identify the dynamics of the adsorption process, batch experiments were carried out using different contact times at 10 g/L, optimized dose and 10 mg/L initial fluoride concentration at room temperature reaction conditions. As shown in Figure 35, rapid fluoride removal was observed up to 8 hours reaction time. During this time high removal efficiency was recorded, about 81 %. The reaction proceeds slowly and at 20 hours reaction time the equilibrium is fully attained with fluoride removal efficiency of about 84 %. Since there is no significant increase of the fluoride adsorption beyond this, the contact time of 20 hours was fixed for further study.

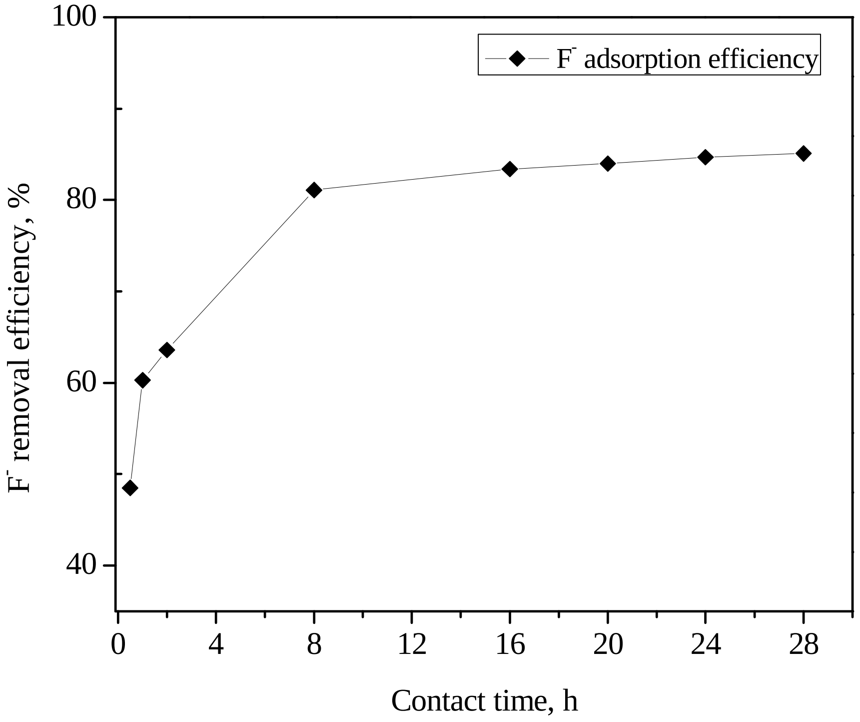

Figure 35: Fluoride removal efficiency as a function of contact time at 10 g/L dose of nHAST composite (C_o = 10 mg/L)

The composite, nHAST adsorbent shows significantly high performance as compared to its support precursor STI with very low removal efficiency. This is due to not only the presence of new active sites, but the high efficiency of nanometric size HAp crystals in nHAST as evidenced by ^{31}P MAS-NMR and STEM analyses. Thus, the high activity as reflected by the fast fluoride adsorption up to 8 hours time is due to ion exchange with such sites, surface hydroxyl ions on the nHAST. However, the later slow adsorption stage is probably the result of the gradual and slow uptake of the adsorbed fluoride to the inner adsorbent surface.

4.6.3. Effect of initial fluoride concentration

The effect of initial fluoride concentration on fluoride removal of nHAST adsorbent was studied using fluoride concentrations ranging from 2 to 200 mg/L. An adsorbent dose and contact time were kept constant at 10 g/L and 20 hours, respectively with continuous agitation at room temperature. Note that data of sample 1 and 2 were taken from real ground water sample analysis test result by nHAST composite, the detail is presented in section 5.6.6).

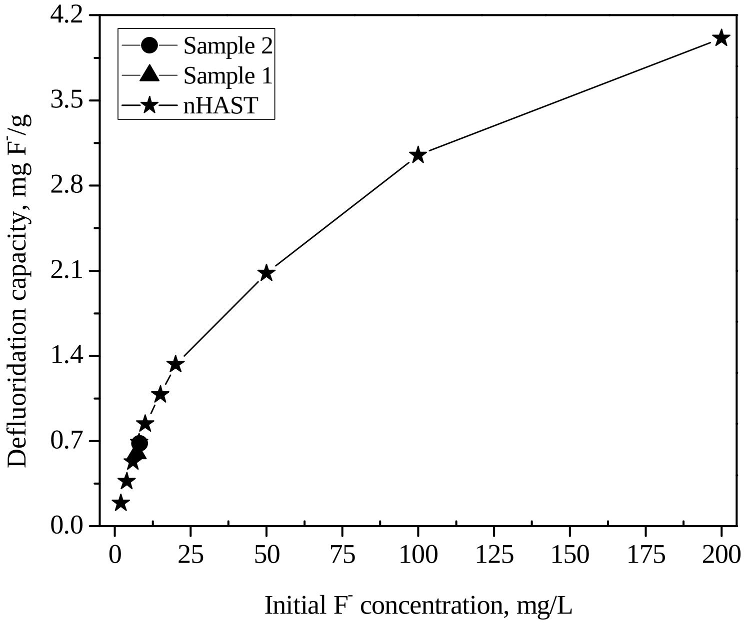

Figure 36: Effect of initial fluoride concentration onto nHAST composite fluoride removal capacity, studied at 10 g/L dose

As shown in Figure 36, the defluoridation capacity increases with increasing initial fluoride concentration. It is significant at lower initial concentrations, up to 20 mg/L due to the utilization of more accessible energetically active sites on the adsorbent surface. Interestingly the capacity keeps on increasing, at slower rate, until it reaches the final maximum initial fluoride concentration of 200 mg/L. This can be attributed to the utilization of less accessible sites because of increased diffusivity and activity of fluoride upon the increased concentration. It also indicates the heterogeneity of sites that are unevenly distributed on rough surface. In fact, the SEM image in Figure 37 clearly shows that nHAST had a significantly rough surface and lots of pores.

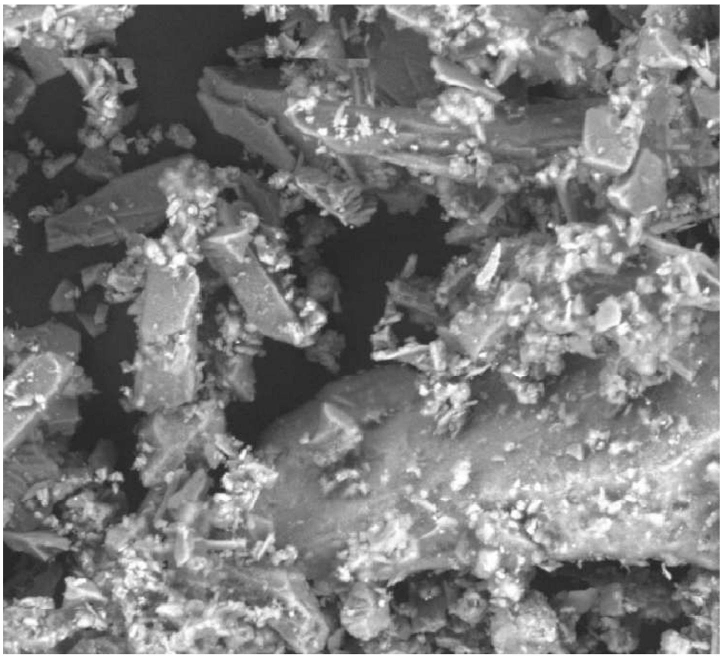

Figure 37: SEM micrograph of nHAST composite

4.6.4. Effect of solution pH

The effect of solution pH was investigated with initial fluoride concentration of 10 mg/L, adsorbent dose of 10 g/L for a contact time of 20 hours stirring continuously at room temperature conditions by varying the initial solution pH from 3 to 10, using 0.1 M HCl or 0.1 M NaOH. Figure 38 demonstrates the influence of initial solution pH on the fluoride removal efficiency of nHAST composite adsorbent. It is evident that the percentage of fluoride removal initially, at pH < 6.5, increases slowly against solution pH and reaches a maximum at pH 3, with 86 % fluoride removal. Further increase in the solution pH, pH > 6.5, decreases the fluoride removal efficiency, again slowly until it reaches at the lower value of about 79 % fluoride removal at pH 10. This is only 7 %

lower than the maximum efficiency at pH 3. The minimal solution pH effect in fluoride removal of nHAST adsorbent may be attributed to the nature of its surface charge. The nHAST composite has a PZC of about 10.0 (refer to Figure 33), which means that the surface of the adsorbent presents a net positive charge when pH is less than 10.0.

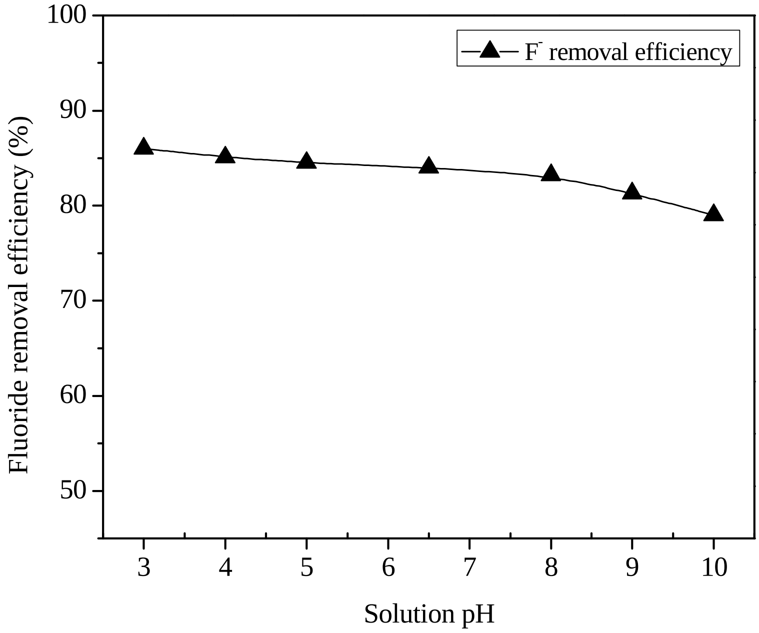

Figure 38: Effect of solution pH on fluoride removal of nHAST composite

Anyhow, the slightly higher efficiency at pH less than 6.5 may be ascribed to the gradual increase in attractive forces against solution pH, whereas the relatively lower efficiency in alkaline medium can be explained by the competition between the OH^- and F^- ions for the adsorption sites. Note that pH of 6.5 is the real solution pH (only of nHAST and F^- solution mixture) without pH adjustment.

It is already known that most adsorbents used in fluoride removal have narrow working pH ranges, and usually show optimum performance in acidic pH range. However, the pH of natural groundwater with high fluoride content is in the range of

7.6 to 8.6 in most cases [46, 150]. Within this pH range, unlike most other defluoridation adsorbents, nHAST composite shows high performance, about 84 % removal efficiency at 10 g/L dose and initial fluoride concentration of 10 mg/L (Figure 38). Interestingly, the performance remains comparably high in the pH range under investigation: pH 3 to 10, between 79 % at pH 10 to 86 % at pH 3 removal efficiency, indicating the minimal solution pH effect on fluoride removal by nHAST composite.

4.6.5. Effect of co-existing anions

Varieties of other anions are generally present in groundwater, and may compete with fluoride ions for adsorption on the nHAST adsorbent. In order to investigate their effect on fluoride removal, batch adsorption experiments were done in the presence of 100–500 mg/L concentrations of chloride, sulfate and bicarbonate solutions in 10 mg/L fluoride solution. Figure 39 describes their effect on the fluoride removal efficiency of nHAST composite. When no competing ions were present, over 84 % of fluoride was adsorbed from 10 mg/L initial fluoride concentration. The final residual solution pH in this case was about 7. In the presence of bicarbonate ions the fluoride removal efficiency decreases while increasing the concentration. This effect is significant at higher concentrations of 300 mg/L or higher. As observed, the efficiency decreased significantly from about 84 % when no competing ions to 65 % in the presence of 500 mg/L HCO_3^- ions, possibly due to the change in pH as well as the stronger competing effect of HCO_3^- ions. However, other ions such as chloride and sulfate show no significant effect within the concentration range tested.

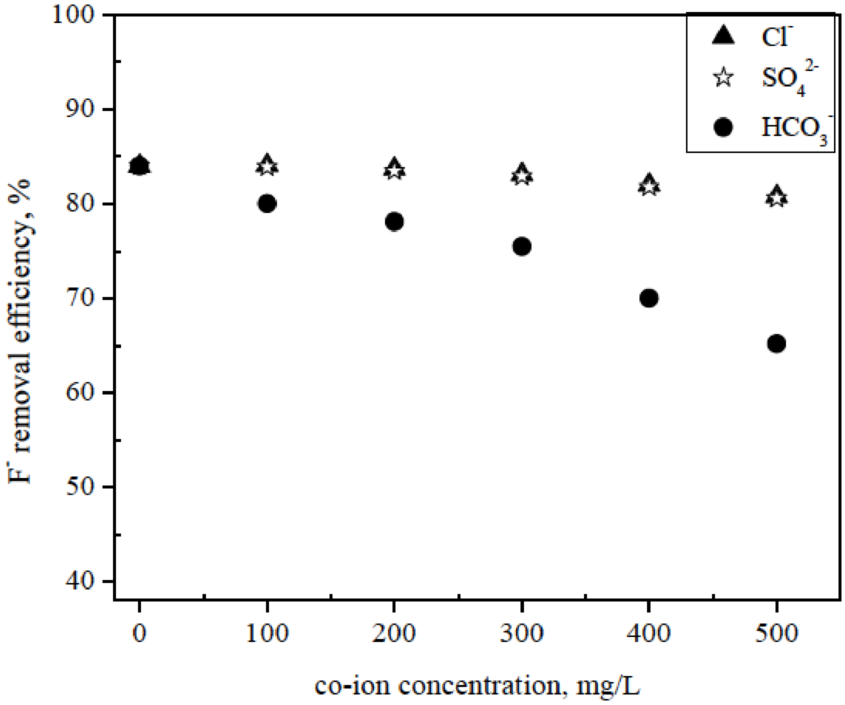

Figure 39: Effect of coexisting ions on fluoride removal of nHAST composite, studied at 10 g/L dose

In general, the change in removal efficiency when the coexisting ion concentration is below 300 mg/L is almost insignificant (Figure 39). This possibly indicates the higher selectivity of nHAST for fluoride, even if detailed mechanistic aspect of the competitive adsorption reactions requires further investigation.

4.6.6. Regeneration of nHAST composite

In order to ensure a complete saturation of the adsorbent material, successive defluoridation treatments were conducted before regeneration experiments, using initial fluoride concentration of 10 mg/L and 10 g/L dose. Results clearly show that the defluoridation capacity was not exhausted after the first defluoridation treatment, Figure 40. In fact, the capacity in the second use-cycle is nearly half the capacity of the first treatment, from 0.84 to 0.48 mg F^-/g. However, after the second treatment the nHAST shows insignificant defluoridation capacity, 0.05 mg F^-/g, and thus regeneration study has started here. The overall capacity after these cycles was 1.37 mg F^-/g.

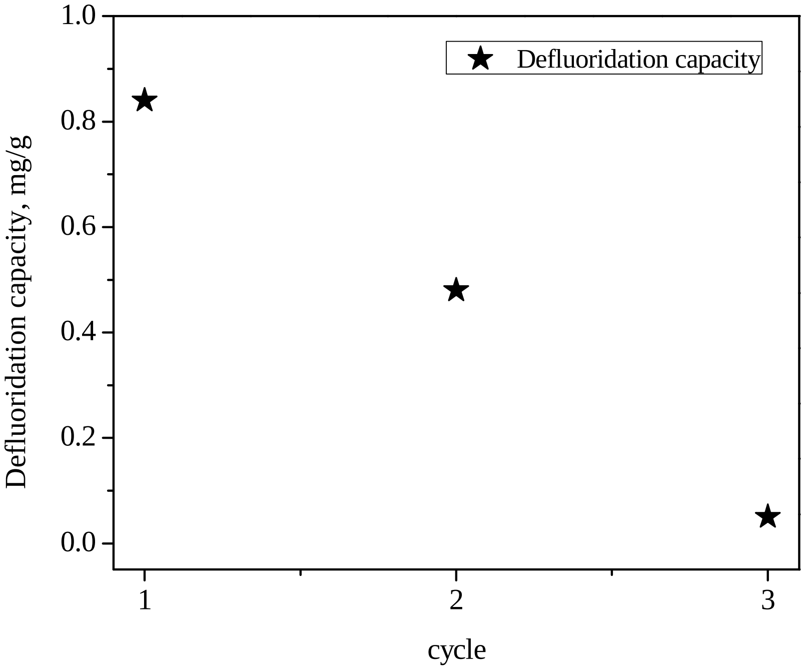

Figure 40: Defluoridation capacity of nHAST composite in consecutive cycles before regeneration

The possibility of regenerating the adsorbent was studied using 0.50 g of saturated nHAST in 100 ml of 0.1M/0.01M NaOH solution (5 g/L) at various contact times. The regenerated residue (nHAST) was then separated by filtration, washed with plenty of distilled water, air dried and characterized.

In this particular study only powder X-ray diffraction analysis was used. Figure 41 shows the XRD patterns of the regenerated adsorbent samples (nHAST 0.01M 24h, nHAST 0.1M 3*3h, and nHAST 0.1M 24h) treated with NaOH solutions. As clearly observed from the figure, as compared with the untreated reference nHAST sample, all the samples resisted the basic treatment.

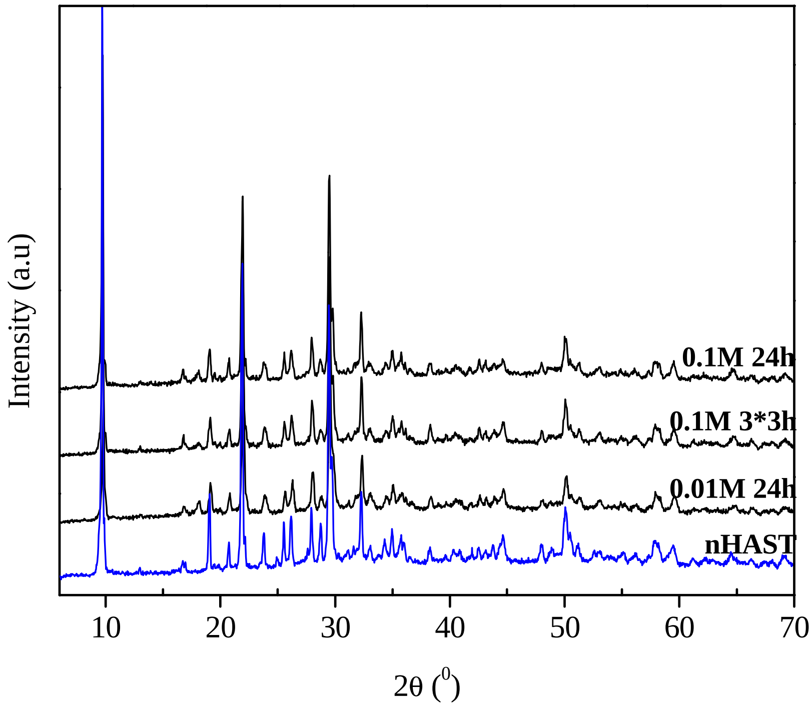

Figure 41: XRD patterns of the regenerated nHAST adsorbent samples

The regenerated adsorbent, after being washed thoroughly with distilled water until it is free from fluoride, were put to repeated use in adsorption study. The result show that desorption of fluoride is effective in three successive treatments in 0.1M NaOH, by renewing basic solutions at 3 hours time for a total of 9 hours. The overall defluoridation capacity of this sample was found to be 0.63 mg F^-/g, significantly lower than the original nHAST with an overall capacity of 1.37 mg F^-/g. The exhausted adsorbent was again subjected to the same desorption treatment as before as shown in Figure 42. In the 2nd cycle of operation, again the capacity was decreasing noticeably, from 0.63 in the first cycle to 0.41 mg F^-/g, after three tests.

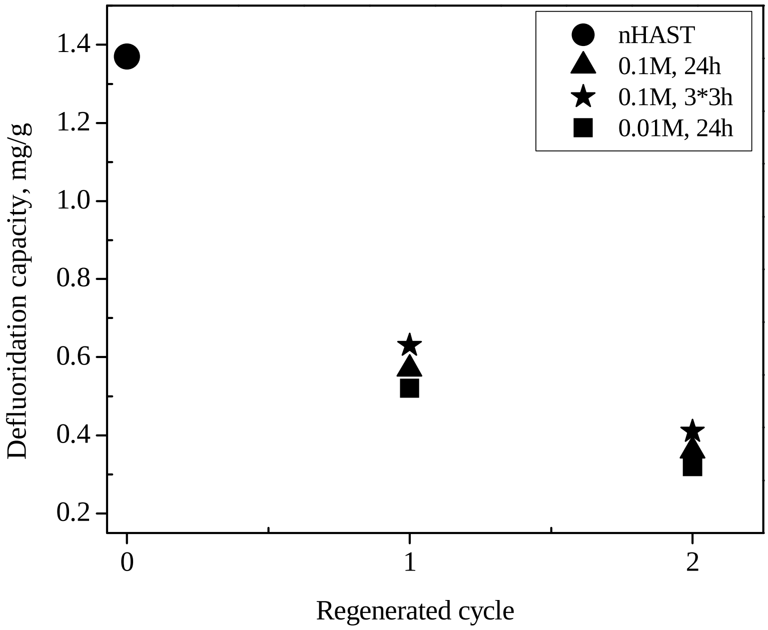

Figure 42: Effect of regeneration on defluoridation capacity of nHAST

The defluoridation efficiency of the regenerated samples, nHAST 0.1M 3*3h, nHAST 0.1M 24h and nHAST 0.01M 24h were found comparably low, 54, 50, and 47 %, respectively as shown in Figure 43. Note that the original nHAST removes about 84 % fluoride. As identified in the figure, the regenerated samples in general are exhausted almost completely in the 2nd defluoridation treatment, sooner than the original nHAST composite. The decrease in fluoride removal capacity as well as efficiency after regeneration may be due to the treatment with highly alkaline solution of regenerating media, and the details need to be further investigated.

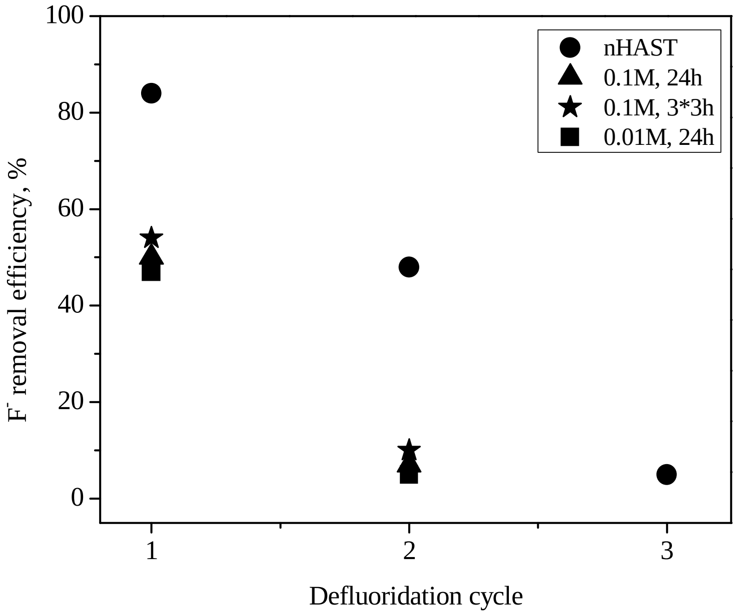

Figure 43: Fluoride desorption test of regenerated adsorbent samples

4.6.6. Fluoride removal on real groundwater from Ethiopian Rift Valley

Finally, the potential of nHAST was tested at field condition with the fluoride containing real groundwater samples, sample 1 and 2, collected from a nearby village near Maki Town, in the Ethiopian Rift Valley fluoride endemic area. Table 10 lists the detailed characteristics of the water before and after the treatment. As shown in the table, when untreated water sample 1 and 2 were subjected to a defluoridation treatment at a dose of 10 g/L and a contact time of 20 hours, about 83 % of fluoride was removed in both cases. The corresponding final fluoride concentration was found to be 1.2 and 1.4 mg/L, respectively, giving same final pH of about 8.10. Unexpectedly, their respective fluoride removal efficiency was found to be slightly lower than that in lab made fluoridated water solution with 84 % removal efficiency from higher initial concentration of 10 mg/L due to the presence of various competing ions in the groundwater.

Table 10: Physicochemical parameters of groundwater samples, before and after treated with nHAST adsorbent

Sample	**Water Sample-1**		**Water Sample-2**	
Parameters	Untreated	Treated	Untreated	Treated
Fluoride, mg/L	7.2	1.2	8.2	1.4
Chloride, mg/L	24.1	8.1	19.5	7.9
Sulphate, mg/L	72.0	48.0	76.0	49.0
pH	8.3	8.1	8.3	8.1

The defluoridation capacity of sample 1 and 2 was found to be 0.6 and 0.68 mg F^-/g, respectively, falls well within the trend of nHAST as a function of the fluoride initial concentration (refer to Figure 36). This probably indicates the efficiency of nHAST adsorbent for defluoridation in a real case as well.

4.6.7. Optimized synthesis procedure and reproducibility test

Reproducibility of optimized best synthesis procedural parameters for the preparation of nHAST composite was successfully tested in other similar natural zeolites, labeled Z2, Z4-Z9 collected from different parts of the country by the School of Earth Sciences, AAU.

4.6.7.1. Zeolite samples characterization

All zeolite samples, Z2, Z4-Z9 involved in the preparation of nHA/zeolite composites were first studied by XRD in order to identify the zeolitic structure (Figure 44), followed by ICP elemental analysis in order to verify their similarity in chemical composition with the STI sample under study (Table 11).

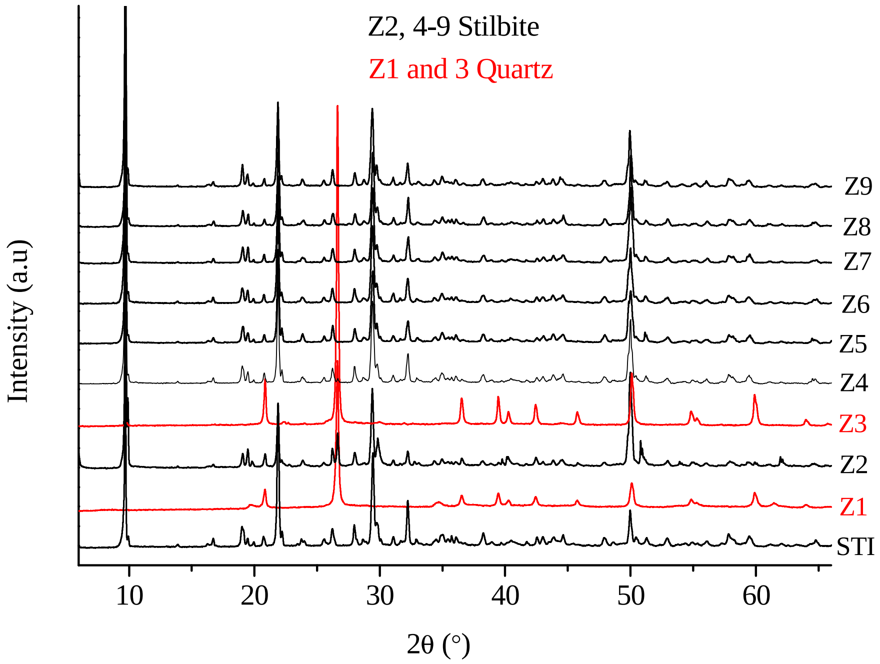

Figure 44: XRD patterns of zeolite samples

As demonstrated in Figure 44, the X-ray diffraction profiles of samples Z2, Z4-Z8 correspond to stilbite natural zeolite [99], while the remaining two samples, Z1 and Z3 were identified as quartz. As clearly shown in the figure, all zeolites identified as stilbite minerals, STI under investigation have very similar diffraction patterns. Those zeolite samples identified as stilbite group minerals were further studied by ICP chemical analysis in order to check the suitability for the composites, nHA/zeolite preparation. With ICP analysis, zeolite samples with high Ca content (to be used as a Ca source/reagent) can be identified as eligible candidates for the preparation of the composites.

The ICP elemental analysis results of zeolite samples that include the most abundant extra framework (Na, Ca) and framework (Si, Al) elements are presented in Table 11. Interestingly, all zeolite samples, Z2, Z4-Z9 including STI under investigation have comparably high Ca composition. However, sample Z2 shows significant differences in Si/Al ratio, another important factor that determine the reactivity. As shown in the figure, Si/Al ratio of Z2 is found to be 5.13, higher than other zeolite samples (Z4-Z9 and STI) having Si/Al ratio in the range of 3.2 to 3.5 (Table 11).

Table 11: ICP elemental analysis of Zeolite samples

Samples	**Al** wt %	**Si** wt %	**Si/Al**	**Na** wt %	**Mg** wt %	**Ca** wt %	**P** wt %
Z2	6.21	31.85	5.13	0.34	0.64	4.49	0.00
Z4	7.67	26.28	3.43	0.47	0.00	5.29	0.00
Z5	7.84	26.35	3.36	0.44	0.00	5.46	0.00
Z6	7.58	25.25	3.33	0.41	0.00	5.24	0.00
Z7	7.43	24.65	3.32	0.40	0.18	5.11	0.00
Z8	7.65	25.64	3.35	0.39	0.00	5.49	0.00
Z9	7.39	25.93	3.51	0.15	0.20	5.27	0.00
STI	8.00	20.40	3.39	0.50	0.16	4.90	0.00

Based on this fact, zeolite samples having similar chemical composition, particularly in Ca content and Si/Al ratio with stilbite sample under investigation, that is, Z4 to Z9 samples were thus chosen for the synthesis procedure reproducibility test of nHAST composite preparation.

4.6.7.2. nHA/Zeolite composite samples characterization result

For Z4-Z9 zeolite samples, the corresponding nHA/Z4-9 composites were synthesized at the best optimum synthesis procedure of synthesis time of 2 hours, crystallization pH 8, crystallization time of 144 hours and room temperature conditions. The composites were first characterized, and then tested in fluoride removal, and finally their performances were compared with the nHAST composite under investigation. Figure 45 presents the X-ray diffraction patterns of the synthesized nHA/Z4-9 composite samples. As shown in the figure, all of them, including nHAST under study showed very similar diffraction pattern.

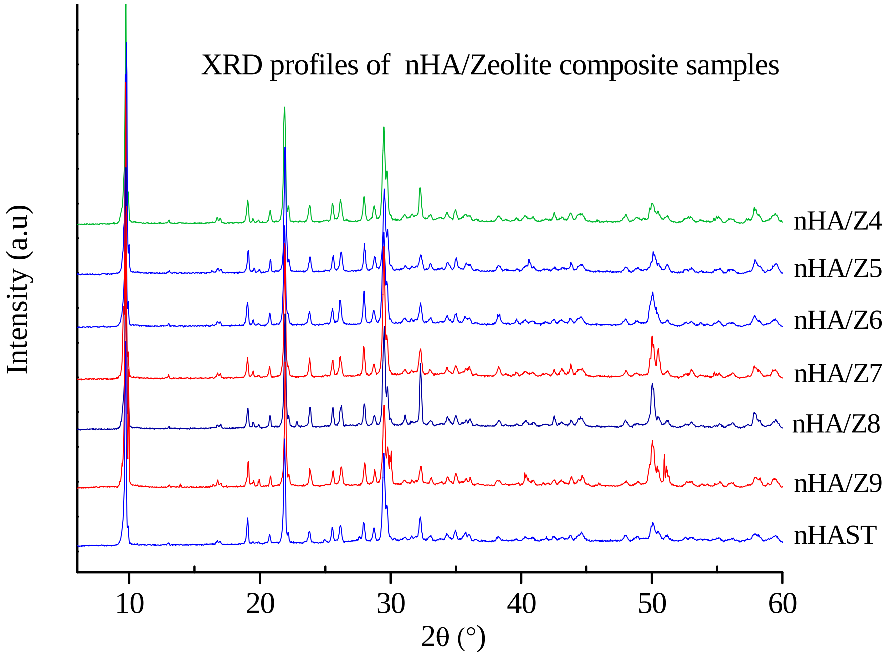

Figure 45: XRD patterns of nHA/zeolite composite samples synthesized at best optimized synthesis procedure for nHAST composite

The peaks at 2θ angles of 9.70, 18.98, 21.91, 26.13, 28.05, 29.45, 32.15 and 50.01 degrees displayed characteristic peaks identical to those of the support stilbite mineral [96]. This suggests that the crystalline structure of all the support zeolites did not change after the HAp grown on zeolite surface, which show their stability under synthesis conditions. However, same as the nHAST composite under investigation, the identification of the presence of HAp in all nHA/Z4-9 composites by XRD were not possible, again because of the low concentration of HAp in the composite, the small (nanometric) crystal size and the overlapping with the more abundant and intense zeolite diffractions. Similar to the case in nHAST, the presence of HAp can easily be confirmed by the presence of P in the final composites by ICP elemental analysis as identified in Table 12. Again, the amount HAp (quantified by the content of P by ICP) growth on zeolite surfaces was found low, in the range between 5.4 % in nHA/Z9 to 10.8 % in nHA/Z4 and nHA/Z5. This and other similarities in Ca content and Si/Al ratio of the final composites with respect to nHAST, indicate the reproducibility of the synthesis procedure well.

Table 12: ICP elemental analysis of nHAZ4-nHAZ9 composite samples synthesized at the optimized synthesis procedure

Samples	**Al** wt %	**Si** wt %	**Si/Al**	**Na** wt %	**Ca** wt %	**P** wt %	**HAp** %
nHAZ4	7.24	20.24	2.80	0.08	5.09	2.00	10.80
nHAZ5	7.27	20.58	2.83	0.12	5.13	2.00	10.80
nHAZ6	7.58	21.82	2.88	0.10	5.22	1.20	6.50
nHAZ7	7.24	20.72	2.86	0.11	4.92	1.90	10.30
nHAZ8	7.29	21.35	2.93	0.10	5.16	1.10	5.80
nHAZ9	7.08	21.03	2.97	0.05	5.14	1.00	5.40
nHAST	8.00	20.04	2.55	0.20	5.30	1.70	9.20

4.6.7.3. Defluoridation test results

Fluoride removal performance of nHA/zeolite composites including their support zeolite samples were tested in batch adsorption experiments. Defluoridation test was performed using 10 mg/L initial fluoride concentration at 100 and 10 g/L dose of raw zeolites, and nHA/zeolite composites, respectively, as presented in Figure 46. As shown in the figure, the fluoride removal efficiency of nHA/zeolite composites was significantly high, indicating the formation of higher amount of active nHA sites on zeolite surface (as evidenced by ICP, wt % of HAp in Table 12).

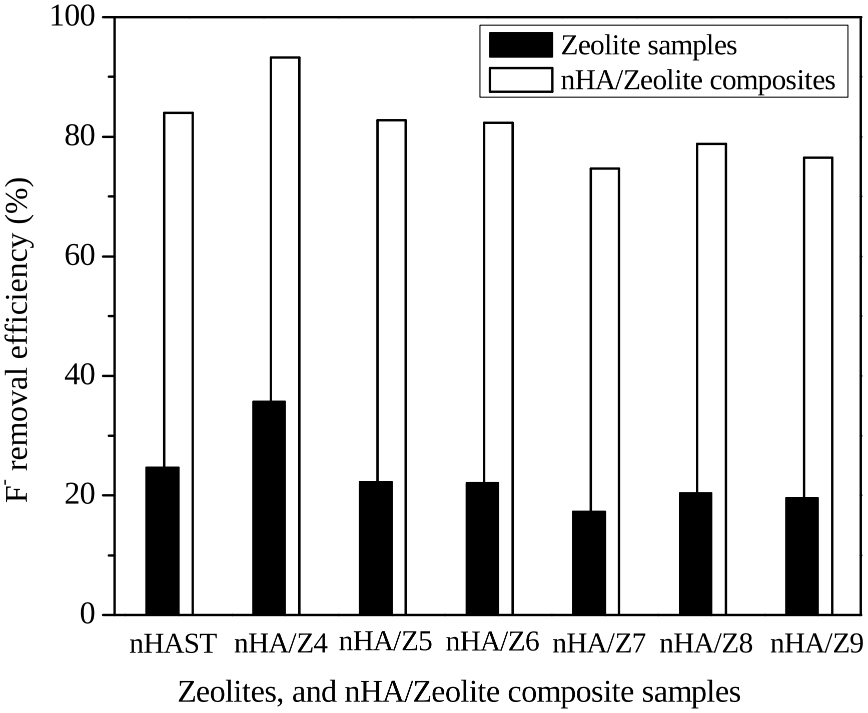

Figure 46: Fluoride removal efficiency of natural zeolites (Z4-Z9, STI) (black bar) and the corresponding nHA/Zeolite composites (white bar)

As identified in Figure 45 all the support zeolites show very low performance, less than 30 % fluoride removal from 10 mg/L initial fluoride concentration at a dose of 100 g/L. However, significantly high fluoride removal efficiency was recorded for the composites at the same initial fluoride concentration of 10 mg/L and at 10 g/L, ten times lower dose. Maximum fluoride removal of 93 % was recorded in nHA/Z4, whereas the minimum 75 % removal in nHA/Z7 composite. Interestingly, all the composites are able to reduce the fluoride concentration below or at least closest to WHO maximum limit of 1.5 mg/L from initial fluoride concentration of 10 mg/L.

The fluoride removal capacities of nHA/zeolite composites are comparable, being between 0.75 and 0.93 mg F^-/g at 10 mg/L initial fluoride concentration and at 10 g/L adsorbent dose, for nHA/Z7 and nHA/Z4 composites, respectively. However, if we normalize the fluoride removal capacity to the amount of HAp present in each adsorbent (determined from ICP and equation 3, Table 12), to give the corresponding HAp intrinsic capacity, calculated as mg F^- per gram of HAp, we observe a slightly larger difference. In this case higher fluoride removal capacity of 14.17 mg F^-/g HAp for the HA in nHA/Z9 composite, almost twice that of nHA/Z7 composite with the lowest HAp intrinsic capacity of 7.25 mg F^-/g HAp, was found. This is still one of the highest values found in the literature for HAp, suggesting that the HAp particles grown on the zeolite surface of the composite samples are much more efficient in removing fluoride, most probably due to their small particle size and high dispersion nature. This agrees very well with the findings of nHAST composite for which the synthesis procedures have been optimized and tested. Thus, the overall study results indicate the credibility of the proposed low energy demanding synthesis procedure, which can be reproduced with different stilbite zeolite samples.

4.7. Scale-up of nHAST composite synthesis

This study aims to optimize the use of reagents at laboratory scale as well as scale up the synthesis of about 2 g nHAST composite to 250 g of the best optimized synthesis procedure, that is nHAST synthesized at synthesis time of 2 hours, crystallization pH 8, crystallization time of 144 hours and room temperature conditions. The aim is to utilize the recovered ammonium phosphate (AP) filtrates upon treatment of each raw zeolite, which otherwise are thrown as a waste material. The process implies that the ammonium phosphate $(NH_4)_2HPO_4$ original solution (AP-0), used in synthesizing the first nHAST-0 composite, will be reused in a second synthesis (nHAST-1) and so on. Scheme 2 demonstrates a simplified scaling up synthesis process of nHAST composite.

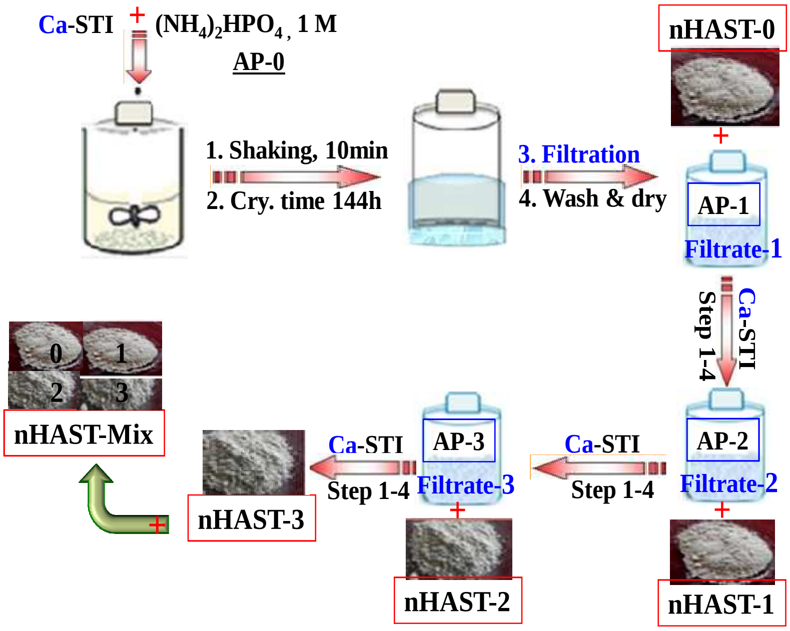

Scheme 2: Scaling up synthesis process illustration of nHAST-0, nHAST-1, nHAST-2 and nHAST-3 composites using the recovered filtrates (APs)

As clearly observed, in addition to the initial nHAST-0 composite synthesized from ammonium phosphate ($(NH_4)_2HPO_4$) original solution and stilbite zeolite, three differentiated nHAST composite samples namely nHAST-1, nHAST-2, and nHAST-3 were synthesized from consecutively recovered ammonium phosphate filtrate solutions: AP-1(Filtrate 1), AP-2 (Filtrate-2), and AP-3 (Filtrate-3), respectively in the synthesis process and the support STI zeolites. Finally, in searching for the possibility of using all composites in one, we mixed all composite adsorbents: nHAST-0, nHAST-1, nHAST-2 and nHAST-3 together to form one, labeled nHAST-Mix composite with the overall amount of about 910 g, almost four times the initially intended amount of 250 g due to nHAST-0 composite alone.

4.7.1. ICP elemental analysis result

ICP elemental analysis was carried out for all nHAST composite samples, nHAST-0, nHAST-1, nHAST-2, and nHAST-3synthesized during scale-up synthesis at slightly different crystallization pHs. The result of measurement of elemental composition and % HAp calculated based on P content are summarized in Table 13.

Table 13: ICP elemental analysis of nHAST-0, nHAST-1, nHAST-2, and nHAST-3samples synthesized in scale-up at slightly different crystallization pH

Samples	**Crys.** pH	**Al** %wt	**Si** %wt	**Ca** %wt	**K** %wt	**Na** %wt	**P** %wt	**HAp** %
nHAST-0	7.96	7.5	18.2	5.3	0.4	0.2	2.1	11.34
nHAST-1	7.81	7.8	18.8	5.7	0.3	0.3	2.1	11.34
nHAST-2	7.65	7.8	18.9	5.6	0.3	0.2	2.1	11.34
nHAST-3	7.51	7.0	17.0	5.1	0.3	0.2	2.0	10.80

As shown in Table 13, the ICP analysis detected the presence of significant and comparable quantity of Ca^{2+} ions in all nHAST composite samples, irrespective of ammonium phosphate solutions. As shown in the table, the pH of crystallization of nHAST-0 was about 8, whereas in the consecutive syntheses the crystallization pH slowly decreases until it attained at minimum of 7.51 in nHAST-3. This is possibly the result of the slight change in chemical compositions of the corresponding filtrate solutions used in the synthesis. Because the change in crystallization pH from the expected pH of 8 is insignificant, in all cases the composite synthesis was conducted without the addition of bases for pH adjustment. Similar to Ca composition, ICP also detected constant amount of P in the composites, and thus the constant amount of HAp has grown on stilbite surface, irrespective of crystallization pH media.

4.7.2. Thermogravimetric analysis

Thermogravimetric analysis was carried out on all nHAST samples synthesized in scale-up processes. The thermogravimetric analysis result presented in Figure 47 shows TGA-DTG curves of the support STI and nHAST composite samples. The TGA plot shows three overlapping regions of weight losses. It is clearly seen from the figure that in low temperature region alone, two differentiated weight losses can be observed in both the STI sample and the nHAST composite samples. In STI, the first weight loss at temperatures below 130 ºC is assigned to loosely attached water. The second strong weight loss with maximum desorption rate at around 170 ºC and other of a lower desorption rate at about 260 ºC are due to desorption of strongly retained water molecules within the STI framework by coordination with exchangeable Ca^{2+} ions.

As can be observed in the figure there is a significant difference in the early weight losses of nHAST samples as compared to the original support STI zeolite. This is because the thermal curves are influenced by the dominant cation present in the composites. Besides, a slight shift of weight loss for dehydration to the lower temperature was observed in TGA-DGT curves of nHAST samples. This is possibly because of the weaker interaction of water molecules with the dominant monovalent NH_4^+ ions exchanged for Ca^{2+} ions in nHAST samples as compared to stronger interaction with divalent Ca^{2+} ions in the parent STI. In all cases, the maximum water desorption shift is observed at about 150 ºC due to loss of weakly adsorbed moisture and interlayer free water molecules. Similar scenario was also observed in another water desorption band of lower weight loss, again due to structural water molecules bound to interlayer cations. In this case, the maximum weight losses were observed at about 210 ºC.

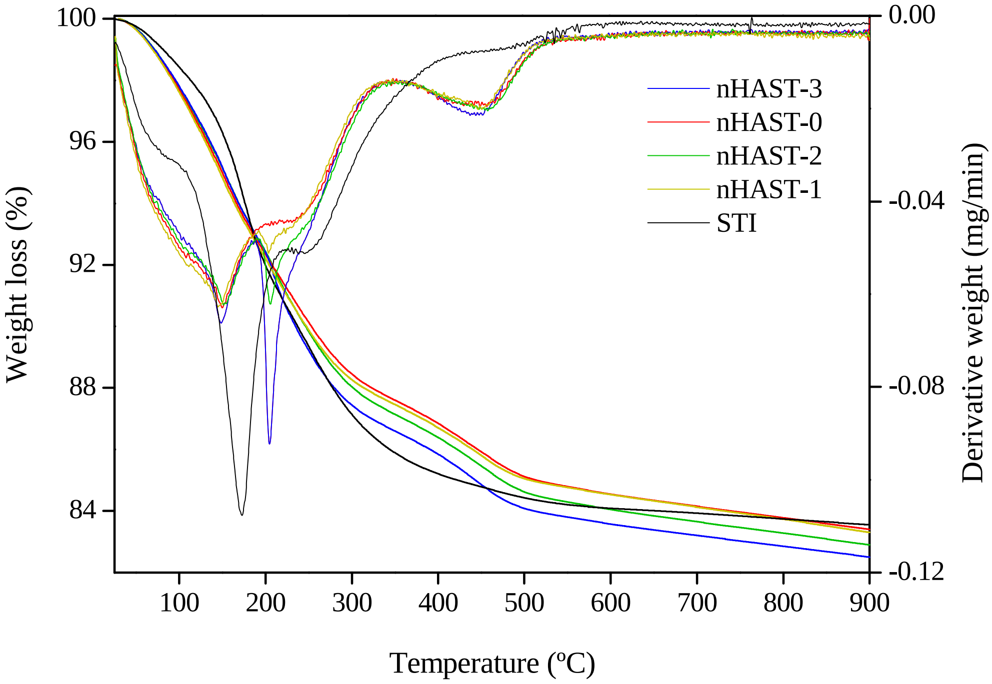

Figure 47: TGA and DTG curves of STI and nHAST composite samples

Interestingly, in the high temperature case (210 ºC) water desorption intensity increases significantly with the stage of recovered filtrates used in the synthesis (nHAST-0 < nHAST-1 < nHAST-2 < nHAST-3), suggesting more exchange of Ca^{2+} by NH_4^+ ions in the respective order. Furthermore, desorption of water at temperatures below 150 ºC is much more intense, while desorption of strongly bonded coordinated water molecules at higher temperature, 210 ºC is much smaller. Again this is a consequence of the exchange of more amount of Ca^{2+} by NH_4^+ ions, which weakly coordinate water molecules, and hence the major water desorption occurs at low temperature. Besides, in nHAST composite samples additional new broad peak was arose at around 460 ºC due to the elimination of ammonia, indicating the release of NH_3 as NH_4-STI transforms into H-STI [82, 144].

4.7.3. Point of zero charge determination

Potentiometric mass titration technique was used for determination of the point of zero charge, PZC of nHAST-0, nHAST-1, nHAST-2, nHAST-3 and nHAST-Mix composite samples. Figure 48 shows the pH of PZC of nHAST-0 composite, the first synthesized sample in scale-up synthesis process (Scheme 2). As described in the figure, the PZC of nHAST-0 composite is found high, at about 10, as identified by the common intersection point of the potentiometric curve of the blank solution with the corresponding curves of the composite material containing 0.5, 1.0, and 1.5 g in 0.02 N $NaNO_3$ electrolytic solutions. This shows the drastic change in the surface morphology of nHAST-0 composite as compared to the parent STI zeolite with very low PZC, about 2.1 (refer to Figure 32). The significant portion of the composite surface (below pH 10.0) is therefore positively charged, suggesting its favorability in fluoride removal through electrostatic attraction.

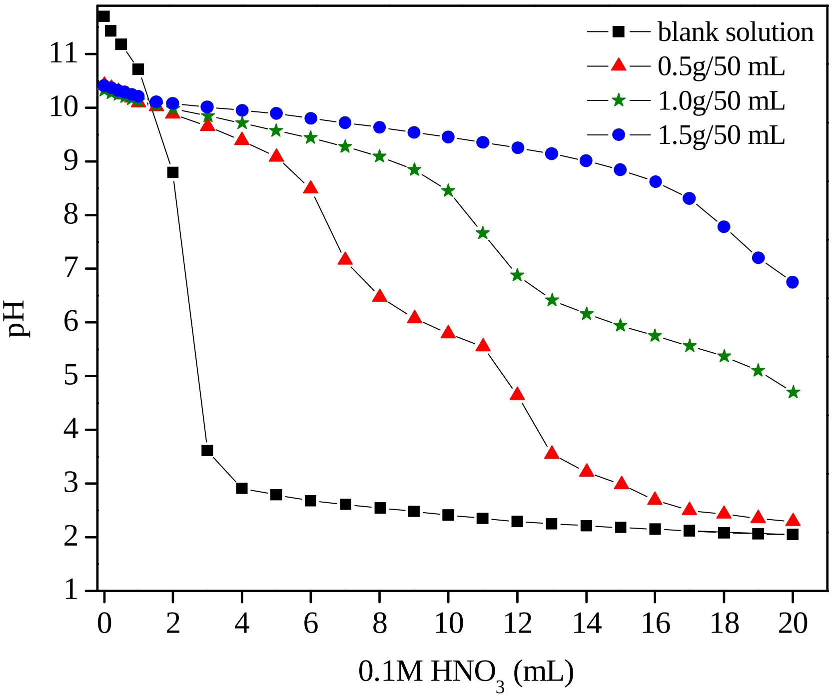

Figure 48: Experimental curves corresponding to the potentiometric mass titrations technique for the determination of the PZC of nHAST-0

The PZCs in the case of other composites synthesized using filtrate solutions: nHAST-1, nHAST-2 and nHAST-3 are found even higher, 10.5, 11.15 and 11.3, in the respective order (refer to Appendix 1). It show slight shift toward higher pH values with the stage of filtrate solutions used in the preparation. As clearly observed in Figure 49, the PZC for nHAST-Mix, most significant composite from practical point of view, is found to be 11.15, even greater than that of nHAST-0 (Figure 48), indicating more pronounced adsorption onto the larger positively charged portion of nHAST-Mix surface, below its PZC of 11.15, than onto the nHAST-0, below PZC of 10.

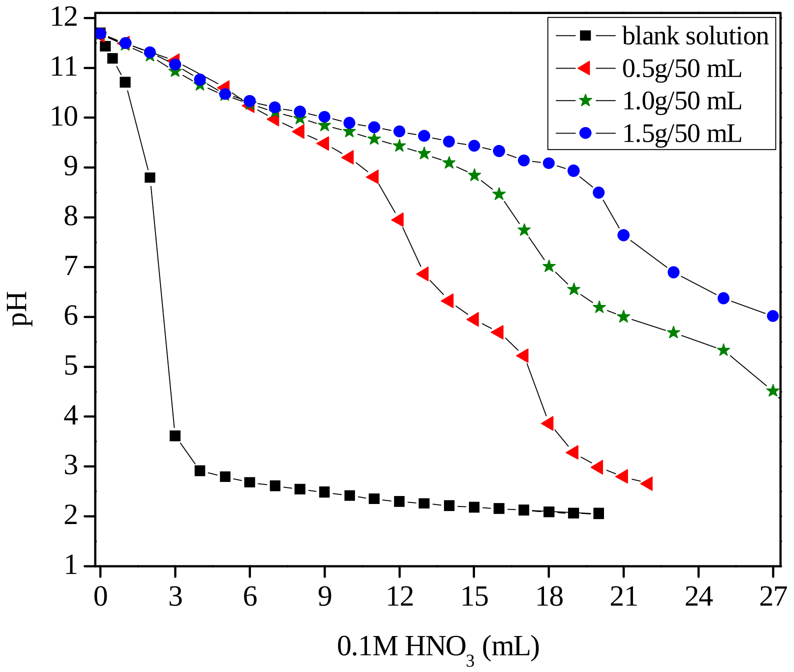

Figure 49: Experimental curves corresponding to the potentiometric mass titrations technique for the determination of the PZC of nHAST-Mix composite

4.7.4. Defluoridation test results

The performance of all composite samples: nHAST-0, nHAST-1, nHAST-2, nHAST-3 and nHAST-Mix were tested in fluoride removal and the results are described in Figure 50 for two different initial fluoride concentrations, 5 and 10 mg/L. As clearly observed, all composites performs very well in fluoride removal. Interestingly, composites synthesized using recovered filtrate solutions show higher defluoridation performance that increase with the stage of the filtrate solutions. This finding is very well supported by point of zero charge studies.

The more pronounced fluoride removal adsorption recorded for nHAST-3, 98.4 %, significantly higher than nHAST-0 sample with 82.1 % fluoride removal efficiency at 10 mg/L initial fluoride concentration at 10 g/L adorbent dose, yielding the final residual fluoride concentrations of 0.16 and 1.79 mg/L, respectively. At the same adsorbent dose if the initial fluoride concentration is 5 mg/L, the performance of the nHAST-0 and nHAST-3 composites reached around 92.2 % and 99.3 % fluoride removal. In this case, the final residual fluoride concentrations were found to be 0.04 and 0.39 mg/L, respectively. As compared to nHAST-3, nHAST-Mix sample show slight decreases in fluoride removal due to the surface charge effect. nHAST-Mix has lower PZC, 11.15 and thus lower in the surface positive charge as compared the higher PZC, 11.3 of nHAST-3. Defluoridation performance of nHAST-Mix composite at 10 and 5 mg/L initial fluoride concentrations, are still higher than the nHAST-0 sample, 94.1 and 98.3 % at 10 g/L adsorbent dose, yielding the final fluoride concentrations of 0.59 and 0.09 mg/L, respectively. In both cases the WHO standard for drinking water are met very well.

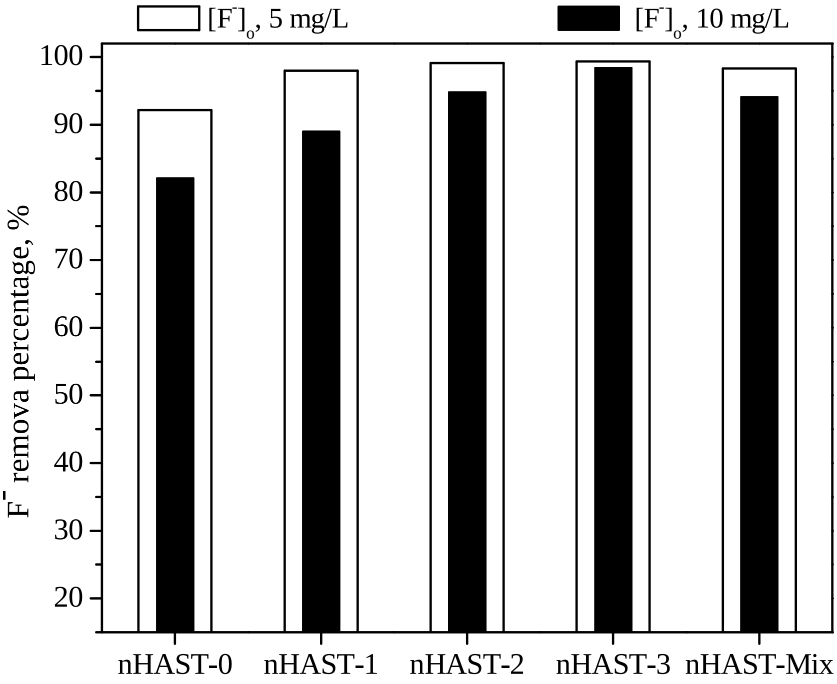

Figure 50: Fluoride removal efficiency (%) of nHAST composite samples (dose = 10 g/L)

From the practical point of view, the high defluoridation capacity of the final nHAST-Mix composite with an efficient use of the starting reagents, where no waste is generated even at larger scale production makes nHAST composite the promising defluoridation adsorbent.

4.8. Comparison of nHAST composite with Bone Char

In this section we compare our composite performance with Bone charcoal (BC), a defluoridation technology already implemented in the Rift Valley of Ethiopia. The nHAST and BC samples were first characterized using X-ray diffraction, ICP-chemical composition analysis, TGA, IR-ATR and NMR techniques. Following, their performance in fluoride removal was compared. A mechanism involving fluoride adsorption is also proposed based on kinetics and isotherm studies. In kinetic study, the two commonly used models: pseudo-first order and pseudo-second order were used in order to investigate the controlling reaction mechanism of the adsorption process. Adsorption isotherm was studied to investigate the information on how adsorption system takes place and how efficiently our adsorbents interact with fluoride ions including their mechanism of interaction at constant temperature.

4.8.1. X-ray diffraction analysis result

X-ray diffraction was used to determine whether the STI framework underwent any transformation during the preparation process. The XRD pattern (Figure 51) of the synthesized nHAST composite samples (blue line) and the parent STI zeolite (red line) are very similar, evidencing the resistance of the STI framework [99]. However, slight variations are observed in the region between 2θ angles of 23 and 24 degree, where the initial stilbite mineral showed three clearly distinguishable peaks characteristic of a monoclinic stilbite, while the nHAST composite showed a single diffraction (marked by an asterisk), evidencing a change of the space group to orthorhombic; this is caused by the almost-complete exchange of Ca^{2+} and Na^{+} of the original stilbite by NH_4^+ ions during the preparation of the composite.

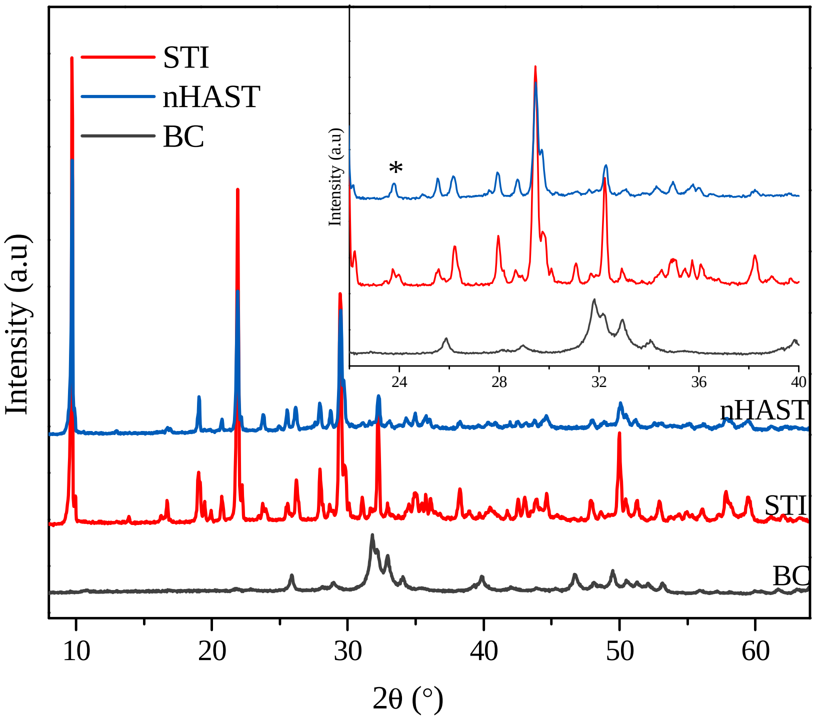

Figure 51: XRD profiles of the support STI, nHAST composite and BC samples

The identification of the presence of HAp by XRD was not possible in the case of the nHAST composite, because of the low concentration of HAp in the composite, its small (nanometric) crystal size and the overlapping with the more abundant and intense zeolite diffractions. As shown in Figure 51, the profile of the Bone Char identifies the presence of HAp structure despite the calcinations of the bones. The peaks at 2θ angles of 25.9, 29.0, 31.8, 32.1, 32.9, 34.1, 39.9, 46.7 and 49.5 degrees in XRD pattern of BC match perfectly that of HAp (Hydroxyapatite, syn, $Ca_5(PO_4)_3(OH)$, ICDD - PDF2 card 00-009-0432).

However, the formation of HAp on the STI surface can be easily assured by the presence of P in nHAST material, by ICP elemental analysis (Table 14) from which the content of HAp, ($Ca_5(PO_4)_3OH$) (in weight %), in the material is calculated from the content in P obtained from the ICP (weight % P), according to equation 11 in section 2.3.

Table 14: ICP elemental analysis of a support STI, nHAST composite and BC

Samples	**Element (wt %)**					**HAp**
	Al	Si	Na	Ca	P	wt %
STI	8.0	20.4	0.5	4.9	-	-
nHAST	7.5	18.2	0.2	5.3	1.7	9.18
BC	-	-	-	30.2	14.9	80.43
HAp (theoretical)	-	-	-	39.8	18.5	99.86

4.8.2. Thermogravimetric analysis result

Figure 52 shows TGA-DTG curves of the STI, nHAST, and BC samples. In STI and nHAST samples, a first weight loss at temperatures below 150 ºC is assigned to loosely attached water. In the original STI zeolite, a second strong weight loss, with maximum desorption rates at 175 and 250 ºC, is observed, which is assigned to desorption of strongly-retained water molecules by coordination with exchangeable Ca^{2+} ions. In nHAST, a second weight loss of strongly adsorbed water molecules inside the zeolite structure takes place at around 240 ºC. Desorption of poorly-retained water at temperatures below 150 ºC is much more intense for the STI and nHAST composite samples. Interestingly, desorption of strongly retained coordinated water molecules at higher temperatures is much smaller in the case of nHAST. This is a consequence of the exchange of Ca^{2+} by NH_4^+ ions, which do not coordinate water molecules, and hence the major water desorption occurs at low temperature. In the nHAST composite, an additional broad peak is observed at around 460 ºC, which is attributed to deammoniation, indicating the release of NH_3 as NH_4-STI transforms into H-STI [82, 146]. In the BC sample, a slow release of water molecules is observed at low temperature (up to 200 ºC), followed by a continuous weight loss between 300 and 700 ºC which must be due to release of water after desorption or through dehydroxylation processes and/or desorption of organic matter. A final weight loss with maximum desorption rate at around 820 ºC must correspond to the decomposition and release of the remaining organic matter after calcination.

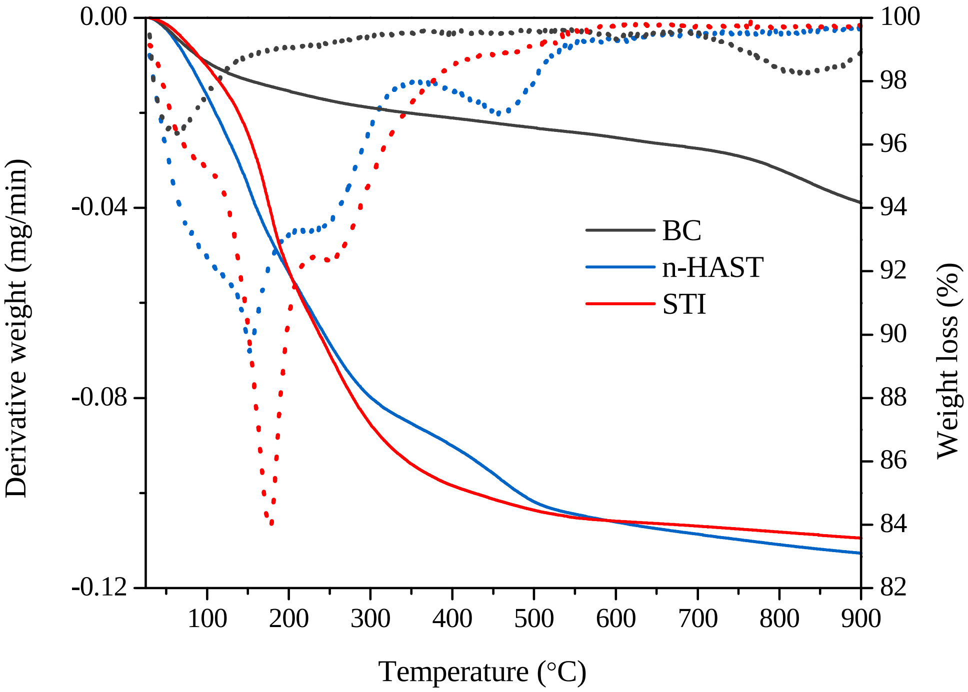

Figure 52: TGA (solid lines) and DTG (dashed lines) of the STI, nHAST and BC samples

4.8.3. IR-ATR analysis results

Figure 53 shows IR-ATR spectra of (a) as synthesized nHAST composite, (b) the original zeolite (STI), and (c) BC. In the original STI zeolite (Figure 53b), the band at 1630 cm^{-1} can be assigned to the deformation band of adsorbed water. The external and internal T-O asymmetric stretching vibrations appear at 1145 and 994 cm^{-1}, respectively, while bands at 790 and 701 cm^{-1} are assigned to the symmetric stretching vibrations. The band at 560 cm^{-1} arises from double ring vibrations, and that at 430 cm^{-1} comes from T-O bending [144, 145]. BC sample (Figure 53c) showed the characteristic pattern of hydroxyapatite, with strong bands at 1090, 1025, and 962 cm^{-1} assigned to the stretching and bending modes of PO_4^{3-} groups, and at 600 and 563 cm^{-1} corresponding to bending of PO_4^{3-} that also match with other literature values [113, 125]. The vibrational mode of OH^- is observed at 630 cm^{-1}. Additional bands are observed at 872, 1420 and around 1470 cm^{-1}, which are consistent with the presence of CO_3^{2-} anions, suggesting a partial substitution of PO_4^{3-} by CO_3^{2-} in the apatite structure [125].

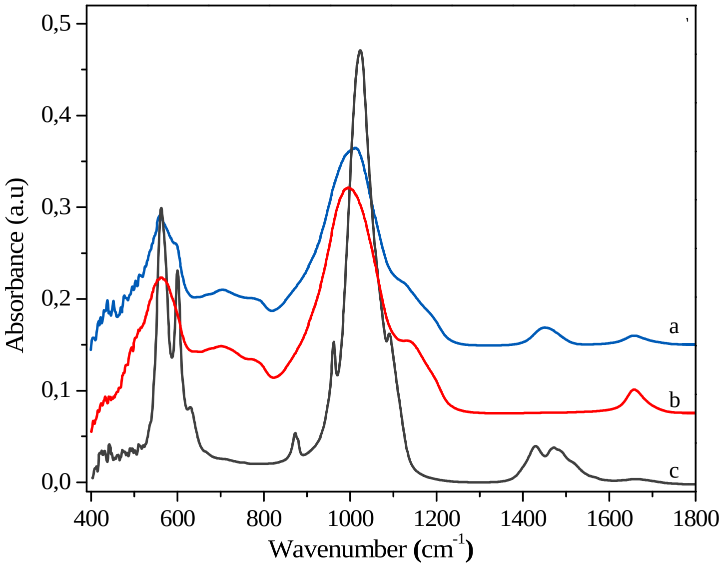

Figure 53: IR-ATR spectra of a) nHAST composite b) STI zeolite, and c) BC

Finally, a broad low intense band observed at 1650 cm^{-1} indicates adsorbed H_2O in the sample. After the chemical treatment of STI to produce the nHAST composite (Figure 53a), the main bands due to the STI framework remained, and a new band arose at about 1430 cm^{-1} due to the presence of NH_4^+ ions after the ion-exchange process during the HAp crystallization. This indicates that the chemical treatment caused the cation exchange of Ca^{2+} by NH_4^+, and agrees well with the ICP and TGA results [146]. Additionally, new features in the double ring vibration band of the STI framework at around 560 cm^{-1} showed up at about 565, 606 and 1020 cm^{-1}, which are consistent with the presence of PO_4^{3-} groups [143], again suggesting the crystallization of HAp on the nHAST composite.

4.8.4. ^{31}P MAS-NMR analysis result

^{31}P MAS-NMR was then used to confirm the presence of HAp in the nHAST composite and BC. Figure 54 shows resonances at around 2.85 ppm and 2.80 ppm for nHAST and BC, respectively, characteristic of P in HAp [125, 148]. However, some differences in the shape of the bands are observed: the band corresponding to nHAST material is broader and developed a shoulder at around 0 ppm, which has been assigned to a nanometric nature of HAp crystals [98, 146, 149]. The difference between both NMR spectra suggests a smaller crystal size and more defective structure of HAp on the nHAST composite than on BC.

Once the formation of HAp on the composite is confirmed, the amount of HAp crystallized was determined by measuring the P content in the nHAST material by ICP elemental analysis (Table 14). According to this, about 9.2 wt % of HAp crystallized on the surface of the composite, while BC showed a higher amount of HAp of about 80.4 % (estimated assuming a stoichiometric composition. This value becomes 76 % if we use the Ca content). The Ca/P molar ratio in BC is 1.57, slightly lower to the nominal value of 1.67, as commonly observed for biogenic HAp. Such calculation cannot be done for the nHAST composite since in this case Ca comes not only from HAp but also can remain in the zeolite (due to a potential incomplete Ca-NH_4 exchange).

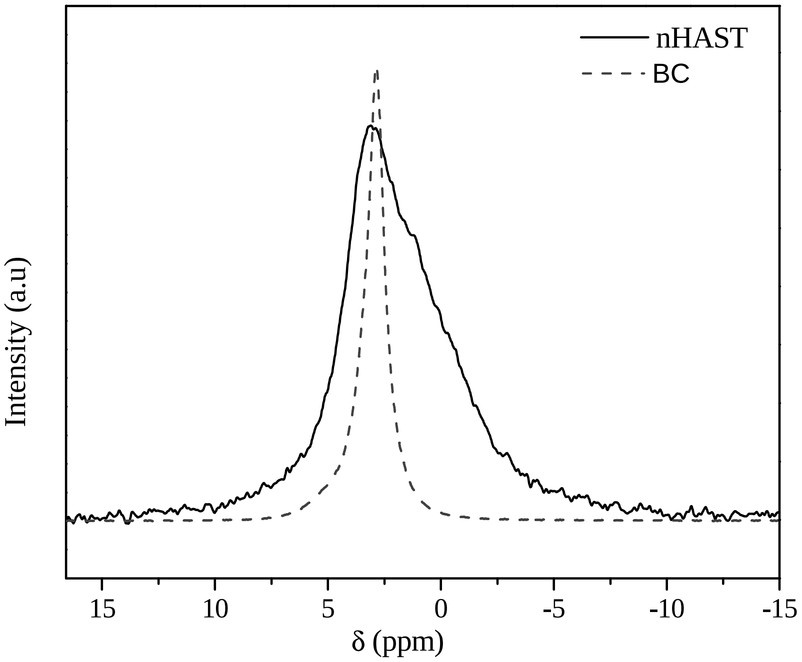

Figure 54: ^{31}P MAS NMR spectra of the nHAST composite and BC samples

SEM micrographs are included in Figure 55a shows the original STI zeolite before modification. Figure 55b shows the nHAST composite in which the nanometric size of HAp grown on the surface of the stilbite crystals cannot be observed clearly at the magnification exhibited in the micrographs. However, some irregularities developed on the surfaces as compared to the parent support STI zeolite can be observed. Finally, Figure 55c shows a typical particle forming the bone char with no particular surface features.

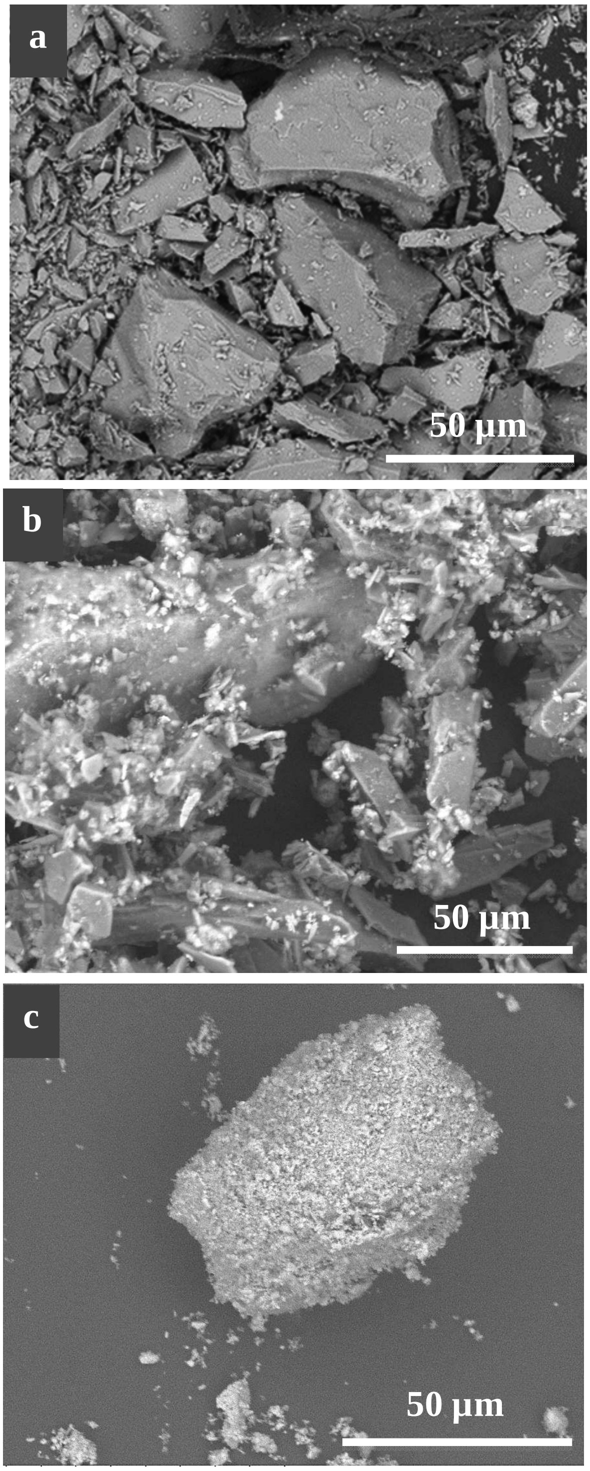

Figure 55: SEM micrographs of a) STI, b) nHAST composite, and c) BC

4.8.5. Fluoride removal results and adsorption mechanisms

Adsorption experiments were initially performed for nHAST composite and BC using various doses (4, 6, 8, 10 and 12 g/L) at initial fluoride concentration of 10 mg/L and a contact time of 20 hours with continuous agitation and at room temperature, Figure 56. As expected, the fluoride removal efficiency was significantly increased at higher adsorbent doses, and reached about 84.0 and 86.7 % of fluoride elimination at a dose of 10 g/L for nHAST and BC adsorbents, respectively. This is due to a higher surface area and the availability of more adsorption sites at higher adsorbent dosage. Both materials are able to reduce the fluoride concentration below the WHO limit of 1.5 mg/L.

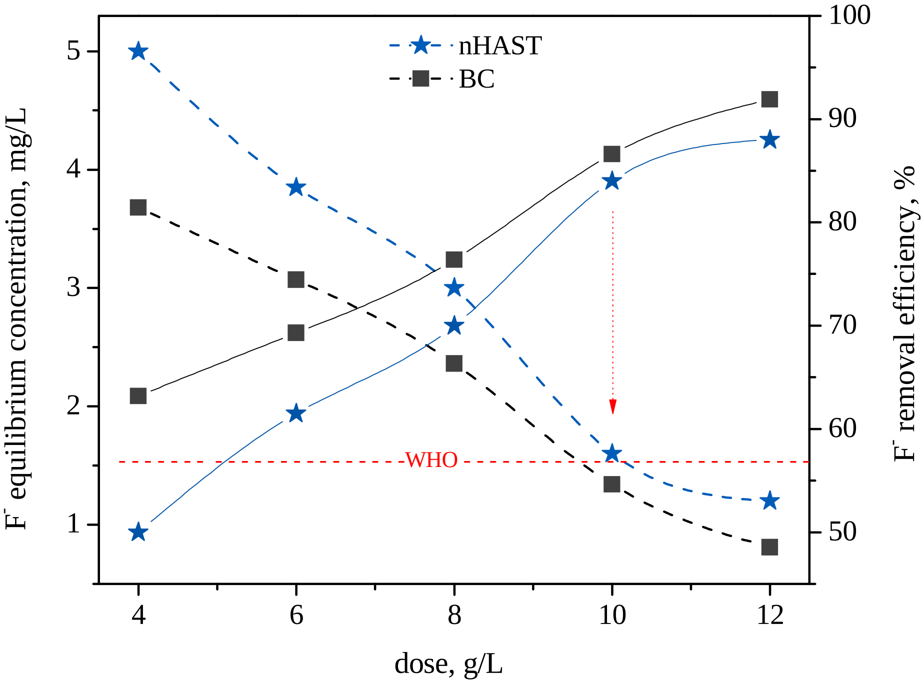

Figure 56: Fluoride equilibrium concentration (dashed lines) and removal efficiency (solid lines) of nHAST composite and BC as a function of dose

The fluoride removal capacity at a dose of 10 g/L is also comparable for the two adsorbents, being 0.84 and 0.87 mg F^-/g for nHAST and BC, respectively. A slightly larger difference is observed at the low dose of 4 g/L, where higher capacities of 1.25 and 1.58 mg F^-/g are observed for nHAST and BC, respectively. As there is no significant change on the efficiency beyond this as well as the measured final equilibrium fluoride concentration has reached the WHO maximum permissible level, a dose of 10 g/L was considered as an optimum dose for further adsorption experiments.

4.8.6. Experimental results on kinetic studies

In order to identify the dynamics of the adsorption process, kinetics experiments were carried out for nHAST and BC at different contact times (0.5, 1, 2, 8, 16, 20, 24 and 28 hours) using an adsorbent dose of 10 g/L and initial fluoride concentration of 10 mg/L at room temperature. The study showed a rapid removal of fluoride ions in the first 8 hours followed by a subsequent slow removal until 20 hours, where equilibrium is reached with 84.0 % and 86.7 % of fluoride removal efficiencies for nHAST and BC, respectively, Figure 57. The slow adsorption stage at long contact times is probably the result of a slow uptake of fluoride and diffusion to the inner adsorbent surface. Since there is no significant increase of fluoride adsorption beyond this point, an adsorption time of 20 hours was fixed for further experiments.

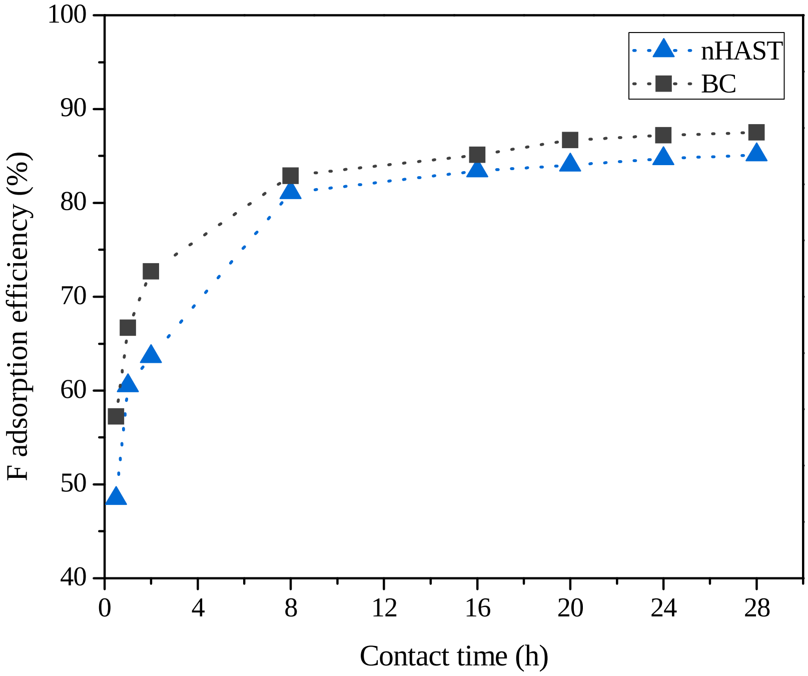

Figure 57: Fluoride adsorption kinetics on nHAST and BC composite samples at initial fluoride concentration of 10 mg/L and dose of 10 g/L

In the present study the two most commonly used kinetic models, that is pseudo-first order and pseudo-second order reaction mechanisms were applied. The experimental data used for fluoride adsorption kinetics of nHAST and BC were analyzed using eq. 8 and 9 described in section 2.3, as presented in Table 15.

Table 15: Data for fluoride adsorption kinetics of nHAST and BC, at 10g/L dose and 10 mg/L initial fluoride concentration

t, h	**Kinetics of nHAST**			**Kinetics of BC**		
	C_e, mg/L	Eff, %	Q_e,mg/g	C_e, mg/L	Eff, %	Q_e,mg/g
0.5	5.15	48.5	0.485	4.28	57.2	0.572
1	3.97	60.5	0.605	3.33	66.7	0.667
2	3.64	63.6	0.636	2.73	72.7	0.727
8	1.89	81.1	0.811	1.71	82.9	0.829
16	1.66	83.4	0.834	1.49	85.1	0.851
20	1.60	84.0	0.840	1.33	86.7	0.867
24	1.53	84.7	0.847	1.28	87.2	0.872
28	1.48	85.1	0.851	1.25	87.5	0.875

The pertinence of the two models was developed by constructing linear plot of log (Q_e - Q_t) against t for pseudo-first order model (Figure 58a) and t/qt vs. t for pseudo-second order model (Figure 58b); the adsorption rate constants and correlation coefficients are reported in Table 16.

Results clearly show that the pseudo-first order model does not fit well to the adsorption kinetics on the two adsorbents; the correlation coefficients, R^2, were 0.9678 and 0.9699 for nHAST and BC, respectively. The calculated values of capacity at equilibrium, $Q_{e,cal}$, following this model (0.295 and 0.257 mg/g in Table 16) also differed from the experimental Q_e values (0.84 and 0.87 mg/g) for nHAST and BC, respectively, which show that the model is not appropriate to describe the adsorption kinetics.

Table 16: Summary of the Pseudo-first order and Pseudo-second order rate constants and correlation coefficients of nHAST and BC adsorbents

Pseudo-first order			**Pseudo-second order**		
	nHAST	**BC**		**nHAST**	**BC**
K_1	0.177	0.175	K_2	2.206	2.776
$Q_{e,cal}$, mg/g	0.295	0.257	$Q_{e,cal}$, mg/g	0.862	0.885
R^2	0.9678	0.9699	R^2	0.9999	0.9999

In contrast, the adsorption of fluoride on both nHAST and BC adsorbents are best described by a pseudo-second order model (in both cases $R^2 = 0.9999$). In this case, the theoretical equilibrium capacities for the pseudo-second order kinetic model (0.862 and 0.885 mg/g in Table 17) fit nicely with the experimental values (0.84 and 0.87 mg/g) for nHAST and BC, respectively, indicating that this model represents the fluoride adsorption kinetics for both nHAST and BC. The rate constant K_2 is slightly higher for BC (Table 17), indicating a slightly faster adsorption on this adsorbent, as observed in Figure 57.

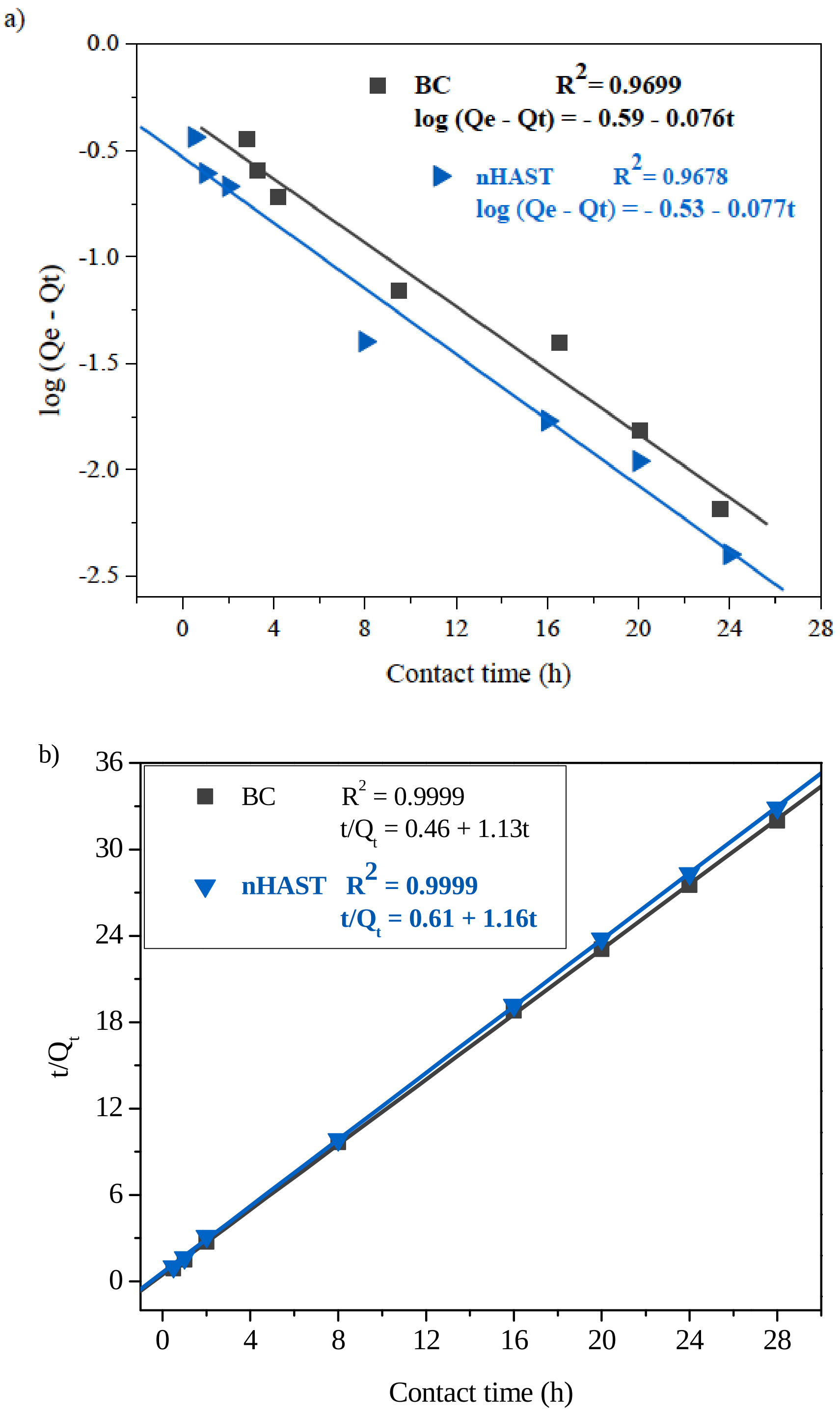

Figure 58: a) Pseudo-first order and b) Pseudo-second order plot of fluoride adsorption kinetics at a dose of 10 g/L and 10 mg/L initial fluoride concentration

Besides, the theoretical equilibrium capacities (0.862 and 0.885 mg/g) for pseudo-second order kinetic model as stated in a summary Table 16 fit well with the experimental value (0.84 and 0.867 mg/g) in Table 15 for nHAST and BC, respectively. This indicates that this model better represents the fluoride adsorption kinetics for both nHAST and BC, and that more of the adsorption might follows second order chemisorptions process.

4.8.7. Experimental result on adsorption isotherm

Adsorption isotherm experiments were carried out in order to determine the best conditions for a maximum fluoride removal by the nHAST and BC adsorbents, using various initial fluoride concentrations (2, 4, 6, 8, 10, 15, 20, 50, 100, and 200 mg/L) and a constant adsorbent dose of 10 g/L (Figure 59). At low fluoride initial concentrations, a very similar adsorption behavior of both adsorbents is observed. However, a completely different picture is clearly appreciated at high fluoride concentrations (higher than 50 mg/L), where BC reaches a saturation point (at around 2.7 mg F^-/g) while the removal capacity of nHAST keeps increasing, at least up to 200 mg/L with a defluoridation capacity close to 4 mg F^-/g, clearly surpassing the defluoridation ability of BC.

It is clearly observed from Figure 59 that the removal capacity of the nHAST keep on increasing, unlike the bone char which almost reaches its saturation point at about 50 mg/L fluoride initial concentration. This can be attributed to the utilization of less accessible sites because of increased diffusivity and activity of F^- ions upon the increased concentration, which in turn show the differences between the adsorbents surface, possibly indicate the homogeneity of sites on smooth surface that are uniformly accessible for the reaction in the case of BC, and the heterogeneity of sites that are unevenly distributed on rough surface for nHAST composite.

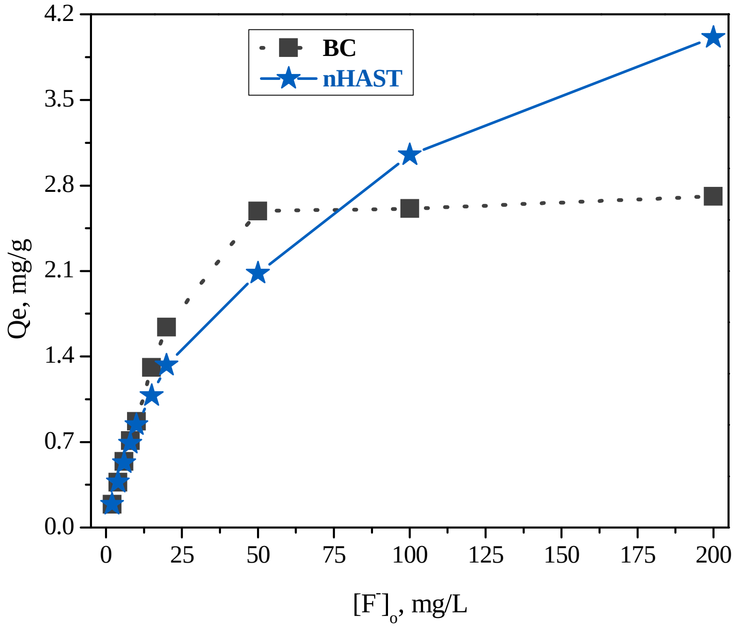

Figure 59: nHAST and BC fluoride adsorption isotherms performed at a dose of 10 g/L, with varying initial concentrations

Although there are different adsorption isotherm models, the two most frequently used models, Langmuir and Freundlich, have been applied as they give a good description of experimental behavior in a large range of operating conditions. Langmuir (Figure 60) and Freundlich (Figure 61) adsorption isotherm model parameters were analyzed using equations 10-13. The constants K_F and n of the Freundlich model are respectively obtained from the intercept and the slope of the linear plot of Freundlich model (eq. 14 as stated in sections 2.3). The model parameters, evaluated from the linear plots, are presented in Table 17.

Table 17: Langmuir and Freundlich isotherm model parameters describing the nHAST and BC fluoride adsorption

	Langmuir model			**Freundlich model**	
	nHAST	**BC**		**nHAST**	**BC**
Q_o, mg/g	4.02	2.74	K_F	0.621	0.686
b, L/mg	0.105	0.448	1/n	0.386	0.348
R^2	0.9657	0.9998	R^2	0.9975	0.9388
R_L	0.83	0.53			

The R_L values for the adsorption of fluoride onto nHAST and BC adsorbents, as calculated from the Langmuir model, are between 0 and 1, suggesting that the adsorption of fluoride under the experimental conditions is a favorable process (Table 17). According to the correlation coefficient, the adsorption of fluoride on the BC fits best with the Langmuir model (R^2 = 0.9998), which describes adsorption on a homogeneous surface (Figure 60). The adsorption capacity Q_o represents the maximum sorption capacity of the sorbent. The theoretical value of maximum capacity of BC (2.74 mg/g) is also in agreement with the experimental value of 2.72 mg/g (Figure 59), which confirms the appropriateness of this model to describe the adsorption process in BC. This value was within the range of the commercial bone chars that have fluoride adsorption capacities ranging from 1.0 to 3.0 mg/g in most cases, although a maximum capacity up to 7.32 mg/g has also been reported [113]. The experimental studies reported by C.K. Rojas-Mayorga et al. [113] and M. Gourouza et al. [114] also showed similar adsorption mechanisms (Langmuir model) for the adsorption of fluoride on other samples of BC.

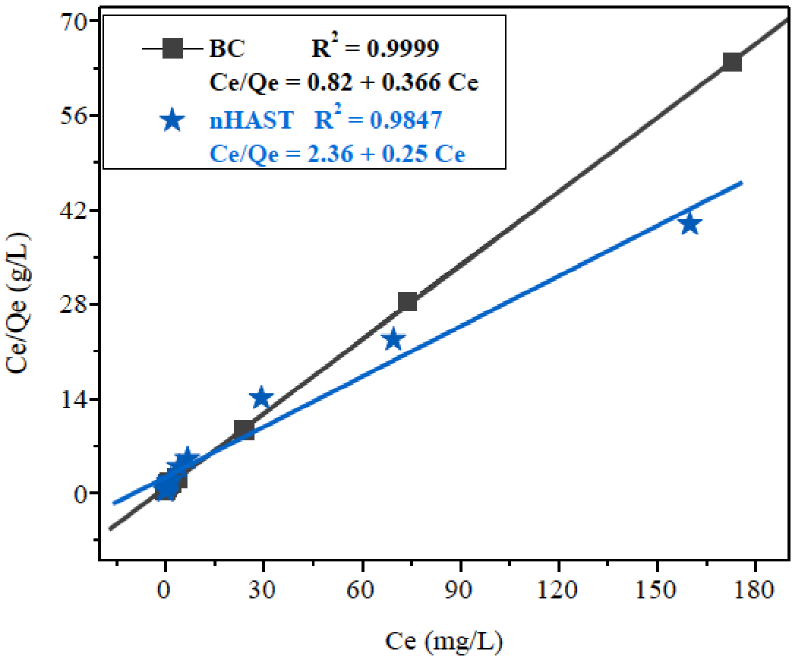

Figure 60: Linearized Langmuir adsorption isotherm for fluoride adsorption

Interestingly, the scenario is rather different in the case of the nHAST composite: Figure 60 clearly shows that in this case, fitting to the Langmuir model is rather poor and instead the Freundlich isotherm model (R^2 = 0.9975) fitted best the experimental data. This difference indicates a different adsorption mechanism between the two adsorbents, which occurs specially at high fluoride concentrations, as observed in Figure 58, being the adsorption mechanism heterogeneous in the case of the nHAST composite and homogeneous for BC. Adsorption of fluoride on HAp particles occurs by OH^-/F^- exchange at low fluoride concentrations [119], and such exchange is known to be dependent on the HAp particle size [118]. Such different heterogeneous adsorption mechanism of the HAp nanoparticles grown on the zeolite surface in nHAST could be related to the particular crystal morphology and size of HAp in this adsorbent, which enable a diffusion of fluoride to the inner part of the crystal at high fluoride concentrations. This fluoride adsorption is partially impeded by the diffusion required, and hence is slower, explaining the experimental observation of a heterogeneous adsorption upon increasing the fluoride concentration, and would be only available for our composite but not for BC. Mechanistic studies have also suggested that at high fluoride concentrations, the fluoride removal mechanism involves precipitation of fluorite by partial dissolution of HAp [119, 150]. Such fluorite precipitation could also provide an alternative explanation for the different adsorption mechanism of both adsorbents at high fluoride concentrations, which should be only possible for the nHAST composite, due to a larger dissolution of the nanosized HAp nanoparticles grown on the external surface of the zeolite.

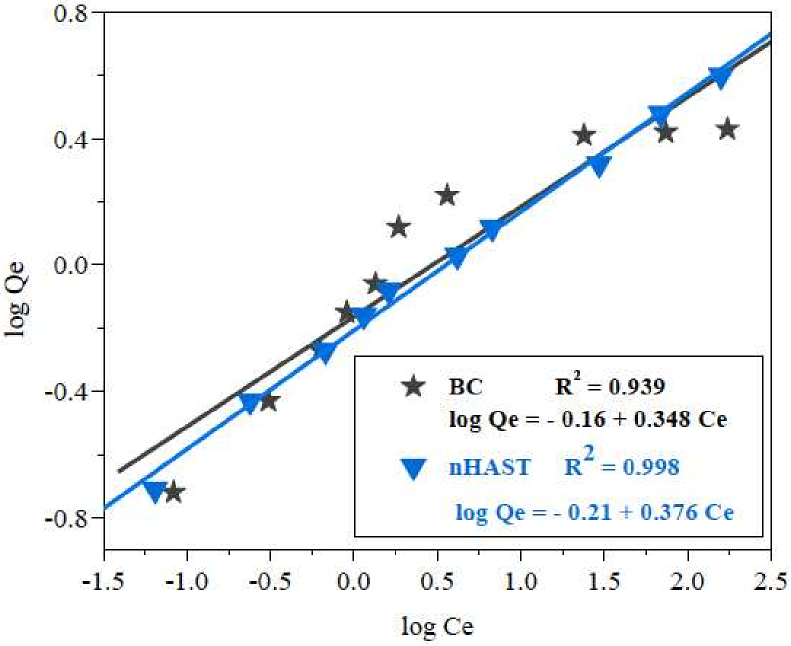

Figure 61: Linearized Freundlich adsorption isotherm for fluoride adsorption

The maximum adsorption capacity of the nHAST composite (around 4 mg/g, calculated from Figure 59) is higher than that of BC (2.74 mg F^-/g as calculated from the Langmuir model, Table 17, equivalent to the value obtained from Figure 59), which is used in this study as a reference material for natural hydroxyapatite, since it is currently the only applied defluoridation technology in several countries in the African Rift Valley. Different reports using HAp synthesized in different ways have shown typical HAp defluoridation capacities between 3 and 6 mg/g [38, 39, 120-122], which are smaller than our intrinsic HAp defluoridation capacity of 9.18 mg/g HAp observed at low fluoride initial concentrations. Our nHAST composite displays a very similar defluoridation behavior than BC and the fact that is supported on large zeolite crystals would also improve permeability issues.

4.9. Comparison of nHAST composite with synthetic HAp

Once more, our nHAST composite is compared with synthetic HAp, a newly arrived defluoridation adsorbent technology in Ethiopia by OSHO as a potential substitute for BC. To evaluate the HAp performance in fluoride removal, batch adsorption studies have been conducted under the same reaction conditions to that of nHAST and BC adsorbent materials already tested. Figure 62 demonstrates the defluoridation test results of HAp including nHAST composite and BC adsorbent materials.

As shown in Figure 62, the synthetic HAp performs very well, removes about 98 % fluoride from 5 mg/L initial fluoride concentrationat 10 g/L adorbent dose. This is slightly higher as compared to nHAST and BC adsorbents with 94.6 and 92.2 % fluoride removal efficiency, respectively at the same reaction conditions (10g/L adsorbent dose). The final residual fluoride concentrations of synthetic HAp, nHAST composite and BC adsorbents were found to be 0.10, 0.27, and 0.39 mg/L, respectively.

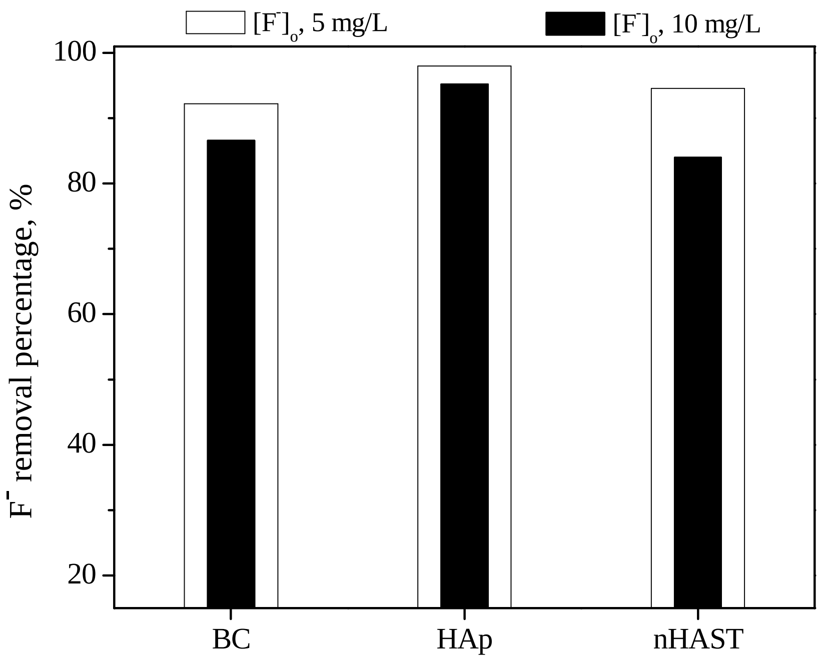

Figure 62: Fluoride removal efficiency (%) of BC, synthetic HAp, and nHAST composite samples at 10 g/Ldose

At the same adsorbent dose, if the initial fluoride concentration is higher, 10 mg/L, the HAp adsorbent shows more pronounced fluoride adsorption performance of around 95.2 %, whereas nHAST and BC perform a bit lower, about 84 and 86.6 % fluoride removal. In this case, the final residual fluoride concentrations were found to be 0.48 for HAp, 1.6 mg/L for nHAST and 1.34 mg/L for BC. However, in both cases the treated water meets the WHO standard for potable uses. Interestingly, the final water solution pH in the case of nHAST is found to be at about pH 7.5, more suitable than both BC of around pH 8 and synthetic HAp of around pH of 8.3. From the practical point of view, nHAST compensates the slightly less defluoridation performance by the use of locally available cheap natural raw materials as starting reagents and above all by its green synthesis procedure, in which no waste is generated even on a larger scale application.

Thus, we conclude again that nHAST composite is a suitable adsorbent, and has a high potential to be used as defluoridating agent in fluoride polluted drinking water.

Finally, similar works in the literature were surveyed in order to evaluate the adsorption capacity of nHAST (4.02 mg F^-/g) composite, as described in Table 18. M. Jiménez-Reyes et al. reported a higher adsorption capacity (4.7 mg F^-/g) of hydroxyapatite for fluoride ions in their study on sorption behavior of fluoride ions from aqueous solutions [39]. G.E.I. Poinern et al. also reported a maximum monolayer adsorption capacity of 5.50 mg/g for nanohydroxyapatite, synthesized through a combined ultrasonic and microwave method [148]. However, C.S. Sundaram et al. reported even a lower adsorption capacity than our nHAST composite in their study on fluoride sorption by nanohydroxyapatite/chitin composite, 2.84 mg F^-/g [38]. The reported defluoridation capacityof bare nHApis 1.296 mg F^-/g. L. Feng et al. in the study entitled “Heat regeneration of hydroxyapatite/attapulgite composite beads for defluoridation of drinking water” also reported the total adsorption capacity of 3.27 mg F^-/g for the composite beds, and 3.46 mg F^-/g for hydroxyapatite powder that used in the synthesis of the composite beds [121]. One latest study by K. Pandi et al. also recorded the defluoridation capacity of 3.72 mg F^-/g for alginate beads filled with nanohydroxyapatite [122], which is somehow comparable with nHAST composite.

In general, the nHAST composite possesses appreciable defluoridation capacity when compared with that of the reported adsorbents, which shows its high potential toward fluoride removal, even if the variations among the literature values possibly arising from the differences in the experimental conditions impose some difficulties in comparing.

Table 18: Maximum (monolayer) defluoridation capacities of some adsorbents reportedin literature

Adsorbent	**PZC**	**Q_e, mg/g**	**pH, initial**	**$[F]_o$, mg/L**	**Ref.**
nHAp	7.2	5.5	6	1-35	[151]
nHAp		4.57	5	3-5	[118]
nHAp		4.7	7		[39]
nHAp		3.1	3		[37]
nHAp	8.4	11.1	7	1-20	[152]
BC	7.0	5.44	7	1-20	[152]
nHAp		1.29	7	10	[38]
nHApCh	5.9	2.84	7	10	[38]
nHap/Alg		3.87			[122]
BC		5.44	7		[118]
Bone meal		4.99	5	3-5	[118]
nHAST	10	4.02	7.5	2-200	This work
BC		2.74	8	2-200	This work

Chapter Five

5. Conclusions

Natural stilbite zeolite from Ethiopia has a very low fluoride adsorption capacity. However, their unique chemical composition, specifically with respect to calcium content along with their inherent ion exchange properties, and excellent chemical and thermal stability as well as local availability make them very suitable for fluoride removal application after suitable chemical treatment processes. In this study, nanohydroxyapatite/stilbite (nHAST) composite was prepared from a locally available stilbite zeolite. The optimization of synthesis parameters allowed controlling the crystal growth of HAp on the surface of the natural zeolite stilbite. The process involves a cationic ion-exchange step and subsequent crystallization through regulation of the synthesis time, crystallization temperature, crystallization time, and crystallization pH.

This contribution reports the preparation of a nHAST composite under synthesis conditions of low crystallization temperature, at room temperature, autogenous crystallization pH value of 8, without ammonia solution, and crystallization time of 144 hours enable the crystallization of nano-sized hydroxyapatite crystals. The optimized nHAST composite is capable of working under very demanding conditions, in solutions with 5.0 and 10 mg/L of fluoride initial concentrations, at pH values similar to those of real waters, reducing to the WHO limit with a dose of 10 g/L. The defluoridation test has shown the high fluoride uptake capacity of nHAST for fluoride removal in the field as well. The low cost and easy accessibility of the materials employed for its preparation, as well as the simplicity of the synthesis procedure, make these materials suitable candidates for their use in fluoride removal from drinking water.

The relatively high PZC of nHAST composite (about 10.0) is indicating its suitability in fluoride adsorption through the electrostatic attraction between fluoride and the adsorbent below its PZC. Besides, its minimal effect in the presence of bicarbonate ion in the untreated water, up to 300 mg/L concentrations as well as the minimal pH dependence of the process shows further advantage of nHAST adsorbent for fluoride removal from groundwater.

Above all, the elimination of ammonia from the system, the most environmentally hostile among the reagent chemicals used in the synthesis of nHAST composite, is a considerable achievement of this work if looked from both scientific as well as commercialization point of view, because this is not only contributing to minimal production costs, but also with the use of inexpensive stilbite mineral, but it also makes the synthesis process “greener”. These results foresee a high potential of nHAST composite towards fluoride removal implementation.

List of Publications

1. L. Gómez-Hortigüela, A. B. Pinar, J. Pérez-Pariente, **T. Sani**, Y. Chebude, I. Díaz, Ion-exchange in natural zeolite stilbite and significance in defluoridation ability, **Microporous and Mesoporous Materials, 193 (2014) 93-102.**
2. M. Adem, **T. Sani**, Y.Chebude, G. Fetter, P. Bosch, I. Diaz, Comparison of the defluoridation capacity of zeolites from Ethiopia and Mexico, **Bulletin of the Chemical Society of Ethiopia, 29 (2015) 53-62.**
3. **T. Sani,** M. Adem, P. Bosch, I. Diaz, Defluoridation Performance Comparison of Nanohydrotalcite/Hydroxyapatite Composite with Calcined Hydrotalcite and Hydroxyapatite, **Water Air Soil Pollut, 90 (2016) 227-233.** This is a collabortive work (other than nanohydroxyapatite/silbite adsorbent) done with a Mexican Scientist Prof. P. Bosh, Universidad utónoma Nacional de Mexico, Mexico; the full paper work have been included in Apendix 2.
4. **T. Sani**, L. Gómez-Hortigüela, J. Pérez-Pariente, Y. Chebude, I. Díaz, Defluoridation performance of nano-hydroxyapatite/stilbite composite compared with bone char, **Separation and Purification Technology, 157 (2016) 42-48.**
5. **T. Sani**, L. Gómez-Hortigüela, J. Pérez-Pariente, A. Mayoral, Y. Chebude, I. Díaz, **Optimization of nHAST synthesis parameters, Manuscript in preparation.**

References

[1] S. Naseem, T. Rafique, E. Bashir, M. I. Bhanger, A. Laghari, T. H.Usmani, Lithological influences on occurrence of high-fluoride groundwater in Nagar Parkar area, Thar Desert, Pakistan, Chemosphere, 78 (2010) 1313-1321.

[2] Z. Mandinic, M. Curcic, B. Antonijevic, M. Carevic, J. Mandic, D. Djukic-Cosic, C.P. Lekic, Fluoride in drinking water and dental fluorosis, Scince Total Environment, 408 (2010) 3507-3512.

[3] V. Tomar, S. Prasad, D. Kumar, Adsorptive removal of fluoride from water samples using Zr–Mn composite material, Microchemical Journal, 111 (2013) 116-124.

[4] M. Arif, J. Hussain, I. Husain, S. Kumar, Fluoride toxicity and its distribution in groundwater of South East part of Nagaur District, Rajasthan, India, International Journal of Scientific Research in Agricultural Sciences, 6 (2014) 110-117.

[5] J. Murray, World Health Organization, Appropriate use of fluorides for human health, Geneva, Switzerland, (1986).

[6] J. Fawell, K. Bailey, J. Chilton, E. Dahi, L. Fewtrell, Y. Magara, Fluoride in drinking-water, World Health Organization, (2006) 1-144.

[7] S. M. Prabhu, S. Meenakshi, Synthesis of surface coated hydroxyapatite powders for fluoride removal from aqueous solution, Powder Technology, 268 (2014) 306-315.

[8] E.G. Paulson, Reducing fluoride in industrial wastewater, Journal of Chemical Engineering, 84 (1977) 89-94.

[9] SM. Hasany, M. Chaudhary, Sorption potential of Haro River quartz for the removal of antimony from acidic aqueous solution, Applied Radioactive Isotope, 47 (1996) 467-471.

[10] Z. Amor, S. Malki, M. Taky, B.Bariou, N. Mameri, A. Elmidaoui, Optimization of fluoride removal from brackish water by electrodialysis, Desalination, 120 (1998) 263-267.

[11] D. Cohen, H. Conrad, 65000 GPD fluoride removal membrane system in Lakeland California, USA, Desalination, 117 (1998) 19-35.

[12] W. Nigussie, F.Zewge, B.S. Chandravanshi, Removal of excess fluoride from water using waste residue from alum manufacturing process, Journal of Hazardous Materials, 147 (2007) 954-963.

[13] A. I. Alabdulaaly, A. I. Al-Zarah, M.A. Khan, Occurrence of fluoride in ground waters of Saudi Arabia, Applied Water Scince, 3 (2013) 589-595.

[14] A .Yehia, K. .Ezzat, Fluoride ion uptake by synthetic apatites, Adsorption Science and Technology, 27 (2009)337-347.

[15] V. Sunitha, B Muralidhara Reddy, M.R. Reddy, Assessment of groundwater quality with special reference to fluoride in South Eastern part of Anantapur District, Andhra Pradesh, Advances in Applied Science Research, 3 (2012) 1618-1623.

[16] L. Feenstra, L. Vasak, J. Griffioen, Fluoride in groundwater: Overview and evaluation of removal methods, International Groundwater Resources Assessment Centre, Netherlands,Report no.1 September (2007).

[17] R. Tekle-Haimanot, A. Fekadu, B. Bushera, Y. Mekonnen, Fluoride levels in water and endemic fluorosis in Ethiopian Rift Valley: 1st International Workshop on fluorosis prevention and defluoridation of water, Ngurdoto, Tanzania, International Society of Fluoride Research, Ngurdoto, Tanzania, October (1995) 18-22.

[18] T.Rango, J.Kravchenko, B.Atlaw, P. G.McCornick, M.Jeuland, B.Merola, A.Vengosh, Groundwater quality and its health impact: An assessment of dental fluorosis in rural inhabitants of the Main Ethiopian Rift, Environment International, 43 (2012) 37-47.

[19] W. Jianhua, L. Peiyue, Q. Hui, Study on the hydrogeochemistry and non-carcinogenic health risk induced by fluoride in Pengyang County, China, International journal of environmental sciences, 2 (2012) 1127-1134.

[20] NHMRC, Public statement, the efficiency and safety of fluoridation www.nhmrc.gov.au, available on December 2013 (2007).

[21] K. Sarala, P.R. Rao, Endemic fluorosis in the Village Ralla, Anantapuram in Andhra Pradesh an Epidemiological study, fluoride, 26 (1993) 177-180.

[22] S. Zerabruk, B.S. Chandravanshi, F. Zewge, Fluoride in black and green tea (Camellia Sinensis) infusions in Ethiopia: Measurement and safety evaluation, Bulletin of Chemical Society of Ethiopia, 24 (2010) 327-338.

[23] P. Renuka, K. Pushpanjali, Review on defluoridation techniques of Water, International Journal Of Engineering and Science, 2 (2013) 86-94.

[24] P. K. Pandey, M. Pandey, R. Sharma, Defluoridation of water by a Biomass: Tinospora cordifolia, Journal of Environmental Protection, 3 (2012) 610-616.

[25] H. Amini, G. A. Haghighat, M. Yunesian, R. Nabizadeh, A. H. Mahvi, M.H. Dehghani, Spatial and temporal variability of fluoride concentrations in groundwater resources of Larestan and Gerash regions in Iran from 2003 to 2010, Environmental Geochemistry and Health, (2015).

[26] L. Gómez-Hortigüela, J. Pérez-Pariente, R. García, Y. Chebude, I. Díaz, Natural zeolites from Ethiopia for elimination of fluoride from drinking water, Separation and Purification Technology, 120 (2013) 224-229.

[27] C.B. Dissanayake, The fluoride problem in the groundwater of Srilanka-environmental management and health, International Journal of Environmental Studies, 38 (1991) 137-155.

[28] P. Loganathan, S. Vigneswarana, J. Kandasamy, R. Naidu, Defluoridation of drinking water using adsorption processes, Journal of Hazardous Materials, 248- 249 (2013) 1- 19.

[29] M. Mahramanlioglu, I. Kizilcikli, I.O. Bicer, Adsorption of fluoride from aqueous solution by acid treated spent bleaching earth, Journal of Fluorine Chemistry, 115 (2002) 41-47.

[30] E. A. M. Vuhahula, J. R. P. Masalu, L. Mabelya, W.B. C.Wandwi, Dental fluorosis in Tanzania Great Rift Valley in relation to fluoride levels in water and in 'Magadi' (Trona), Desalination, 248 (2009) 610-615.

[31] H.Amini, S. M.Taghavi Shahri, M.Amini, M. M.Ramezani, Y.Mokhayeri, M.Yunesian, Drinking water fluoride and blood pressure, An environmental study, Biological trace element research, 144 (2011) 157-163.

[32] H.Chen, M.Yan, X.Yang, Z.Chen, G.Wang, D.Schmidt-Vogt, Y.Xu, J.Xu, Spatial distribution and temporal variation of high fluoride contents in groundwater and prevalence of fluorosis in humans in Yuanmou County, Southwest China, Journal of Hazardous Materials, 235-236 (2012) 201-209.

[33] L. Sun, Y. Gao, H. Liu, W. Zhang, Y. Ding, B.Li, An assessment of the relationship between excess fluoride intake from drinking water and essential hypertension in adults residing in fluoride endemic areas, Scince Total Environment, 443 (2013) 864-869.

[34] P.T.C. Harrison, Fluoride in water: a UK perspective, Journal of Fluorine Chemistry, 126 (2005) 1448-1456.

[35] G. Viswanathan, A. Jaswanth, S. Gopalakrishnan, S. Sivailango, Mapping of fluoride endemic areas and assessment of fluoride exposure, Scince Total Environment, 4 0 7 (2009) 1 5 7 9 - 1 5 8 7.

[36] T.A. Aoba, The effect of fluoride on apatite structure and growth, Critical Reviews in Oral Biology and Medicine, 8 (1997) 136-153.

[37] C. S. Sundaram, N. Viswanathan, S. Meenakshi, Defluoridation chemistry of synthetic hydroxyapatite at nano scale: Equilibrium and kinetic studies, Journal of Hazardous Materials, 155 (2008) 206-215.

[38] C. S. Sundaram, N. Viswanathan , S. Meenakshi, Fluoride sorption by nano-hydroxyapatite/chitin composite, Journal of Hazardous Materials, 172 (2009) 147-151.

[39] M. Jiménez-Reyes, M. Solache-Ríos, Sorption behavior of fluoride ions from aqueous solutions by hydroxyapatite, Journal of Hazardous Materials, 180 (2010) 297-302.

[40] W. Liang, L. Zhan, L. Piao, C.R. ssel, Fluoride removal performance of glass derived hydroxyapatite, Materials Research Bulletin, 46 (2011) 205-209.

[41] Y. Wang, N. Chen, W. Wei, J. Cui, Z. Wei, Enhanced adsorption of fluoride from aqueous solution onto nanosized hydroxyapatite by low-molecular-weight organic acids, Desalination, 276 (2011) 161-168.

[42] D. Zhang, H. Luo, L. Zheng, K. Wang, H. Li, Y. Wang, H. Feng, Utilization of waste phosphogypsum to prepare hydroxyapatite nanoparticles and its application towards removal of fluoride from aqueous solution hydroxyapatite by low-molecular-weight organic acids, Journal of Hazardous Materials, 241-242 (2012) 418-426.

[43] J. Lin, S. Raghvan, D.W. Fuerstenau, Adsorption of flouride ions by hydroxyapatite from aqueous solution, Colloids and Surfaces, 3 (1981) 357-370.

[44] L.E.L. Hammari, P. Barboux, K. Lahlil, A. Saoiabi, Retention of fluoride ions from aqueous solution using porous hydroxyapatite structure and conduction properties, Journal of Hazardous Materials B114 (2004) 41-44.

[45] F. Zewge, Solution to the fluoride problem in the rift valley region of Ethiopia. A Biannual News Letter of the Chemical Society of Ethiopia, 14 (2005) 15-22.

[46] S. Ayoob, A.K. Gupta, Fluoride in drinking waters: A review on the status and stress effects, Environtal Science and Technology, 36 (2006) 433-487.

[47] R. Tekle-Haimanot, Z. Melaku, H. Kloos, C. Reimann, W. Fantaye, L. Zerihun, K. Bjorvatn, The geographic distribution of fluoride in surface and groundwater in Ethiopia with an emphasis on the Rift Valley, Science Total Environment, 367 (2006) 182-190.

[48] S. Jagtap, L. M.K. Yenkie, Nitin, S. Rayalu, Fluoride in drinking water and defluoridation of water, Chemical Reviews, 112 (2012) 2454-2466.

[49] A.García-Pérez, M. E. Irigoyen-Camacho, A. Borges-Yáñez, Fluorosis and dental caries in Mexican Schoolchildren residing in areas with different water fluoride concentrations and receiving fluoridated salt, Caries Research, 47 (2013) 299-308.

[50] S. Alemu, E. Mulugetaa, F. Zewgea, B.S. Chandravanshi, Water defluoridation by aluminium oxide–manganese oxide composite material, Environmental Technology, 35 (2014) 1893-1903.

[51] F. Díaz-Barriga, A. Navarro-Quezada, MI. Grijalva, M. Grimaldo, JP. Loyola-Rodríguez, M. Deogracias Ortiz, Endemic fluorosis in México, Fluoride, 30 (1997) 233-239.

[52] L. Galicia-Chacón, N. Molina-Frechero, A. Oropeza-Oropeza, E. Gaona, L. Juárez-López, Análisis de la concentración de fluoruro en agua potable de la delegación Tláhuac, Ciudad de México, Revista Internacional de Contaminación Ambiental, 27 (2011) 283-289.

[53] X.Fan, D. J. Parker, M.D. Smith, Adsorption kinetics of fluoride on low cost materials, Water Research, 37 (2003) 4929 - 4937.

[54] J. Kravchenko , T. Rango, I. Akushevich, B. Atlawd, P. G. McCornick, R. B. Merola, C. Paul, E. Weinthal, C. Harrison, A. Vengosh, M.Jeuland, The effect of non-fluoride factors on risk of dental fluorosis: Evidence from rural populations of the Main Ethiopian Rift, Science Total Environment, 488–489 (2014) 595-606.

[55] UNICEF, UNICEF's position on water fluoridation, Availabilte at http://www.nofluoride.com/Unicef_fluor.cfm, (2014).

[56] R.T. H. Kloos, Distribution of fluoride and fluorosis in Ethiopia and prospects for control, Tropical Medicine and International Health, 4 (1999) 355-364.

[57] WHO, World Health Organization, Guidelines for drinking water quality, Health criteria and other information,2nd edition, Geneva, Switzerland, 2 (1996).

[58] UNESCO, Trace elements in groundwater and public health, Available at http://www.iah.org/briefings/Trace/trace.pdf., (2012).

[59] WHO, World Health Organization, Guidelines for drinking water quality, recommendations, Geneva, Switzerland, 1 (1984).

[60] M. Agarwal, K. Rai, R. Shrivastav, S. Dass, Defluoridation of water using amended clay, Journal of Cleaner Production, 11 (2003) 439-444.

[61] M. Amini, K.Mueller, K. C.Abbaspour, T.Rosenberg, M.Afyuni, K. N.Moller, M.Sarr, C. A.Johnson, Statistical modeling of global geogenic fluoride contamination in groundwaters, Environmental Science and Technology, 42 (2008) 3662-3668.

[62] RiPPLE, Fluoride mapping poster: Fluoride problems in Ethiopian drinking water. Research Inspired Policy and Practice Learning in Ethiopia and the Nile Region (RiPPLE), Addis Ababa,

Ethiopia, Available at http://r4d.dfid.gov.uk/PDF/Outputs/RiPPLE/fluoride-mapping-poster.pdf,(2015).

[63] E. Mulugeta, F. Zewge, C A. Johnson, B.S. Chandravanshi, Aluminium hydro(oxide)–based (AO) adsorbent for defluoridation of drinking water: Optimisation, performance comparison, and field testing, Water SA, 41 (2015) 121-128.

[64] T. Rango, A. Vengosh, M. Jeuland, R. Tekle-Haimanot, E. Weinthal, J. Kravchenko, C. Paul, P. McCornick, Fluoride exposure from groundwater as reflected by urinary fluoride and children's dental fluorosis in the Main Ethiopian Rift Valley, Science Total Environment, 496 (2014) 188-197.

[65] F.Adeno, E.Mulugeta, F.Zewge, Y.Chebude, Adsorptive removal of fluoride from water using nanoscale aluminium oxide hydroxide (AlOOH), Bulletin of the Chemical Society of Ethiopia, 28 (2014) 215-227.

[66] C. Reimann, K. Bjorvatn, B. Frengstad, Z. Melaku, R. Tekle-Haimanot, U. Siewers, Drinking water quality in the Ethiopian section of the East African Rift Valley I-data and health aspects, Science Total Environment, 311 (2003) 65-80.

[67] F. Wondwossen, A. N. Astrom, K. Bjorvatn, A. Ba˚rdsen, The relationship between dental caries and dental fluorosis in areas with moderate- and high-fluoride drinking water in Ethiopia, Community Dentistry and Oral Epidemiology, 32 (2004) 337-344.

[68] WHO, World Health Organization, Guidelines for drinking water quality, 4th edition, Geneva, Switzerland, 4 (2011).

[69] S. Kumar, K. Gopal, A review on fluorosis and its preventive strategies, Indian, Journal of Environmental Protection, 20 (2000) 430-436.

[70] R. Tekle-Haimanot, Study of fluoride and fluorosis in Ethiopia with recommendations on appropriate defluoridation technologies, Consultancy report, UNICEF-Ethiopia, 136 (2005) 1-55.

[71] UNICEF/WHO, JMP Thematic report on drinkingwater, (2011).

[72] WHO, World Health Organization, Guidelines for drinkingwater quality, Geneva, Switzerland, (1993).

[73] J. Mullen, History of water defluoridation, British Dental Journal, 199 (2005) 1-4.

[74] E. Dahi, F. Mtalo, B. Njau, H. Bregnhoj, Defluoridation using the Nalgonda technique in Tanzania, paper presented at 22nd WEDC conference, New Delhi, India, (1996).

[75] R. L. Ramos, J. Ovalle-Turrubiartes, M.A. Sánchez-Castillo, Adsorption of fluoride from aqueous solution on aluminum-impregnated carbon, Carbon 37, (1999) 609-617.

[76] CRC, Cooperative Research Centre for water quality and treatment of Australia, Investigation of defluoridation options for rural and remote communities, Research report No 41, (2008).

[77] R. Bhaumik, N.K. Mondal, Optimizing adsorption of fluoride from water by modified banana peel dust using response surface modelling approach, Applied Water Science, (2014) 1-21.

[78] L. Osterwalder, CA. Johnson, H. Yang, R. Johnston, Multi-criteria assessment of community-based fluoride removal technologies for rural Ethiopia, Science Total Environment, 488 (2014) 532-538.

[79] N. Chen, Z. Zhang, C. Feng, M. Li , D. Zhu, R. Chen, N. Sugiura, An excellent fluoride sorption behavior of ceramic adsorbent, Journal Hazardous Materials, 183 (2010) 460-465.

[80] F. Ogata, H. Tominaga, H. Yabutani, N. Kawasaki, Removal of fluoride ions from water by adsorption onto carbonaceous materials produced from coffee grounds, Journal Oleo Science, 60 (2011) 619-625.

[81] S Chidambaram, AL Ramanathan, S. Vasudevan, Fluoride removal studies in water using natural materials, Water SA, 29 (2003) 339-344.

[82] L. Gómez-Hortigüela, A.B.Pinar, J. Pérez-Pariente, T. Sani, Y. Chebude, I. Díaz, Ion-exchange in natural zeolite stilbite and significance in defluoridation ability, Microporous and Mesoporous Materials, 193 (2014) 93-102.

[83] C. Díaz-Nava, M. T. Olguín, M. Solache-Ríos, Water defluoridation by Mexican heulandite-clinoptilolite, Separation Science Technology, 37 (2002) 3109-3128.

[84] G. Moges, F. Zewge, M. Socher, Preliminary investigations on the defluoridation of water using fired clay chips, *Journal of African Earth Sciences*, 21 (1996) 479–482.

[85] B. Shimelis, F. Zewge, BS. Chandravanshi,Removal of excess fluoride from water by aluminium hydroxide,*Bull. Chem. Soc. Ethiop*, 20 (2006), 17–34.

[86] K. Gomoro, F. Zewge, B. Hundhammer, N. Megersa,fluorideremovalbyadsorption on thermally treated lateritic soils, Bull. Chem. Soc. Ethiop. 2012, 26(3), 361-372.

[87] R. Szostak, Molecular sieves: Principles of synthesis and identification, Van Nostrand Reinhold, New York, 1 (1989).

[88] E.G. Derouane, Catalysts for fine chemical synthesis: Microporous and mesoporous solid catalysts, John Wiley and Sons, Chichester, (2006) 141-156.

[89] S.A. H. Beitollah, J. Sadr, Recent applications of zeolites, Natural nanostructure materials, Iran Journal of Catalsis, 4 (2009) 214-223.

[90] A. Corma, H. Garcia, A unified approach to zeolites as acid catalysts and as supermolecular hosts exemplified, Journal of the Chemical Society, Dalton Transactions, 2000 (2000) 1381-1394.

[91] S.S. Hassani, F. Salehirad, H.R. Aghabozorg, Z. Sobat., Synthesis and morphology of nanosized zeolite L, Crystal Research and Technology, 45 (2010) 183-187.

[92] E.M. Flanigen, Molecular sieve zeolite technology, the first twenty years, Pure and Applied Chemistry, 52 (1980) 2191-2211.

[93] B.B. D. Georgiev, K. Angelova, I. Markovska, Y. Hristov, Synthetic zeolites structure, clasification, current trends in zeolite synthesis, International Science conference, Stara Zagora, Bulgaria (2009) 1-5.

[94] A.Z. S. Li, Y. Su, H. Zhang, L. Chen, J. Yang, C. Ye, and F. Deng, Bronsted/Lewis acid synergy in dealuminated HY Zeolite: A combined solid-state NMR and theoretical calculation study, Journal of American Chemical Society, 129 (2007) 11161-11171.

[95] L.B. McCusker, C. Baerlocher, H. Van Bekkum, E.M. Flanigen, P.A. Jacobs, J.C. Jansen, Zeolite structures: Introduction to zeolite science and practice, Studies in Surface Science and Catalysis, 137 (2001) 37-67.

[96] S. Wang, Y. Peng, Natural zeolites as effective adsorbents in water and wastewater treatment, Chemical Engineering Journal, 156 (2010) 11-24.

[97] P. Misaelides, Application of natural zeolites in environmental remediation: A short review, ,Microporous and Mesoporous Materials, 144 (2011) 15-18.

[98] L.Gomez-Hortiguela, J.Perez-Pariente, Y. Chebude, I. Diaz, Controlled growth of hydroxyapatite on the surface of natural stilbite from Ethiopia: Application in mitigation of fluorosis, RSC Advances, 4 (2014) 7998-8003.

[99] Ch. Baerlocher, L. B. McCusker, D. H. Olson, Atlas of zeolite framework types, 6th edition, Elsevier, Amsterdam, (2007).

[100] V.A. Drebushhchak, S.N. Dementiev, Y.V. Seryotkin, Journal of Thermal Analysis and Calorimetry, 107 (2012) 1293-1299.

[101] W.J. Mortier, Thermal stability of the stilbite-type framework: Crystal structure of the dehydrated sodium/ammonium exchange form, American Mineralogist, 68 (1983) 414-419.

[102] M.S. Onyango, Y. Kojima, O. Aoyi, E.C. Bernardo, H. Matsuda, Adsorption equilibrium modeling and solution chemistry dependence of fluoride removal from water by trivalent-cation-exchanged zeolite F-9, Journal of Coloid and Interface Scince, 279 (2004) 341-350.

[103] S. Samatya, U. Yüksel, M. Yüksel, N. Kabay, Removal of fluoride from water by metal ions (Al^{3+}, La^{3+} and ZrO^{2+}) loaded natural zeolite, Separation Science Technology, 42 (2007) 2033–2047.

[104] S. Xingbin, X. Chengju, H. Zhaochao, The fluoride-adsorption capacity and influencing factors study of Zeolite: International conference on challenges in Environmental Science and Computer Engineering, (2010).

[105] Y. Sun, Q. Fang, J. Dong, X. Cheng, J. Xu, Removal of fluoride from drinking water by natural stilbite zeolite modified with Fe(III), Desalination, 277 (2011) 121-127.

[106] Z. Zhang, Y. Tan, M. Zhong, Defluorination of wastewater by calcium chloride modified natural zeolite, Desalination, (2011),doi:10.1016/j.desal.2011.03.057.

[107] M.S. Onyango, Y. Kojima, A. Kumar, D. Kuchar, M. Kubota, H. Matsuda, Uptake of fluoride by Al^{3+} pretreated low-silica synthetic zeolites: Adsorption equilibrium and rate studies, Separation Science Technology, 41 (2006) 683-704.

[108] W.S. Wise, Handbook of natural zeolites: Natural zeolites commission of the International Zeolite Association, (2013).

[109] H.G. McCann, Reactions of fluoride with hydroxyapatite, Journal of Biological Chemistry, 201 (1953) 247-259.

[110] S.A. Leach, Reactions of fluoride ion with powdered enamel and dentine, British Dental Journal, 106 (1959) 133-142.

[111] V.E. Badillo-Almaraz, J.A. Flores, H. Arriola, F.A. López, L. Ruiz-Ramírez, Elimination of fluoride ions in water for human consumption using hydroxyapatite as an adsorbent, Journal of Radioanalytical and Nuclear Chemistry, 271 (2007) 741-744.

[112] M.E. Kaseva, Optimization of regenerated bone char for fluoride removal in drinking water: A case study in Tanzania, Journal of Water and Health, 04 (2006) 139-147.

[113] C. K. Rojas-Mayorga, A. Bonilla-Petriciolet, I. A. Aguayo-Villarreal, V. Hernández-Montoya, M. R. Moreno-Virgen, R. Tovar-Gómez, M.A. Montes-Morán, Optimization of pyrolysis conditions and adsorption properties of bone char for fluoride removal from water, Journal of Analytical and Applied Pyrolysis, 104 (2013) 10-18.

[114] M. Gourouza, I. Natatou, A. Boos, Elimination of fluoride ions from an aqueous solution with charred beef shoulder blade bones, Journal of Materials and Environmental Science, 5 (2014) 416-425.

[115] N. R. Muladno, H.N. Salundik, Chicken bone charcoal for defluoridation of groundwater in Indonesia, International Journal of Poultry Science, 13 (2014) 591-596.

[116] M. Azami, S. Jalilifiroozinezhad, M. Mozafari , M. Rabiee, Synthesis and solubility of calcium fluoride/hydroxy fluorapatite nanocrystals for dental applications, Ceramics International, 37 (2011) 2007-2014.

[117] R.A. Ramli, R. Adnan, M. Abu Bakar, S.M. Masudi, Synthesis and characterisation of pure nanoporous hydroxyapatite, Journal of Physical Science, 22 (2011) 25-37.

[118] S. Gao, R. Sun, Z. Wei, H. Zhao, H. Li, F. Hu, Size-dependent defluoridation properties of synthetic hydroxyapatite, Journal of Fluorine Chemistry 130 (2009) 550-556.

[119] V. Sternitzke, R. Kaegi, J-N. Audinot, E. Lewin, J.G. Hering, C.A. Johnson, Uptake of fluoride from aqueous solution on nano-sized hydroxyapatite: Examination of a fluoridated surface layer, Environment Science Technology, 46 (2012) 802−809.

[120] G. E. J. Poinern, M. K. Ghosh, Ng. Yan-Jing, T. B. Issa, S. Anand, P. Singh, Defluoridation behavior of nanostructured hydroxyapatite synthesized through an ultrasonic and microwave combined technique, Journal of Hazardous Materials, 185 (2011) 29-37.

[121] L. Feng, W. Xu, T. Liu, J. Liu, Heat regeneration of hydroxyapatite/attapulgite composite beads for defluoridation of drinking water, Journal of Hazardous Materials, 221- 222 (2012) 228-235.

[122] K. Pandi, N. Viswanathan, Synthesis of alginate bioencapsulated nano-hydroxyapatite composite for selective fluoride sorption, Carbohydrate Polymers, 112 (2014) 662-667.

[123] A. Nayak, Hydroxyapatite synthesis methodologies: An overview, International Journal of Chemical Technology Research, 2 (2010) 903-907.

[124] A. Beganskienė, O. Dudko, R. Sirutkaitis, R. Giraitis, Water based sol-gel synthesis of hydroxyapatite, Materials Science, 9 (2003) 383-386.

[125] R.N. Panda, M.F. Hsieh, R.J. Chung, T.S. Chin, FTIR, XRD, SEM and solid state NMR investigations of carbonate-containing hydroxyapatite nano-particles synthesized by hydroxide-gel technique, Journal of Physics and Chemistry of Solids, 64 (2003) 193-199.

[126] A. A. Chaudhry, S. Haque, S. Kellici, P. Boldrin, I. Rehman, F. A. Khalid, J.A. Darr, Instant nano-hydroxyapatite: A continuous and rapid hydrothermal synthesis, Chemical Communication, (2006) 2286-2288.

[127] A. E. S. Márquez, D. A. Lerner, G. Fetter, P. Bosch, D.Tichitb, E. Palomaresd, Preparation of layered double hydroxide/chlorophyll a hybrid nano-antennae: A key step, Dalton Transactions, 43 (2014) 10521-10528.

[128] T. Sato, H. Fujita, T. Endo, M. Shimada, A. Tsunashima, Synthesisofhydrotalcite-like compounds and their physico-chemical properties, Reactivity Solids, 5 (1988) 287-219.

[129] L. Liang, H. Jing, W. Min, D.G. Evans, D. Xue, Factors influencing removal of fluoride from aqueous solution by calcined Mg-Al-CO_3 layered double hydroxide, Journal of Hazardous Materials, B133 (2006) 119-128.

[130] L. Liang, H. Jing, W. Min, D. Xue, Kinetic studies on fluoride removal by calcined layered double hydroxides, Journal of Industrial and Engineering Chemistry Research, 45 (2006) 8623-8628.

[131] E. P. Van Straaten, Rocks for Crops: Agromi-nerals of Sub-Saharan Africa, ICRAF, Nairobi, Kenya, (2002) 137-144.

[132] M.Tigistu, T. Negash, L. Kassa, Report on exploration and evaluation of zeolite at Hawassa area, SNNP Regional state, Addis Ababa, Ethiopia, (2011).

[133] A. Asrat, S. Tadesse, L. Gómez-Hortigüela, J. Pérez-Pariente, R. García, Y. Chebude, I. Diaz, Unpublished results.

[134] K. Bourikas, J. Vakros, Ch. Kordulis, A. Lycourghiotis, Potentiometric mass titrations: Experimental and theoretical establishment of a new technique for determining the point of zero charge (PZC) of metal (hydr)oxides, Journal of Physical Chemistry, 107 (2003) 9441-9451.

[135] A. Tamiru, Preliminary analysis of the availability of groundwater in Ethiopia, Ethiopian Journal of Science, 16 (1993) 43-59.

[135] M.M.J. Treacy, J.B.Higgins, Collection of simulated XRD power patterns for zeolites, Elsevier, (2001).

[137] R. A. Howie, W. A. Deer, W. S. Wise, J. Zussman, Rock forming minerals, Framework silicates: Silica Minerals, feldspathoids and the zeolites, Geological Society, London, 4B (2004), ISBN: 978-971-86239-86144-86234.

[138] M.Adem, T.Sani, Y.Chebude, G.Fetter, P.Bosch, I.Diaz, Comparison of the defluoridation capacity of zeolites from Ethiopia and Mexico, Bulletin of the Chemical Society of Ethiopia, 29 (2015) 53-62.

[139] F.A. Mumpton, Clinoptilolite redefined, Ameralogist Mineralogist, 45 (1960) 351-369.

[137] J.R. Boles, Composition, optical properties, cell dimensions, and thermal stability of some heulandites group zeolites, American Mineralogist 57 (1972) 1463-1493.

[141] W. H. Wang, K.L. Matthews, Simulating gaseous distribution in a silver zeolite cartridge using sodium iodide solution, Health Physics, 90 (2006) 573-579.

[142] S. L. Serna, Retención de gases en zeolitas, Doctorado en ciencia e ingeniería de materiales, Instituto de Investigaciones en Materiales, U.N.A.M., (29 de septiembre de 2010).

[143] Y. Watanabe, Y. Moriyoshi, Y. Suetsugu, T. Ikoma, T. Kasama, T. Hashimoto, H. Yamada, J. Tanaka, Hydrothermal formation of hydroxyapatite layers on the surface of type-A zeolite, Journal of the American Ceramic Society, 87 (2004) 1395-1397.

[144] J. Li, J. Qiu, Y. Sun, Y. Long, Studies on natural STI zeolite: Modification, structure, adsorption and catalysis, Microporous and Mesoporous Materials 37 (2000) 365-378.

[145] X. Cheng, Y. Zhong, J. Wang, J. Guo, Q. Huang, Y. Long, Studies on modification and structural ultra-stabilization of natural STI zeolite, Microporous Mesoporous Materials, 83 (2005) 233–243.

[146] T. Sani, L. Gómez-Hortigüela, J. Pérez-Pariente, Y. Chebude, I. Díaz, Defluoridation performance of nano-hydroxyapatite/stilbite composite compared with bone char, Separation and Purification Technology, 157 (2016) 42-48.

[147] E. Passaglia, The heat behaviour of cation exchanged zeolites with the stilbite framework, Tschermaks Mineralogische und Petrographische Mittilumgen, 27 (1980) 67-78.

[148] C. Drouet, Apatite formation: Why it may not work as planned, and how to conclusively identify apatite compounds, BioMed Research International, (2013), Article ID 490946.

[149] C. Jäger, T. Welzel, W. Meyer-Zaika, M. Epple, A solid-state NMR investigation of the structure of nanocrystalline hydroxyapatite, Magnetic Resonance in Chemistry, 44 (2006) 573-580.

[150] C.M. Kanno, R. L. Sanders, S. M. Flynn, G. Lessard, S. C. B. Myneni, Novel apatite-based sorbent for defluoridation: Synthesis and sorption characteristics of nano-micro-crystalline hydroxyapatite-coated-limestone, Environment Science Technology, 48 (2014) 5798-5807.

[151] G. E. J. Poinern, Y.J. Ng, T. B. Issa, S. Anand, P. Singh, Defluoridation behavior of nanostructured hydroxyapatite synthesized through an ultrasonic and microwave combined technique, Journal of Hazardous Materials, 185 (2011) 29-37.

[152] N.A. Medellin-Castillo, R. Leyva-Ramos, E. Padilla-Ortega, R.O. Perez, J.V. Flores-Cano, M.S. Berber-Mendoza, Adsorption capacity of bone char for removing fluoride from water solution, Role of hydroxyapatite content, adsorption mechanism and competing anions, Journal of Industrial and Engineering Chemistry, 20 (2014) 4014-4021.

Appendices

Appendix 1: Experimental curves corresponding to the potentiometric mass titrations technique for the determination of the PZC of a) nHAST-1, b) nHAST-2, c) nHAST-3.

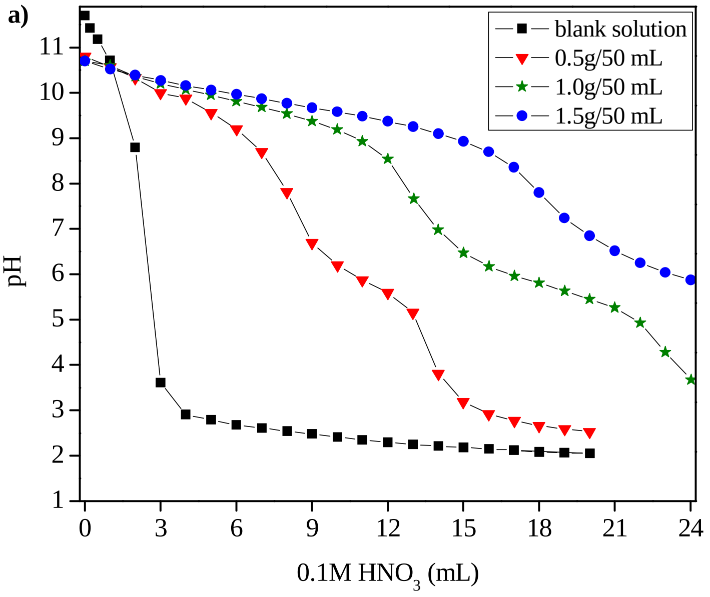

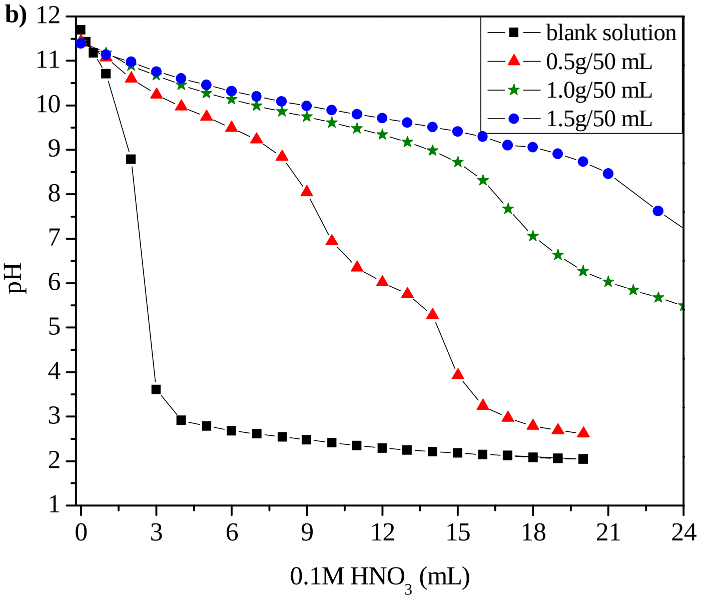

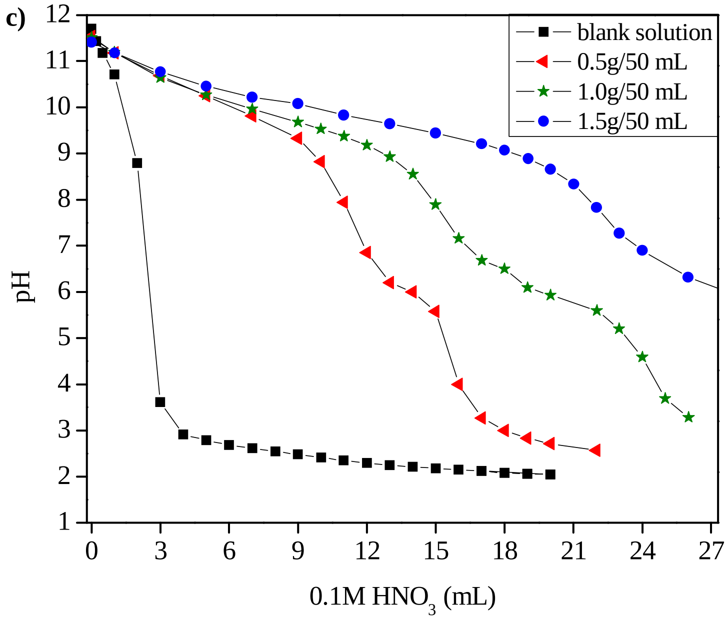

Appendix 2: T. Sani, M. Adem, P. Bosch, I. Diaz, Defluoridation Performance Comparison of Nanohydrotalcite/Hydroxyapatite Composite with Calcined Hydrotalcite and Hydroxyapatite, Water Air Soil Pollution, 90 (2016) 227-233, DOI 10.1007/s11270-016-2786-2.